COMPUTATIONAL MECHANISTIC STUDIES OF C-H AND C-X ACTIVATED ORGANOMETALLIC SPECIES WITH FIRST-ROW TRANSITION METALS

Steven Roldán Gómez

http://hdl.handle.net/10803/668858

DOCTORAL THESIS

Computational Mechanistic Studies of C-H and C-X Activated Organometallic Species with First-row Transition Metals.

Steven Roldán Gómez

2019

Doctoral Program in Chemistry

Supervised by: Dr. Xavi Ribas Salamaña and Dr. Josep Maria Luis Luis
Tutor: Dr. Xavi Ribas Salamaña

Presented in partial fulfillment of the requirements for a doctoral degree from the University of Girona

Universitat
de Girona

Dr. Xavi Ribas Salamaña and Dr. Josep Maria Luis Luis from the University of Girona,

DECLARE:

That the thesis entitled "Computational Mechanistic Studies of C-H and C-X Activated Organometallic Species with First-row Transition Metals", presented by Steven Roldán Gómez to obtain a doctoral degree, has been completed under our supervision and meets the requirements to opt for an International Doctorate.

For all intents and purposes, we hereby sign this document.

Dr. Xavi Ribas S.

Dr. Josep Maria Luis L.

Girona, ____________ de 2019

A aquellos que siguen estando presentes a pesar de la distancia.

Acknowledgements

This thesis was possible thanks to the financial support from the *Ministerio de Economía y Competitividad de España* (MINECO), with the FPI grant BES-2014-070441 and the project grant CTQ2013-43012-P.

In addition, I have to express my whole-hearted gratitude to my supervisors Xavi Ribas y Josep Maria Luis for all the shared knowledge, all the support and the patience during these four years. It has been a hugely enlightening experience and I feel very grateful for the opportunity they gave me and to have them both as my supervisors.

A big thank you to my experimental colleagues in the QBIS-CAT for all the great moments that we spent together learning, researching and having fun. Above all, to Anna Company, Miquel Costas, and Giorgo Olivo for inspiring me with their outstanding research spirit and passion for organometallic and inorganic chemistry (five years ago, I would have never imagined how fascinating these fields could be); to Lorena, Carla, Oriol, and Mireia, for all the hard work and the time that we spent doing research together.

I would like also to thank the “computational people” of the IQCC (Institut de Química Computacional i Catàlisi) that were kind enough to discuss research topics, or simply talk about “cool stuff” (I have learnt so much!). To those that I shared a lot of time with at “the office” like Dani Masó and Albert Artigas (during my days at the faculty) and also to all the people of CompBioLab (at the *parc cientific*), thank you all.

Moreover, I have to acknowledge all the people outside academia that have made these years, not only the four years of research, but a whole life-changing experience. Also, to those that were very close and had to suffer my “mood swings” due to the thesis, Ana Maestre (my “Spanish Mom”); Gaston, Saura, Filip (my flatmates); Joan and Corinna (my really good friends that always complained that I never had enough time for them); my “Erasmus friends”: Sara, Levina, Adam, Tim, Iskra; and of course, Lady Abby. Thanks to all of you, my mental health was not a mess during this hard process.

Finally, I would like to acknowledge my lifelong friends Felipe, Andrea and Cristiam. It is your inspiration and support that kept me going in the hardest moments of my academic and personal life, even with the distance I still feel your support, and for that you will have always my infinite gratitude.

List of Publications

Publications included in this thesis

Capdevila, L.; Meyer, T. H.; Roldán-Gómez, S.; Luis, J. M.; Ackermann, L.; Ribas, X. Chemo-Divergent Nickel(0)-Catalyzed Arene C–F Activation with Alkynes: Unprecedented C-F/C-H Double-Insertion. *ACS Catal.* **2019**, acscatal.9b03620.

Planas, O.; Roldán-Gómez, S.; Martin-Diaconescu, V.; Luis, J. M.; Company, A.; Ribas, X. Mechanistic Insights into the SN2-Type Reactivity of Aryl-Co(III) Masked-Carbenes for C-C Bond Forming Transformations. *Chem. Sci.* **2018**, *9* (26), 5736–5746.

Rovira, M.; Roldán-Gómez, S.; Martin-Diaconescu, V.; Whiteoak, C. J.; Company, A.; Luis, J. M.; Ribas, X. Trifluoromethylation of a Well-Defined Square-Planar Aryl-Ni II Complex Involving $Ni^{III}/CF_3\cdot$ and $Ni^{IV}-CF_3$ Intermediate Species. *Chem. - A Eur. J.* **2017**, *23* (48), 11662–11668.

Planas, O.; Roldán-Gómez, S.; Martin-Diaconescu, V.; Parella, T.; Luis, J. M.; Company, A.; Ribas, X. Carboxylate-Assisted Formation of Aryl-Co(III) Masked-Carbenes in Cobalt-Catalyzed C-H Functionalization with Diazo Esters. *J. Am. Chem. Soc.* **2017**, *139* (41), 14649–14655.

Other Publications:

Magallón, C.; Serrano-Plana, J.; Roldán-Gómez, S.; Ribas, X.; Costas, M.; Company, A. Preparation of a Coordinatively Saturated μ-H2:H2-Peroxodicopper(II) Compound. *Inorganica Chim. Acta* **2018**, *481*, 166–170.

Capdevila, L.; Andris, E.; Briš, A.; Tarrés, M.; Roldán-Gómez, S.; Roithová, J.; Ribas, X. Silver(I)-Catalyzed C-X, C-C, C-N, and C-O Cross-Couplings Using Aminoquinoline Directing Group via Elusive Aryl-Ag(III) Species. *ACS Catal.* **2018**, *8* (11), 10430–10436.

List of Abbreviations

Abbreviation	Description
DFT	Density Functional Theory
HAT	Hydrogen Atom Transfer
AFIR	Artificial Force Induced Method
SC-AFIR	Single component AFIR
DS-AFIR	Double Sphere AFIR
CPU	Central Processing Unit
HF	Hartree-Fock
LDA	Local Density Approximation
GGA	Generalized Gradient Approximation
KS-DFT	Kohn-Sham DFT
SIE	Self-Interaction Error
STO	Slater-Type Orbital
GTO	Gaussian-type Orbital
QM/MM	Quantum Mechanics/Molecular Mechanics
PCM	Polarizable Continium Model
SMD	Solvation Model based on Density
SPE	Single Point Energy
SET	Single Electron Transfer
PES	Potential Energy Surface
TFE	2,2,2-TriFluoroEthanol
EDA	Ethyl diazo acetate
RDS	Tate-Determining Step
HRMS	High Resolution Mass Spectroscopy
LA	Lewis Acid
TDTT	5-(trifluoromethyl)dibenzothiophenium triflate
TS	Transition State
IRC	Intrinsic Reaction Coordinate
***p*-DMA**	dimethylamine
LUMO	Lowes Unoccupied Molecular Orbital
8-AQ	8-aminoquinoline group
DPA	Diphenylacetylene
NMR	Nuclear Magnetic Resonance
GRRM	Global Reaction Route Mapping

List of Figures

List of Tables

Table of Contents

Summary

During the last decades computational chemistry has become a resourceful tool in the quest to understand and predict the mechanism and the reactivity of chemical systems. This is especially true in the area of organometallic catalysis, where the computational models used nowadays show better accuracy/computational-cost ratio compared to the ones of a few decades ago. In addition, it has become common practice to rationalize the mechanistic proposals for a specific reaction based on combined computational and experimental evidence. The role of computational chemistry is particularly relevant when there is not enough experimental evidence due to the elusive nature of the intermediate and reactive species or when we want to gain insight into the reaction regarding properties that are not measurable by experimental means.

This thesis addresses the calculations performed to determine the mechanism of four different organometallic reactions catalyzed by first-row transition metals that were developed in tight synergic collaboration with the experimental researchers of our group.

In the first project (chapter 4), we predicted the unexpected formation of a C-metalated aryl-Co(III) enolate, which we interpreted as a masked carbene (due to its reduced reactivity compared to standard unstable M=carbenes) and we studied its reactivity. Here, our computations suggested an unprecedented Co(III)-mediated intramolecular S_N2-like C-C bond formation mechanism and also they indicated this step as the rate-determining step of the reaction. We also unraveled, computationally, how the presence of Lewis acid additives (like Li^+), the use of electron-poor diazoacetates, and the strength of the nucleophile, affected the kinetics of the reaction.

In the second study (chapter 5), we discerned between the one-electron or two-electron mechanistic character for the trifluoromethylation of a well-defined aryl-Ni(II) complex. Our calculations pointed to a mixture between one-electron and two-electron mechanisms. First, the aryl-Ni(III)/$\cdot CF_3$ (trifluoromethyl radical and the aryl-nickel(III) complex adduct) is formed, with the subsequent rapid formation of an aryl-Ni(IV)-CF_3 intermediate, which undergoes reductive elimination to afford the trifluoromethylated product.

In the next study (chapter 6), the reactivity of a C-F activated Nickelocycle with alkynes, we used theoretical calculations to analyze the experimentally observed chemoselectivity in the formation of the aromatic-homologation or the mono-alkene annulation product. In addition, we also analyzed the preference for the C-F activation over the C-H activation for this specific organometallic Ni-catalysis. Our calculations unraveled the crucial role of the Li^+ in assisting the removal of the fluoride anion.

Finally, in the last project (chapter 7), we explored the reactivity of a well-defined macrocyclic aryl-Fe(II) complex and the unexpected CO insertion on the ligand scaffold, transforming an amine moiety to an amide, with systematic reaction-path-exploratory tools, as well as with the standard DFT calculations. We have computed several possible mechanisms for this reaction, but a plausible mechanism of this unique reaction remains unknown.

Resumen

Durante las últimas décadas, la química computacional se ha convertido en una herramienta muy útil para indagar y comprender los mecanismos que rigen los sistemas químicos. Especialmente en el área de la catálisis organometálica, donde los modelos computacionales pueden tener una buena relación entre precisión y coste computacional. Además, hoy en día es una práctica habitual racionalizar propuestas mecanísticas para una reacción específica basándose en evidencias tanto computacionales como experimentales. El papel de la química computacional es particularmente relevante en los casos en que no hay suficiente evidencia experimental, debido a la naturaleza evasiva de las especies intermedias.

Esta tesis aborda los cálculos realizados en la determinación del mecanismo de cuatro reacciones organometálicas diferentes, catalizadas por metales de la primera serie de transición, que se desarrollaron en estrecha colaboración con los investigadores experimentales de nuestro grupo.

En el primer proyecto (capítulo 4), se encontró la formación inesperada de un enolato de aril-Co(III) metalado en C, que interpretamos como un *carbeno enmascarado* debido a su reactividad reducida en comparación con los carbenos metalados (M=carbenos), habitualmente inestables, y estudiamos su reactividad. Nuestros cálculos sugieren que el mecanismo de formación de enlace C-C mediado por el complejo de Co(III) es similar al de una S_N2 intramolecular. Dichos cálculos indicaron que este paso mecanístico era la etapa determinante de la reacción. En estos estudios, también desvelamos computacionalmente cómo la cinética de la reacción se ve afectada por la presencia de aditivos tipo ácido de Lewis (como Li^+), el uso de diazoacetatos electrón-deficientes, y la fuerza del nucleófilo de la reacción.

En el segundo estudio (capítulo 5), discernimos entre el carácter mecanístico tipo transferencia de un solo electrón o de dos electrones, para el caso de la trifluorometilación de un complejo de aril-Ni(II) bien definido. Nuestros cálculos apuntaron a un mecanismo que se puede entender como una combinación entre ambas propuestas. Primero, se forma un aril-Ni(III)/$\cdot CF_3$, el cual decae rápidamente en aril-Ni(IV)-CF_3, que, consecuentemente, genera el producto de trifluorometilación a través de una eliminación reductiva.

El siguiente estudio (capítulo 6), trata la reactividad de un complejo C-F activado de Nickel cíclico con alquinos, en el cual utilizamos cálculos teóricos para analizar la quimio selectividad observada experimentalmente en la formación del producto de homologación aromática o el producto de anulación de mono-alqueno. También analizamos la preferencia en esta reacción por activar el enlace C-F en vez del C-H por parte del complejo de níquel. Además, nuestros cálculos revelaron el papel crucial del Li^+ en la eliminación del anión fluoruro (F^-) sobrante después de la activación del C-F.

Finalmente, en el último proyecto (capítulo 7), exploramos la reactividad de un complejo macrocíclico aril-Fe(II) bien definido, en el cual se da la inesperada inserción del CO en la cadena orgánica del ligando, transformado un grupo amina en amida, con programas de exploración sistemáticas de rutas de reacción, así como con los habituales cálculos DFT. A pesar de que calculamos diversos posibles mecanismos de reacción, el mecanismo que explica el comportamiento de ésta sigue sin resolverse.

Resum

Durant les últimes dècades, la química computacional s'ha convertit en una eina molt útil per indagar i comprendre els mecanismes que regeixen els sistemes químics. Especialment en l'àrea de la catàlisi organometàl·lica, on els models computacionals poden tenir una bona relació entre precisió / cost computacional. A més, avui en dia es una pràctica habitual racionalitzar propostes mecanístiques, per a una reacció específica, basats en evidències tant computacionals com experimentals. El paper de la química computacional és particularment rellevant en els casos en què no hi ha prou evidència experimental, a causa de la naturalesa evasiva de les espècies intermèdies.

Aquesta tesi aborda els càlculs realitzats en la determinació del mecanisme de quatre reaccions organometálicas diferents, catalitzades per metalls de transició de la primera sèrie, que es van desenvolupar en estreta col·laboració amb els investigadors experimentals del nostre grup.

En el primer projecte (capítol 4), es va trobar la formació inesperada d'un enolat de aril-Co(III) metal·lat en C, que interpretem com un carbè emmascarat a causa de la seva reactivitat reduïda en comparació amb els usualment inestables carbens metal·lats (M=carbens), i vam estudiar la reactivitat d'aquests. Els nostres càlculs suggereixen que el mecanisme de formació d'enllaç C-C catalitzat pel complex de Co(III) és similar al d'una S_N2 intramolecular. Aquests càlculs van indicar que aquest pas mecanístic era l'etapa determinant de la reacció. En aquests estudis, també desvetllem computacionalment com la cinètica de la reacció es veu afectada per la presència d'additius tipus àcid de Lewis (com Li^+), l'ús de diazoacetats electró-deficients, i la força del nucleòfil de la reacció.

En el segon estudi (capítol 5), discernim entre el caràcter mecanístic tipus transferència d'un sol electró o de dos electrons, per al cas de la trifluorometilació d'un complex d'aril-Ni(II) ben definit. Els nostres càlculs van apuntar a un mecanisme tipus que es pot entendre com una combinació entre ambdues propostes. Primer, es forma un aril-Ni(III)/ $\cdot CF_3$, el qual decau ràpidament en aril-Ni(IV)-CF_3, que, conseqüentment, genera el producte de trifluorometilacin a través d'una eliminació reductiva.

El següent estudi (capítol 6), tracta la reactivitat d'un complex C-F activat de Nickel cíclic amb alquins, en el qual utilitzem càlculs teòrics per analitzar la quimio selectivitat observada experimentalment en la formació del producte d'homologació aromàtica o el producte de formació de un anell de mono-alquè. També analitzem la preferència en aquesta reacció per activar l'enllaç C-F en comptes de el C-H per part del complex de níquel. A més, els nostres càlculs van revelar el paper crucial del Li^+ en l'eliminació de l'anió fluorur (F^-) sobrant després de l'activació del C-F.

Finalment, en l'últim projecte (capítol 7), vam explorar la reactivitat d'un complex macrocíclic aril-Fe(II) ben definit, en el qual es dóna la inesperada inserció del CO en la part orgànica del lligant, utilitzant programes d'exploració sistemàtiques de rutes de reacció, així com amb el habituals càlculs DFT. Tot i que vam calcular diversos possibles mecanismes de reacció, el mecanisme que explica el comportament d'aquesta encara segueix sent un misteri.

Chapter 1

Introduction

*Image taken from ©istock

Summary

In this Chapter, we will introduce briefly the topic of computational chemistry and its relevance to develop and to understand the reactivity of transition metals, in particular, the first row transition metals.

1.1 Modern chemistry and catalysis.

One of the main challenges that science has faced since the last century, especially Chemistry, is the fact that most sources of valuable materials to maintain the wellbeing of modern society (oil, precious metals, helium etc.) are finite.[1,2] Therefore, those resources will be depleted in a not-so-far future. To overcome this, several worldwide strategies are continuously developed in different fields with the intention to find new and more abundant sources, or to create new alternatives, or even more, to efficiently harness the already scarce ones (including their renewal).[3–5]

As part of those strategies to "*improve the world*", catalysis shows up as a plausible environmentally friendly and resource-efficient approach when applied to industry, and actually is one of the 12 principles of Green Chemistry.[6] Catalysis is defined as all those processes where an agent, the catalyst (which in many cases can be recovered), increases the rate of a chemical reaction without altering the overall standard Gibbs energy of the reaction. In other words, it modifies the kinetics of the reaction without changing its overall thermochemistry. In addition, the fact that it can be recovered grants that the same catalyst can react again and again with other "batches" of starting materials.[1]

These characteristics of the catalytic processes makes it very appealing to the endeavor of creating a better, greener and resource-efficient future. The catalyst allows the exploitation of raw materials without producing excessive amounts of waste and without being consumed by the reaction.

In principle, catalysts have been present around us since long ago. Indeed, one of the efficient ways of nature's molecular machinery to work is by catalysis. All living creatures depend on the catalytic properties of the proteins inside of each cell to perform their job and sustain life.[7] What makes the difference during this era is that humankind is learning how to manipulate and how to apply some of those catalytic agents in the development of better and cleaner chemistry.

Catalytic processes are involved in almost every compound around us, from decomposition of matter itself to the most advanced industrial processes implemented nowadays. In general, there is a wide variety in types of catalysis but to simplify their study, they are separated into three main frames of study: homogeneous catalysis, heterogeneous catalysis, and biocatalysis. Although some of the concepts and theory are the same for the three types of catalysis, this thesis is focused on transition metal catalyzed homogeneous catalysis.

1.2 Homogeneous catalysis and transition metals.

According to its definition, homogeneous catalysis are those catalytic processes where the catalyst is in the same physical phase as reactants and products[8]. The most common situation is to have all the species in solution (liquid phase), and that is the case throughout this thesis. Within the vast number of examples of homogeneous catalysis processes, the one involving an organometallic species as catalyst has experienced a remarkable development during the last decades.[9]

Indeed, the development of homogeneous catalysis with organometallic compounds has been a trending topic inside the chemistry community. Certainly, some of the Nobel Chemistry Prizes of the last two decades have been attributed to homogeneous catalyzed processes with organometallic molecules as the catalyst (**2001**, William S. Knowles and Ryoji Noyori *"for their work on chirally catalysed hydrogenation reactions*" and K. Barry Sharpless "*for his work on chirally catalysed oxidation reactions*"; **2005**, Yves Chauvin, Robert H. Grubbs and Richard R. Schrock "*for the development of the metathesis method in organic synthesis*"; **2010**, Richard F. Heck, Ei-ichi Negishi and Akira Suzuki "*for palladium-catalyzed cross couplings in organic synthesis*").[10–12]

Some of the reasons why transition-metal complexes gained interest in the field of catalysis are their versatility and the facility to change or tune their properties just by changing or modifying the ligands of the metal. Most of the industry and research have found a "gold mine" of new and very efficient catalysts when exploring a wide variety of ligand coordinated to the so-called precious (noble) metals (like Palladium, Rhodium, Platinum, etc.).[13–16] Such precious metal catalysts opened a whole new catalogue of reactions to produce bulk material and fine chemicals which the comfort of our modern life relies on, with cross-coupling, polymerization and C-H activation catalysis being some of the most highlighted processes.[17] The ability of these noble metals to yield selectively desired products, their stability to standard condition, and their preference for conventional two-electron oxidation-state changes, are essential to their high activity, durability and balance to maintain efficient catalytic cycles, thus making them a cornerstone of modern catalytic chemistry.

However, in terms of sustainability, one of the disadvantages of these catalysts is that they are based on precious transition metals, which implies that they are expensive and very scarce compared to other metals. Such drawbacks led to an exploration of organometallic complexes with the rest of the more available (and hopefully cheaper) first-row transition metals during the past decades, which yielded a considerable amount of papers related to homogeneous catalysis with abundant transition metals published every year.[18]

By default, the more abundant transition metals (also known as 3d transition metals or first-row transition metals) are more reactive than their late-transition counterparts. 3d transition metals can easily perform single-electron redox processes and ligand redistribution and exchange, which adds complexity to their reactivity, resulting in additional reaction pathways, diminishing in selectivity, and limiting the catalytic lifecycles. Indeed, finding the suitable conditions and the adequate ligands that yield a similar (or better) specific catalytic activity than their noble metal analogues can be challenging. It is this challenge that persuaded the chemistry community to pursue this goal, expanding new and old frontiers to understand the molecular details under the catalytic behavior and consolidate the foundations for the next generation of earth-abundant metal catalysis. Such a challenge cannot be faced by synthetic means alone; it requires the consolidation of synthetic strategies, spectroscopic studies, kinetic studies, and theoretical and computational efforts.[19,20]

It is in this line that in the last two decades computational chemistry has become a key factor in the development and understanding of catalytic processes, to the point that it is routinely used, like any other laboratory technique (NMR, X-ray diffraction, etc.) to characterize some properties of the system.

1.3 Computational Chemistry in Homogeneous Catalysis.

First-principle-based computational methods to determine the molecular electronic structure have progressed enormously during the last decades due to faster computers (better technologies), more efficient algorithms, and more accurate methods. Therefore, it has become common practice that mechanistic studies rely much more on calculation. Computational chemistry is especially useful in providing insight regarding the nature of intermediates and transition states that are suggested by spectroscopic studies, kinetic studies or simply chemical intuition. Computational modeling and molecular simulations have contributed enormously to the progress in the fundamental understanding of catalytic phenomena.[19–25] They have become a fundamental part of catalytic studies, giving an atomic framework in the elucidation of catalytic mechanism and interpretation of spectroscopic data.

Advanced methodologies in quantum chemistry are quite reliable to support analysis of chemical reactivity, complex reaction paths, kinetic models, and catalytic cycles. DFT (Differential Functional Theory) methods are especially well suited for this kind of task, since they are usually able to reach the chemical accuracy at very low computational cost. Therefore, DFT is the most common choice to provide feedback and guidelines for the development of new and improved catalytic systems.

It must be said that the widespread application of computational chemistry has been facilitated by the simplification and availability of quantum chemistry and molecular modeling software. Computational chemistry, nowadays, is employed by a wide range of experimental research groups (not only by theoretical chemists) to support their mechanistic proposals, comparing their (usually) DFT mechanistic models with their experimental results to obtain correlations that confirm their hypothesis with chemical accuracy.

Conventionally, computational (chemistry) accuracy is related to the good performance of a specific methodology to compute specific fundamental chemical properties with respect to experimental or highly accurate (high level) theoretical results. In the case of calculations on catalytic systems, the overall accuracy also strongly depends on the quality of the model that we use to represent the system, *i.e.*, how well it accounts for the most relevant chemical details with respect to the reaction in question.[26] In general, there is a trade-off between the level of theoretical approximation and the level of chemical details in the model.

Despite the fact that computational chemistry has acquired a fundamental role in catalysis, it must be recognized that mere calculations alone are not (always) able to provide a correct picture of a mechanism most of the time. Even some researchers argue that they should not be relied upon.[27–31] And, in part, it is true because the main tangible reference is the solid experimental evidence when it comes to describe a catalytic mechanism. However, it is becoming more frequent to use computational chemistry to correct wrong results based on misinterpreted experimental data.[32] Therefore, the best option for a complete study of a reaction is to perform a combined and synergic experimental and computational work to provide better insight into the behavior and mechanism of catalytic systems.

In this thesis, we show four specific examples in which computations are combined with experimental evidence collected in our research group to gain insight into the respective mechanism of each reaction in combination.

1.4 Cross-coupling Catalysis.

As a general description, cross-coupling reactions involve the formation of a new bond between two fragments or molecules aided by a transition metal catalyst. In the most common cases, one of the fragments is an aryl, vinyl, alkyl halide or pseudohalide (trifluoromethylsulfonates, isocyanide …) acting as the electrophile, which couples with the corresponding C-based or heteroatom-based nucleophile thanks to the catalyst interplay. Even though this is not a new type of reaction, since it has existed for several decades, it has been the recent advances that have broadened its scope and applicability.[33,34] Currently, it is one of the most relevant chemical processes in several academic fields and industrial sectors.[35] Part of the popularity of the cross-coupling reaction emerged from the diversity of reagents used for the reaction and the wide variety of functional groups incorporated in the reagents. Among all possible transition metal for cross-coupling, palladium-catalyzed cross-coupling stands out as a powerful tool to form C-C and C-Heteroatom bonds.[36,37]

The first reports on palladium-catalyzed cross-coupling showed up in the seventies.[38] At the beginning, a wide range of cross-coupling reactions were developed for C-C bond formation based on C acting as nucleophiles, such as aryl, vinyl, alkyl derivatives of magnesium (Kumada-Corriu),[39] boron (Suzuki -Miyaura),[40] tin (Stille-Migita),[41] zinc (Negishi),[42] or silicon (Hiyama),[43] or reactions with terminal alkynes acting as nucleophiles in the presence (Sonogashira)[44] or absence (Heck alkynylation)[45] of a copper co-catalyst. In general, the proposed mechanism starts with the oxidative addition of the organo halide to the catalyst. Then, the second partner undergoes a transmetallation, which places both coupling partners on the same metal center while eliminating the functional groups. As a final step a reductive elimination of the two coupling fragments occurs, which regenerates the catalyst and yields the organic product (**Figure 1.1**).

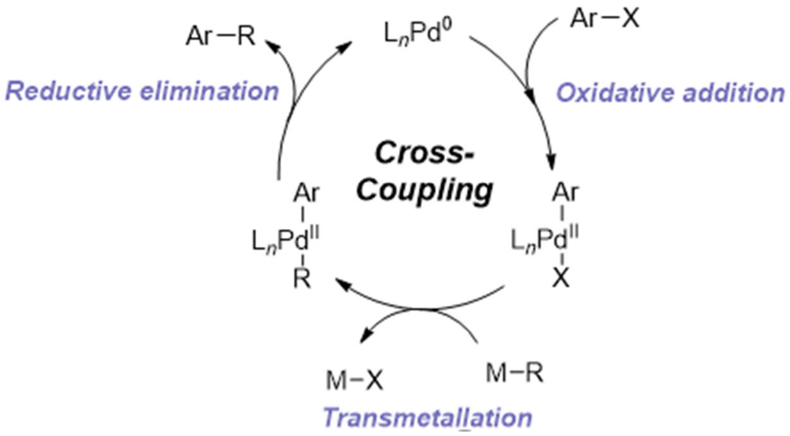

Figure 1.1 General mechanism for Pd-catalyzed cross-coupling reactions, which is initiated by oxidative addition of an organic halide at Pd(0), continues through transmetallation and finishes by reductive elimination.

During the nineties, Hartwig and Buchwald developed methodologies for a palladium catalyzed C-N cross-coupling methodology that greatly expanded the perspective of the field.[46,47] In a similar way, during the remaining years all kinds of cross-coupling have been developed that have improved the applicability of the reaction. Although all these palladium-based methodologies were powerful and chemically efficient, they presented some drawbacks, like the cost and scarcity of Palladium, and the expense of catalyst removal from the final product, among others.[48–50] Therefore, strategies looking for greener, better and cheaper alternatives have gained attention during the last two decades, which has yielded manifold and interesting alternatives with abundant transition metals like Nickel.

1.4.1 Nickel in cross-coupling catalysis.

The use of Nickel as a replacement of Palladium, in principle, is chemically reasonable, because both belong to the same group in the periodic table and share some common properties. The idea of using Nickel in cross-coupling reaction is not new. Already in the seventies, it was used in reactions of alkenes and alkynes, such as nucleophilic allylation, oligomerization, cycloisomerization and reductive couplings. However, the outstanding result with Palladium cast a shadow on Nickel for a few decades until the need for a greener and cheaper solution presented itself, resurrecting the interest for cross-coupling Nickel catalysis. Furthermore, Nickel is quite versatile, showing excellent performance in a wide range of cross-coupling reactions,[51] including C-C bond-forming reactions as Negishi, Suzuki-Miyaura, Stille, Kumada, and Hiyama couplings. Throughout the years, the development of new Ni-catalysts, ligands, and substrates have greatly improved the scope of these transformations. Despite the tremendous advances in C-C bond formation, some C-heteroatom couplings remain a challenge.

Nickel exhibits unique properties compared to Palladium. One of them is accessibility to all the oxidation states ranging from Ni(0) to Ni(IV),[35,52] while Pd usually adopts Pd(0) and Pd(II) states, and more rarely Pd(IV) (**Figure 1.2 A**). The open-shell electronic-configuration states of Nickel are more stable, therefore, electrophilic activation by Nickel can imply a classic two-electron oxidative addition or single electron processes to afford radicals and Ni(III) or Ni(I) species.[53] In addition, Nickel possesses a lower electronegativity and reduction potential than Palladium, which contribute to a slower β-H elimination (side reaction) in alkyl-Nickel compounds in comparison to Palladium ones.[54–56]

Regarding Ni cross-coupling mechanisms, two-electron mechanism via Ni(0)/Ni(II) intermediates is expected when C_{sp2} electrophiles are used.[57] Concerted oxidative addition of Ni(0) to aryl halides is followed by transmetallation with a nucleophile and a subsequent reductive elimination (**Figure 1.2 (B)(i)**). The low reduction potentials and electronegativity of Ni usually suggest that Ni(0) is highly reducing and can facilitate oxidative addition. This effect can be enhanced by strong s-donor ligands. Nevertheless, it is not easy to predict the mechanism of the nickel-catalyzed cross-coupling reactions. They are very dependent on the type and the character of ligand (it can change from one-electron to two-electron mechanism).

We can also have, in the case of two-electron pathways, that the reaction proceeds via Ni(I)/Ni(III) intermediates in which, usually, the transmetallation occurs before the oxidative addition (**Figure 1.2** (**B)(ii)**).

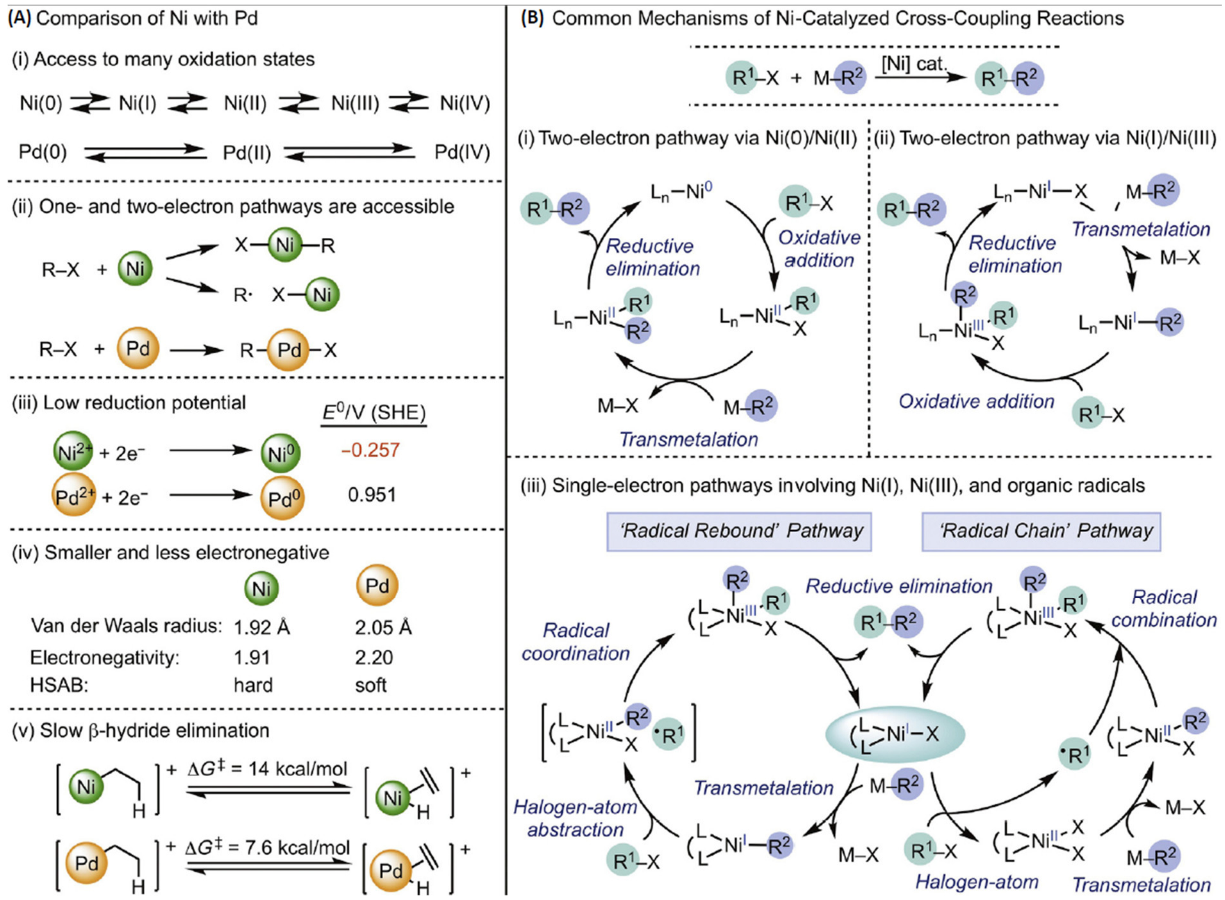

Figure 1.2 Fundamental properties of Nickel catalysts and consequences in catalysis.[58] **(A)** Comparison of the properties of Ni and Pd. **(B)** Common mechanisms of Ni-catalyzed cross-coupling reactions. **(i)** Two-electron redox pathway mediated by Ni(0) and Ni(II) intermediates. **(ii)** Two-electron redox pathway mediated by Ni(I) and Ni(III) intermediates. **(iii)** One-electron redox pathways.

The vast majority of Ni-catalyzed cross-coupling reactions with C_{sp3} electrophiles involves single-electron transfer pathways and organic radical intermediates (**Figure 1.2 (B)(iii)**). The sequence of electrophile and nucleophile activation may be system dependent, leading to two possible pathways, usually involving a Ni(I)–halide intermediate (highlighted in the center of (**Figure 1.2** (**B)(iii)**). In the 'radical rebound cycle', the Ni(I)–halide first undergoes transmetallation with the nucleophile to form a Ni(I)–carbyl intermediate that interacts with the alkyl electrophile to generate a Ni(II) complex and an alkyl radical. A combination of the radical with Ni(II) forms a Ni(III) intermediate that undergoes subsequent reductive elimination to yield the product. In the case of the 'radical chain pathway', the Ni(I)–halide intermediate initiates the formation of a radical from the alkyl electrophile prior to transmetallation with the nucleophile. Then, a Ni(III) intermediate is formed after a radical combination with Ni(II)-R^2 , which finally suffers a reductive elimination to yield products and the initial Ni(I)complex.

Due to the versatility of Nickel and the fact that Nickel cross-coupling catalysis is still a young field, with a lot of potential for innovation, several less common cross-coupling mechanisms have been found recently. Nevertheless, they are specific to each catalytic system and their conditions.[58]

1.5 C-H activation.

Most fuels, chemicals and materials are derived from petroleum feedstock, which is a mix of saturated and unsaturated hydrocarbons. These hydrocarbons are characterized by a lack of reactivity, which is caused by the strength of their C-C and C-H bonds. Therefore, the chemical community is highly motivated by the search of synthetic strategies to transform such raw materials into more valuable products in a simple manner.

Although C-H bonds are quite unreactive, they are not completely inert. In fact, there are certain industrial (chemical) processes that are used to functionalize hydrocarbons, which in general involve free radicals, carbocations, organometallic reagent, or super acids electrophiles,[59] along with extreme conditions like high temperatures. These extreme conditions increase the cost of the process, cause emissions which generate adverse environmental effects, and reduce the selectivity of the reaction. Here is where the introduction of the transition metals to the organic toolbox of reagent enters the field to solve some of the previous problems and to generate new strategies.[60]

The term *C-H activation* is used to describe the C-H cleavage processes. In organometallics, the term "C-H activation" refers to species or moieties wherein the C-H bond interacts directly with the metal reagent or catalyst to (usually) later yield a carbon-metal intermediate in the absence of free radicals or ionic intermediates. Moreover, it is used to distinguish metal mediated C-H cleavage from hydrogen atom transfer (HAT), traditional radical, and ionic substitutions.

C-H bond activation can be distinguished or separated into two types: inner-sphere and outer-sphere C-H functionalization (**Figure 1.3**). The former involves an initial cleavage of the Carbon-Hydrogen bond to afford an alkyl/aryl-metal intermediate species, which after reacting with either an external reagent or with another ligand at the metal center yields a particular product. The outer-sphere (coordination chemistry approach) mimics biological catalyzed oxidation reactions containing an activated ligand X (X=oxo, carbene, imino, etc) that can react with the C-H bond in two ways, either by direct insertion; or H-atom abstraction followed by radical rebound.

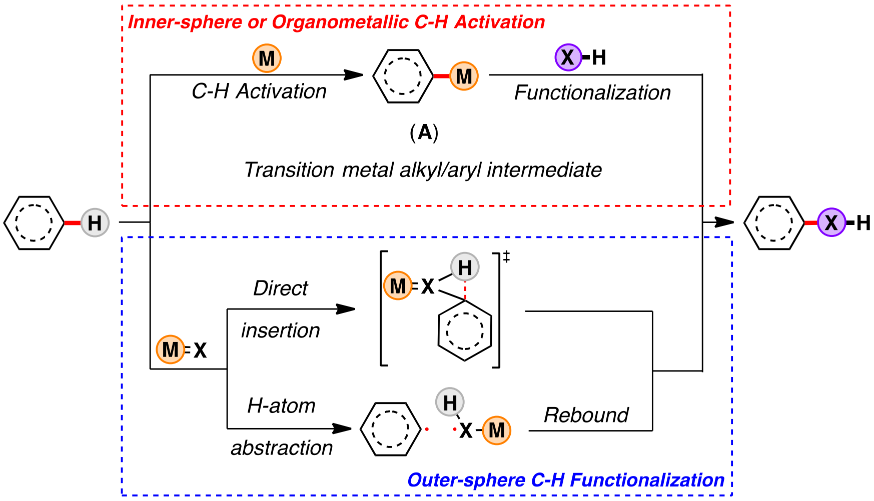

Figure 1.3 Inner-sphere (top) and Outer-sphere (bottom) C-H functionalization.

1.5.1 Cobalt in C-H activation.[61]

The use of 3d metals for C-H activation has always been promoted by the need for a better cost-effective catalysis for a myriad of transformations. Cobalt, as one of the earth abundant transition metals which is environmentally friendly, carries great potential for several applications in homogeneous catalysis.[62]

The use of Cobalt in metal-mediated C-H activation is not surprising if we consider the widely developed field of rhodium-catalyzed C-H activation[63,64] and the fact that the reduced electronegativity of Cobalt, compared to Rhodium, augments the nucleophilicity in the organometallic cobalt-complexes. Since its discovery, low-valent catalyzed processes have been the usual procedure when it comes to cobalt catalysis. However, new methodologies with high-valent cobalt catalysis have gain popularity during the last years (**Figure 1.4**) and it has emerged as a powerful tool in organic synthesis (since it shows similar or even better reactivity to high-valent rhodium catalysis). Nowadays, the field of cobalt- catalyzed C-H functionalization is divided in two categories based on the oxidation state of the metal: i) the low-valent approach, where the active catalyst corresponds to Co(0) or Co(I) species;[65] and ii) the high-valent approach, where the active catalysts typically contain a Co(III) center. The chapter of this thesis that corresponds to cobalt catalysis (chapter 4), deals with a specific case of high-valent cobalt catalysis.

In each chapter of this thesis we will briefly introduce the chemical "state of the art" of each specific catalytic system. In this way, the goal of the research and our contribution to the field will be in context. Since this thesis is using computational chemistry to study the reactivity, it is necessary to explain some of the general concepts of computational and quantum chemistry, which will be introduced in the next chapter.

C-H activation.

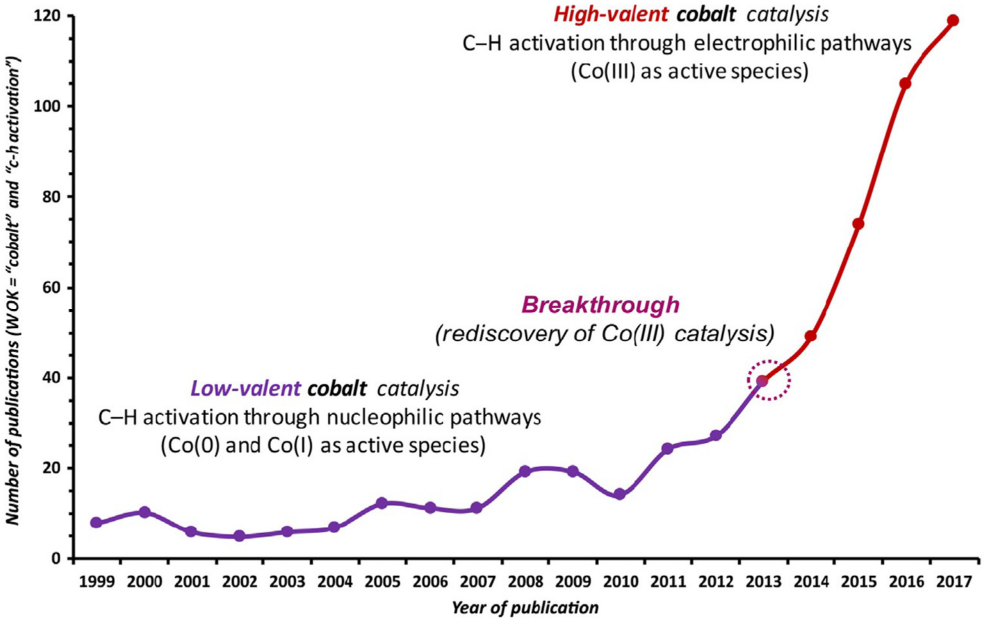

Figure 1.4 Publications of cobalt-catalyzed C–H activation per year. Number of publications obtained from WoK (search criteria used: cobalt AND C–H activation).[61]

Chapter 2

Methodology

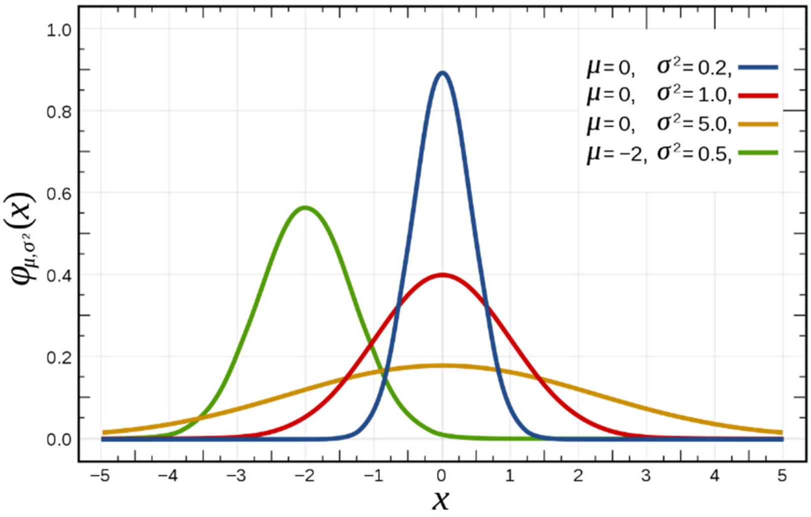

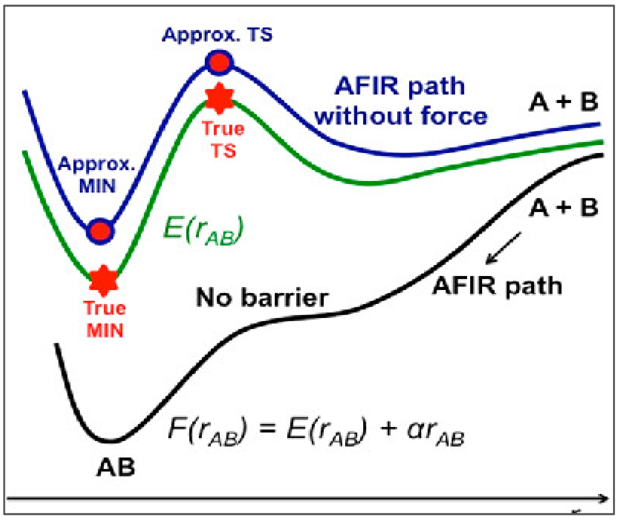

Summary

In this chapter, we briefly introduce some of the concepts from quantum chemistry and physical-chemistry related to the methods used in this thesis. Initially, we talk about Density Function Theory (DFT) and its implications. Then we explain some key points that should be taken into account when performing computational chemistry studies. Next, we briefly introduce Marcus theory to approximately calculate the energy barriers related to an electron transfer process. Finally, we will explain the Artificial Force Induced Reaction Method (AFIR), specifically the SC-AFIR and the DS-AFIR approaches.

2.1 Density Functional Theory.

In computational chemistry, quantum mechanical models based on wavefunctions are considered extremely accurate to describe (or predict) the properties of a system; however, their characteristic high demand of computational time or CPU resources makes them difficult to implement in more than small and simple systems. On the contrary, molecular mechanical models, which are based on classical mechanics, tend to be much less accurate (and limited) to describe the properties of a system. Nevertheless, they are so little demanding of time and CPU resources that they are commonly used to yield rough descriptions of the properties of a system. Besides these two kinds of molecular modeling, there is a third common option, DFT (Density Functional Theory), which is considered to have the best compromise between accuracy and CPU cost.[66,67] In this thesis, we performed all the calculation with DFT modeling.

Density functional theory is a modeling approach based on using electron density functions of the system to describe their properties. DFT is based on the Hohenberg-Kohn theorems[67] that state the following: 1) the electronic energy and any other property of the ground state can be calculated as a functional of the exact electron density of the system; 2) the exact electron density of the system is the one that minimizes the electronic energy of the ground state, following the variational principle (equation 2.1).

$$E[\rho]\geq E[\rho_{\mathrm{exact}}]=E_{\mathrm{min}} \tag{2.1}$$

A functional is any mathematical expression that is applied to obtain a number from a function. In the case of DFT, the functionals are applied to the electron density. Since the electron density function ($\rho(r)$) only depends on three spatial coordinates of the system (x, y, and z), the DFT approach is able to reduce the computational cost of quantum many-electron calculations with respect to wavefunction-based methods. On the contrary, Hartree-Fock (HF) and post-HF methods depend on 3N variables (4N when taking the spin into account), where N is the number of electrons. The final step in the development of DFT is to find a functional that connects the electron density of the system with its energy. However, such a paramount task can be very difficult to complete, and therefore is currently not fully solved.

Based on the classical quantum approach, we can divide the total energy functional into three terms: kinetic energy $T[\rho]$, attraction between the nuclei and electrons $E_{ne}[\rho]$, and electron-electron interaction $E_{ee}[\rho]$ (for a given geometry of the molecule, the nuclear-nuclear repulsion is assumed constant due to the Born-Oppenheimer approximation). Furthermore, we can divide the $E_{ee}[\rho]$ term into Coulomb ($J[\rho]$) and exchange ($K[\rho]$) parts, implicitly including the correlation energy to all the terms (eq. 2.2).[67]

$$E[\rho] = T[\rho] + E_{en}[\rho] + J[\rho] + K[\rho] \tag{2.2}$$

Based on this, several early attempts of constructing orbital-free functionals (depending only on the electron density) have been performed. Such types of constructions, if they work, could bring the whole potential of DFT depending on a few variables of the chemical system which number is independent of system size. However, these methods show low accuracy, especially for the T and K functionals. Therefore, such methods are not popular and are far from becoming a method of general use.[68,69]

In 1965, DFT methods came into general use with the publication of a practical method to calculate ρ and E[ρ] by Khon and Sham.[70] They introduced orbitals in DFT, defining a kinetic functional under the molecular-orbital approximation. Since the exact density is not known, the approximate density is written in terms of a set of auxiliary one-electron functions, the KS orbitals:

$$\rho = \sum_{i=1}^{N} |\phi_i(r)|^2 \tag{2.3}$$

Kohn and Sham considered a fictitious reference system of non-interacting electrons with the same electron density as the real system, moving through a local effective external potential, called the Kohn-Sham potential (V_{eff}(r)). The Kohn-Sham (KS) model is closely related to the HF method in the sense that HF uses an independent-electron wavefunction (Slater-determinant), whose electrons interact through the HF potential. Therefore, the energy functional can be described as:

$$E[\rho] = \frac{\hbar}{2m_e}\sum_{i=1}^{N}\int \phi^*(r)\nabla^2\phi(r)dr - \sum_{i=1}^{N}\int \frac{Z_i e^2}{4\pi\varepsilon_0|R_1 - r|}\rho(r)dr + \frac{1}{2}\int\int \frac{\rho(r)\rho(r')e^2}{4\pi\varepsilon_0|r - r'|}dr\, dr' + E_{XC}[\rho] \tag{2.4}$$

Here the kinetic electronic energy of non-interacting electrons can be calculated by an equivalent expression to the one used in HF theory, corresponding to the first term in equation 2.4. Other components that also have equivalent expressions in HF theory are the second term corresponding to the classical electron-nucleus attraction, E_{ne}[ρ], and the third term which is the classical Coulomb repulsion between charges, J[ρ]. Finally, the last term is the exchange-correlation term that corresponds to the difference between the exact kinetic energy of the real system and the kinetic energy of non-interacting electrons and all non-classical interactions between electrons, E_{xc}[ρ]. Nevertheless, the latter term is the only unknown energetic term in the KS formalism of DFT. This last term is the core of the DFT framework. Unfortunately, it is not easy to find accurate expressions that describe the exchange-correlation term. Assuming that the exact E_{xc}[ρ] functional would exist, DFT-KS would be able to provide the exact total energy of the system with similar computational cost that one would require to determine the uncorrelated HF energy.

From the large number of DFT functionals that we can find, it is the nature of the approximation for the exchange-correlation functional $E_{xc}[\rho]$ that makes each one of them unique. The simplest approximation for the DFT exchange-correlation energy is the so-called Local Density Approximation (LDA), which approximates the exchange-correlation energy density at a given position as a function of the electron density at that same local position. The next level of sophistication is the generalized gradient approximation (GGA), in which the energy functional also depends on the gradient of the density at that given position. A level above is the meta-GGA, in which the energy functional also depends on the local kinetic energy density calculated using Kohn-Sham orbitals or on the Laplacian of the electron density (*i.e.* second derivative). Higher-order approximations such as hybrid functionals, or fully non-local functionals, can improve the accuracy, but they create nonlocality dependence for the density and also higher computational cost.[71] It is worth mentioning that in hybrid DFT methods, the exchange-correlation includes a fraction of the HF exchange, while in fully non-local functional (or double hybrids functionals), the energy density approximation also depends on unoccupied orbitals.

DFT Modeling is just an approximation and therefore it contains error by default. There are three of them that are quite clear. The first one is the Self-Interaction Error (SIE), which is generated because in KS-DFT, as the energy is a functional of the one-electron density, there is no way to precisely distinguish between the correct two-body Coulomb interactions from fictitious one-electron self-interactions. The SIE is due to the fact that the $E_{xc}[\rho]$ is an approximation.[66,72]

A second error in DFT is caused by the inherent description of the wavefunction as a single determinant, which leads to a near-degeneracy energy (non-dynamical or static correlation) error. One of the first ways to tackle this issue is the use of spin-unrestricted description, where α-spin electron density occupies a different region of space than β-spin electron density. Generally, DFT studies of first-raw transition metals complexes use an unrestricted description. Since the self-interaction error tends to decrease barriers while the lack of non-dynamic correlation increases them, there is a substantial cancellation effect between these two errors of DFT. For that reason, trying to remove just one of the error sources when both are present could lead to larger errors.[73]

The third error in some functionals arises from the lack of a description of the long-range dispersion interactions (Van der Waals). These long-range interactions can be viewed as instantaneous electron correlations when “charge fluctuations” on one region of the system induce dipole moments on the other fragment. In a more precise picture, electromagnetic zero-point energy fluctuations in the vacuum lead to “virtual” excitations to allowed atomic or molecular electronic states. The corresponding (pseudo)densities interact electrostatically (with exchange-type modifications at smaller distances) and these interactions are not represented by conventional (hybrid) DFT functionals that only consider electron exchange but do not employ virtual orbitals.[74] Since the dispersion correction is an add-on term, this does not alter the wavefunction or molecular properties for a specific given geometry. Nevertheless, geometry optimization with dispersion correction will lead to different geometry because the energetic dispersion correction contributes to the forces acting on the atoms.

In this thesis we used the Grimme dispersion correction,[75] when necessary. The dispersion correction used is described in the specific methodology subsection of each chapter (4-7). In the same way, we can find the specific DFT functional that we use for each project in the same section. In general, we used the GGA functional BP86[76,77], the hybrid functional B3LYP[78–81] and the highly parametrized (based on meta-GGA) M06-L[82] functional.

2.2 The role of the Basis.

Before explaining its relevant role in DFT, it is necessary to describe the definition of a basis set: a basis set is a set of basis functions used to describe the shape of the orbitals in terms of atomic orbital contributions and linear combinations of such functions with angular functions are used to describe molecular orbitals. Usually a basis function can be one of two types: Slater Type Orbitals (STO) or Gaussian Type Orbitals (GTO),

$$\chi_{\zeta,n,l,m}(\mathrm{r},\theta,\varphi) = \mathrm{N}\mathrm{Y}_{l,m}(\theta,\varphi)r^{n-1}e^{-\zeta r} \qquad \textit{Slater type Orbitals} \qquad (2.5)$$

$$\begin{aligned} \chi_{\zeta,n,l,m}(\mathrm{r},\theta,\varphi) &= \mathrm{N}\mathrm{Y}_{l,m}(,\theta,\varphi)r^{2n-2-l}e^{-\zeta r^2} \\ \chi_{\zeta,l_x,l_y,l_z}(\mathrm{x},y,z) &= \mathrm{N}x^{l_x}y^{l_y}z^{l_z}e^{-\zeta r^2} \end{aligned} \qquad \textit{Gaussian Type Orbitals} \qquad (2.6)$$

where N is a normalization constant and $Y_{l,m}$ are spherical harmonic functions. In the case of Cartesian GTO, the sum of l_x, l_y, and l_z, determines the type of orbital (s=0, p=1, etc). STO can better represent the orbitals near the nucleus than GTO and their functional decay away from the nucleus is also better described. Nevertheless, the integrals of a GTO function are much more facile to compute than the ones in a STO. This fact led to the construction of linear combinations of GTO with a similar behavior to STO, overcoming the disadvantages of a single GTO, and still being computationally affordable (in comparison to STOs). For example, the linear combination of three GTOs can model a STO (**Figure 2.2**). This makes the linear combination of GTOs the preferred method to construct a basis set to this day.

For a basis set the more basis functions it has, the better it describes the "real" molecular orbitals (in principle, an infinite number of basis functions would be a complete basis set, CBS). At the same time, the more functions it has, the higher the computational cost (the amount of processors and time that it requires to perform the calculation). Therefore, when we select a basis set, there must be a compromise between its accuracy and its computational cost: with enough basis functions for a flexible basis set and not so many basis functions to be computationally available.

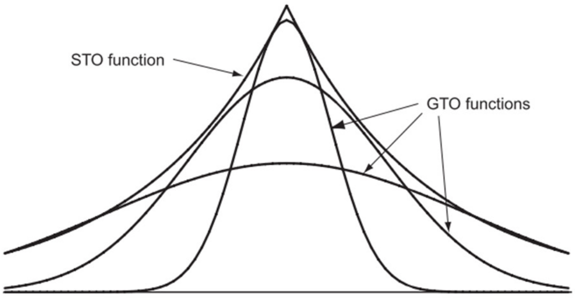

Figure 2.1 Approximating a Slater-type orbital with 3 Gaussian-type orbitals. Most of the STO is covered by the three GTO functions.[83]

Several basis sets tend to separate inner core orbitals from valence shell orbitals to describe them differently. Usually more functions are used to describe the valence shell orbitals (because they are the ones that contribute the most to their reactivity and their properties). The amount of functions that are used to represent the valence orbitals are denoted by the *degree of split valence basis*; this means, how many basis sets we have to describe each valence orbital compared to the minimum basis set. Therefore, in the case that we have the double of functions than the minimum basis set of functions, we say that we have a double-zeta valence (DZ) basis set. The same would apply if we have the triple of functions (it would be triple-zeta valence, TZ), and so on for quadruple-zeta (QZ) and pentuple-zeta (PZ). In addition, functions with higher angular momentum can be added to further improve the flexibility of the valence orbitals described; these functions are called polarization functions (and it is always recommended to use them if the computational cost allows it) and are usually denoted by a "P" after describing the type of valence split (*e.g.* TZP or DZP). Finally, diffuse functions (functions with a small exponent) are a type of function that can be added when the system possesses loosely bound electrons (like in anion, excited states or properties that depend on the wave function tail).

During the last decades, a multitude of basis sets has been developed by different research groups with, sometimes, different purposes. That is why they are catalogued by families of basis sets in which each family shares common characteristics and their own nomenclature. Some of the most popular ones are the **Pople style basis set** (*e.g.* 3-21G, 6-31G, 6-311G), **Ahlrichs type basis set** (*e.g.* SVP, TZVP, Def2SVP, Def2TZVP), and **Correlation consistent basis set** (cc-pVDZ, cc-pVTZ,cc-pVQZ).[67]

In the Pople notation, the first number refers to the number of Gaussians (or primitives) that describe the basis functions associated to inner core electrons. The following two (or three) numbers indicate how many Gaussians there are in each split of the valence orbitals. Therefore, a 6-311G basis set means that there are 6 primitives describing each basis set function associated to core electrons, the valence shell is triple split and there are 3, 1, 1 primitives for each of the valence basis functions respectively. In addition, when polarization functions are added to heavy atoms (atoms that are not Hydrogen), it is represented by adding a "*" at the end; a second asterisk means that polarization functions are also added to the orbitals of Hydrogen. The diffuse functions can also be added to heavy or Hydrogen atoms and it is represented by one or two "+", respectively. It is worth mentioning that Pople basis sets are considered outdated and possess serious deficiencies,[84] although they can be useful in some specific cases.

In the case of the Ahlrichs basis set, the number of primitives is not given in their nomenclature. Nevertheless, from the notation we can understand that SVP is a single split only for the valence orbitals (*i.e.* DZVP), with polarized functions added (in general this basis set has polarized functions added by default, which is represented with the "P" at the end of the name). Then, the other basis set TZVP, QZVP corresponds to triple- and quadruple- zeta respectively. In recent years (since 2005), this family of basis sets was redefined and greatly improved, which is denoted by the Def2 as a prefix. For example, Def2TZVP corresponds to a redefined Ahlrichs basis set with triple split and polarized functions. In general, this redefined family of basis sets is more flexible than the Pople family since they have different exponents for the s and p orbitals instead of sp orbitals (with the same exponent), which is the case in Pople basis set.

In the case of the correlation consistent basis sets, the cc denotes that they are correlated consistent, which means that they are tuned towards recovering the correlation energy of the valence electrons, and their names indicate the level of split in the valence core. Therefore, cc-pVDZ, cc-pVTZ, cc-pVQZ, cc-pV5Z and cc-pV6Z correspond to correlation consistent polarized valence Double/Triple/Quadruple/Quintuple/Sextuple Zeta (split) respectively. This type of basis sets always has polarization functions, decreasing the split of the functions with the degree of polarization. For instance, for the atoms of the second period, cc-pVTZ assigns three basis functions for the 2s and 2p orbitals, two basis functions for the 3d orbitals, and one basis function for the 4f orbitals. This basis was designed especially for post-HF methods, in such a way that the functions that contribute similar amounts of correlation energy are included in the same stage, independent of the function type. For example, the first d function provides a large energy lowering, but the contribution from a second d function is similar to that of the first f function. The energy lowering from a third d function is similar to that of the second f function and the first g function. These polarization functions should, therefore, be added in the order 1d2d1f and 3d2f1g.

A Complete Basis Set, called CBS, *a priori* requires an infinite number of basis functions. However, an approximate value for the CBS value can be obtained performing extrapolations using increasing larger basis set. CBS limit extrapolations only give reliable results if it is performed using basis sets designed specifically for the task, such as the correlation consistent basis sets, *e.g.* cc-pVxZ. At least three basis sets should be used (*e.g.* cc-VDZ, cc-VTZ, and cc-VQZ).[85–87] It is relevant to mention that the lack of completeness in a basis set generates what is called the Basis Set Superposition Error (BSSE). However, some methods have been developed to compensate this error like the Counterpoise (CP) correction or the extrapolation to CBS methods.[67]

2.3 Chemical Reactivity and Mechanistic studies with DFT.

Computational modeling of the mechanism of organometallic reactions depends on the DFT method or level of theory (usually the level of theory is described as the functional along with the basis set used). The selection of a proper DFT functional and basis set from the myriad of methods available relies on the properties that we want to study and the system (number or atoms, type of atoms, type of bonds, etc.). However, sometimes it is not that simple, and the selection of a functional requires a benchmark study that verifies the reliability of our choice. Therefore, exploring the literature in search of preexisting benchmarking that could suit your organometallic system is always recommended; even better (if you have the time and resources available) is to perform a benchmark on your own system using functionals that are trained for organometallic systems.

Although the level of theory is of paramount relevance, it is not the only factor that can affect the accuracy of a mechanistic study from the computational perspective. There are other key factors that should be addressed to ensure good accuracy and consistency in the study. These key factors are:

- Basis set
- The microscopic/structural model
- The conformational complexity
- The dispersion forces
- The solvation correction
- The entropic and temperature correction.

2.3.1 Basis set selection.

The selection of a basis set heavily depends on the number of atoms that we have in our system (more specifically the number of electrons). Hence, for systems with a considerable amount of atoms (or with more than one heavy element) it is recommended to choose a “small” basis set (with not so many functions) for calculations that require heavy computing (like geometry optimizations, frequency calculation, etc).[88–90] In computational chemistry, it is known that calculations with small basis sets contain an implicit error due to the restrictions or lack of flexibility that impose a small number of functions to describe the orbitals. Consequently, it is a common practice to perform a single point calculation with a better (more flexible or complete) basis set after the heavy calculation with a smaller one. A concrete example is the geometry optimization process. When we want to optimize a chemical system, usually we start optimizing or exploring the system with a smaller basis set, so we gain information quickly about the system, for instance what possible structures are minima or transition states. Then, once we have the stationary-point structures, single point calculations with a more robust basis set are performed to obtain more accurate properties, such as energy differences.[89]

2.3.2 Microscopic/structural model.

Since computational chemistry is still a very young science, compared to its chemical peers, there exist several chemical systems that are not that easy to represent or to model in a way that the calculations are computationally feasible. Therefore, sometimes, it is necessary to use a simplified model of the real reaction that can be computed with the computational power at hand. It is here that our chemical intuition plays a fundamental role because the selection of the model can be subjective; even if it is a simplified model the important idea is that it makes chemical sense and contains the key variables of the system. A typical example of this case is the mechanistic studies of organometallic complexes where the ligand has several triphenyl phosphine moieties (Ph_3P) and they are simplified by trimethyl phospine ones (Me_3P).[26]

2.3.3 The conformational complexity.

One of the greatest drawbacks that we face when we simulate the reactivity of an organometallic complex is the limitation of the conformational space. Indeed, it is not a trivial task to find all the plausible conformers in a metallic complex due to the flexibility of the ligand metal bonds (also depending on the ligands), which makes it quite difficult to systematize and generalize. So, the way to solve this problem is by using programs that systematically explore all the conformational and reactive space, which are computationally very expensive, or to explore “by hand” what our chemical intuition considers the most relevant conformers. Due to the computational limitations we usually face, it is common to rely on the latter method, although we should take into account that the probability that some mechanistically relevant conformers could escape our scope is moderate.

In the case of organic molecules, conformational exploration does not have these limitations since we can use molecular mechanic models that rely on force fields (very computational cheap methods) to explore quickly and easily the conformational space with acceptable accuracy; this is not the case for organometallic systems, in which metal-ligand bonds show such flexibility that describing them with force fields produce inaccurate results.

2.3.4 The dispersion forces.

Although dispersion forces (London interactions) tend to be weak, they are very relevant. As we mentioned before, one of the handicaps present in most of the DFT functionals developed a few decades ago is that they do not take the dispersion forces into account. Therefore, considering the weak London interaction as an added term in any functional can improve the capabilities of it,[91] for example, in dictating the strength of the steric interaction that can discriminate between enantiomers.

Fortunately, Grimme and coworkers have developed a method to add the dispersion effect to most of the common functionals that does account for such effect. Although it is still far from perfect, it improves the accuracy of several functionals, like the infamous B3LYP (which without the Grimme dispersion can yield fewer reliable results). However, some functionals are designed to already include the dispersion effects. For example, the highly parametrized Minnesota functional family, developed by Truhlar *et al.,* can account for the dispersion effects.[67]

2.3.5 Solvation correction.

During the first decades of DFT calculations, molecules used to be studied in gas phase or in vacuum conditions, simply because it was not computationally feasible to simulate the solvated systems in which there are thousands of solvent molecules surrounding the substrate. Even nowadays, we still struggle to compute systems that have (a lot of) explicit molecules surrounding the reactive species at the quantum level. It is possible to simulate the effect of the solvent explicitly with QM/MM methods but the results still lack the higher accuracy provided by DFT calculations.

A partial solution to this drawback was the implementation of the Polarized Continuum Model (PCM). In the PCM, the solute is described with quantum mechanics while the solvent is approximated as a structure-less continuum whose interaction with the solute is mediated by its permittivity, ε. Here, the solute can be a molecule or a cluster of molecules containing the solute and a few relevant molecules of solvent. Inside this continuum, the solute is located inside a molecular cavity constructed with interlocked spheres that are centered on the atoms of the solute. In this way, the free energy of solvation can be calculated as follows:

$$\Delta G_{solvation} = \Delta G_{cavity} + \Delta G_{dispersion} + \Delta G_{electrostatic} \tag{2.7}$$

Although this model still has disadvantages, it has been vastly improved over the last years, with a strong contribution from Tomasi, Mennucci, Cammi, and coworkers.[92,93] In our case, we used the implementation of the PCM with the formalism developed by Truhlar and coworkers: the Solvation Model based on Density (SMD).[94]

2.3.6 Entropic and temperature corrections.

Since mechanistic properties that we can compare with experimental data do not only depend on the electronic energy but rather on free energies or Gibbs energies, the correct calculation of the entropy plays a pivotal role in the mechanistic characterization of homogeneous catalysis.

The entropic expression that we rely on to describe the system is fundamentally based on the ideal gas and the rigid rotor harmonic-oscillator approximation. However, we can improve this approximation to compute more adequate entropy values (ultimately Gibbs energies) to describe reactions.

First, the change of the standard state assumed for ideal-gas conditions to the real experimental conditions can have an impact on the final value of the entropy. This is usually performed by changing the ideal-gas standard state (1 atm) and temperature (273.15K) to the standard state determined by the concentration of the reactants or the species involved ([X]= x M, where x is the concentration in molar of the species X) and the temperature of reaction (T), respectively. The calculation of this correction for the Gibbs energy is shown in the next sub-chapter.

Another relevant correction that we performed was the change from the harmonic oscillator to the quasi-harmonic approximation, which is able to correct the deviation that arises from the wrong description of the low-frequency vibrational modes of the system. From the two quasi-harmonic approximation procedures,[95,96] we use the one described by Truhlar and coworkers in which all frequencies below a cut-off are shifted to the value of the cut-off before the entropic calculations are performed.

Last year, Paton and Funes-Ardoiz developed a very practical python program, Goodvibes,[97] that can apply these and other types of corrections to computational thermochemistry calculations in a very user-friendly manner. In some of our chapters, we used this program to calculate the entropy, temperature, and concentration corrected Gibbs energies.

2.4 Calculation of the Gibbs Free energy.

In this thesis we calculated Gibbs energy differences of mechanistic steps by performing a three-step calculation. First we optimized the geometry of the species with a low level of theory B1; secondly, we performed a frequency calculation on the optimized geometry; and finally, a Single Point Energy (SPE) calculation with a more flexible basis set, B2, was performed. In this way, we obtained the electronic energy from the SPE calculations (E_{SPE}), and from the frequency calculations we obtained the entropy and the enthalpy corrections (ΔG_{corr}). Adding the previous three values together yielded the Gibbs free energy at the ideal-gas standard state (ΔG^*). In our case, ΔG^* already included the solvation energy associated with the solvent correction by using the PCM model during the optimization and single point calculations. However, the Gibbs energy associated with the change from the standard-state gas concentration of 1 atm (*) to standard state gas phase concentration equal to the experimental concentration of the different species ([X] = x M) is still missing. In order to include this correction we used the following relation:

$$\Delta G^{o/*} = \Delta G^* + RTln\left(\frac{Q^o}{Q^*}\right) \tag{2.8}$$

where Q^o is the reaction quotient (the ratio of concentrations that appears in the equilibrium constant) evaluated with all the species at the standard-state concentration given by their experimental concentration (and Q^* is the reaction quotient evaluated with all the species at the 1 atm standard-state), R is the universal gas constant (1.987 cal/(K mol)) and T is the temperature in Kelvin.

2.4.1 Calculation of the Single Electron Transfer Barrier.

The calculation of the Kinetic barrier of a Single Electron Transfer process (SET) requires a specific approach. For the SET, the free energy barrier (ΔG_{SET}) is calculated with the formalism of the Marcus approximation (commonly known as Marcus Theory for single electron transfer).[98,99] In this approximation, the barrier is defined by the Gibbs energy of the redox reaction (ΔG_{redox}) and the reorganization energy (λ) with the following expression:

$$\Delta G_{SET} = \frac{(\Delta G_{redox} + \lambda)^2}{4\lambda}, \qquad \lambda = \lambda_{is} + \lambda_{os} \tag{2.9}$$

where λ describes the sum of the inner sphere reorganization energy (λ_{is}) and the outer sphere reorganization energy (λ_{os}). The former (λ_{is}) describes the contribution due to the slight geometrical change of the molecules when the electronic states change, *i.e.*, the energy to reorganize the geometry caused by the electron transfer; and the latter (λ_{os}) corresponds to the energy required to rearrange the surrounding solvent molecules of the system. We can calculate λ_{is} as the average of total reorganization energy for products (λ_{isP}) and for reactants (λ_{isR}).

$$\lambda_{is} = (\lambda_{isP} + \lambda_{isR})/2 \tag{2.10}$$

Then, these energies can be computed as the energy difference between the ground state products with the reactants' geometry (*E(PRO)*$_R$) and the ground state products at their optimized geometry *(E(PRO)*$_{OPT}$*)*, and the energy difference between the ground state reactants with the product's geometry *(E(RE)*$_P$*)* and the ground state reactants at their optimized geometry (*E(RE)*$_{OPT}$*)*. In other words, we calculated the energy (single point energy calculation) of *E(PRO)*$_R$ by using the spin state and the charge of the products, but with the nuclear coordinates of the reactants instead of the products; and vice versa for *E(RE)*$_P$. In **Figure 2.2** this approach is shown in a clearer way.

$$\lambda_{isP} = E(PRO)_R - E(PRO)_{OPT} \tag{2.11}$$

$$\lambda_{isR} = E(RE)_P - E(RE)_{OPT} \tag{2.12}$$

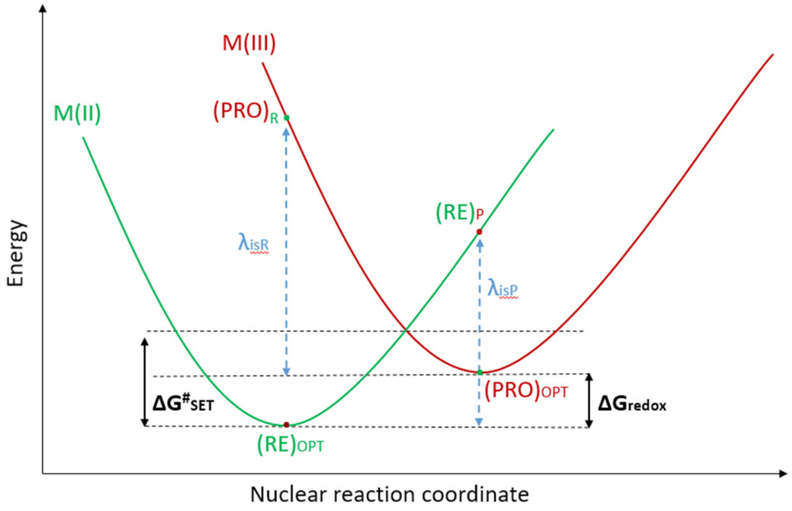

Figure 2.2 Graphical representation of the Marcus approach to calculate the components of the inner sphere reorganization energy (λ_{isR} and λ_{isP}). It shows a typical electron transfer free-energy profile for reactants and products within the Marcus model of two spheres, being $\Delta G^{\#}_{SET}$ the Marcus barrier.

On the other hand, the expression to describe λ_{os} in a continuum solvent model is as follows:

$$\lambda_{os} = (\Delta q)^2 \left(\frac{1}{2r_1} + \frac{1}{2r_2} - \frac{1}{R}\right)\left(\frac{1}{D_{op}} - \frac{1}{\epsilon_s}\right) \tag{2.13}$$

where Δq is the charge transferred, r_1 and r_2 are the radii of the reactant molecules, R is the radius of the reactant adduct, and D_{op} and ϵ_s are the static and optical dielectric constants of the solvent. The radii are computed from the sphere that corresponds to the molecular volume defined as the volume inside a contour of 0.001 electrons/Bohr^3 density (in Gaussian 09 suit,[99] the volume is calculated adding the keyword "Volume").

2.5 The Artificial Force Induced Reaction Method (AFIR).[100]

The idea behind the "artificial force induced reaction" (AFIR) is simple; it is about pushing fragments A and B together or pulling them apart. If we want to push the atoms A and B together, it can be achieved by adding a linear function of their distance r_{AB} to their diatomic potential energy, $E(r_{\mathrm{AB}})$. **Figure 2.3** shows the diatomic potential curve $E(r_{\mathrm{AB}})$, which has a barrier that separates the reactant pair A + B from the product X. Such a barrier can be eliminated by adding the term αr_{AB} to $E(r_{\mathrm{AB}})$, where α is a constant parameter. Then, the resulting function, which is shown in green, has no barrier. On this function, $E(r_{\mathrm{AB}}) + \alpha r_{\mathrm{AB}}$, the product region can be reached efficiently from the reactant pair simply by minimizing the function.

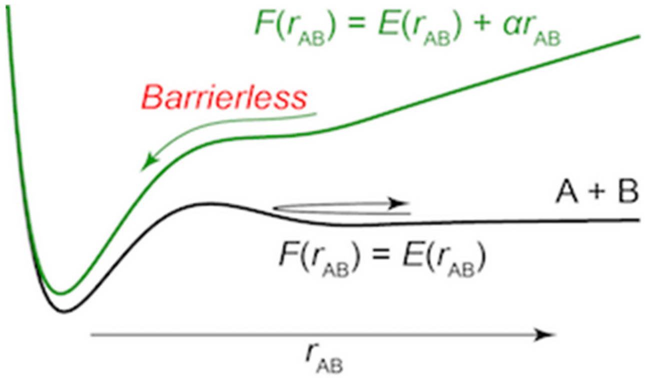

Figure 2.3 A diatomic potential curve $E(r_{\mathrm{AB}})$ between atoms A and B (black curve) and the corresponding AFIR function $E(r_{\mathrm{AB}}) + \alpha r_{\mathrm{AB}}$ (green curve). r_{AB} is the distance between A and B, and α is a constant parameter.[101]

In the case of polyatomic systems the corresponding function would be following the AFIR function:

$$F(Q) = E(Q) + \rho\alpha \frac{\sum_{i\in A}\sum_{j\in B}\omega_{ij}r_{ij}}{\sum_{i\in A}\sum_{j\in B}\omega_{ij}} \tag{2.14}$$

where the first term is the potential energy surface (PES) $E(\mathbf{Q})$ of geometrical parameters $\mathbf{Q}$ and the second term is the artificial force. The parameter α in the artificial force term determines its strength. The coefficient ρ is either 1 to push fragments together or −1 to pull them apart. The force term is given as a weighted sum of the distances r_{ij} between the atom i in the fragment A and the atom j in the fragment B, and the weight function ω_{ij} is defined as:

$$\omega_{ij} = \left[\frac{R_i + R_j}{r_{ij}}\right]^6 \tag{2.15}$$

where $R_i + R_j$ is the sum of covalent radii of atoms i and j, to treat all elements equivalently. This weight function, ω_{ij}, assigns a stronger force to the pair of atoms that are closer and a weaker force to the more distant ones.

For convenience, the parameter α is determined by the following equation:

$$\alpha = \frac{\gamma}{\left[2^{\frac{-1}{6}} - \left(1 - \sqrt{1 + \frac{\gamma}{\epsilon}}\right)^{\frac{-1}{6}}\right] R_0} \tag{2.16}$$

where the standard Ar-Ar parameters of the Leonnard-Jones (LJ) potential, $R_0 = 3.8164$ Å and $\varepsilon = 1.0061$ kJ mol^{-1}, are employed. In this context, $\boldsymbol{\alpha}$ corresponds to the mean force that acts on two atoms in their direct collision on the Lennard–Jones (LJ) potential with collision energy $\boldsymbol{\gamma}$, in the area from the minimum to the turning point.

The collision-energy parameter γ defines an approximate upper limit to the barrier height that can be overcome by the force term. The γ parameter is usually selected depending on the highest transition state energies searched. The γ parameter can also be based on experimental conditions, such as temperature T, reaction time t, etc. It must be highlighted that the γ value is usually decided assuming the rate constant k of the standard transition state theory:

$$k = \frac{k_B T}{h} \exp\left[-\frac{\Delta\Delta G^{\neq}}{RT}\right] \tag{2.17}$$

where $\Delta\Delta G^{\ddagger}$ is the overall activation Gibbs energy, k_B is the Boltzmann constant, T is the temperature, h is the Planck constant, and R is the gas constant. The reaction time t can be estimated as the inverse of the rate constant ($t \approx 1/k$). Therefore, substituting $k = 1/t$ and taking the inverse and the natural logarithm of the both sides, the γ required to overcome a barrier of $\Delta\Delta G^{\ddagger}$ can be expressed as follows:

$$\gamma = RT\left(\ln t - ln\frac{h}{k_B T}\right) \tag{2.18}$$

It is important to remark that t should be set to a larger value than the time of the actual reactions because γ provides just an approximate upper limit of the barrier height. Thus, t is usually set to ten times its real value ($t = 10\ t_{\text{actual}}$).

Notably, if a large value of γ is given, many high barrier pathways (that are not important in a given experimental condition) will be obtained, and such exhaustive searches incur very large computational costs. Therefore, one must be quite reasonable and use an adequate (not too large) γ value.

AFIR calculations can be perform with three different algorithms: Single Component AFIR (SC-AFIR), Multi-Component AFIR (MC-AFIR), and Double-Sphere AFIR (DS-

AFIR). In our case, we will briefly introduce the basics of SC-FIR and DS-AFIR. MC-AFIR is out of the scope of this thesis.

2.5.1 Single Component AFIR (SC-AFIR) algorithm.

In this case we have only two fragments, just like the model used in the description of the general AFIR method. However, the fragments do not necessarily need to be single molecules, they can be H-bond clusters, metal clusters, Van de Waals complexes, organometallic complexes, and so on.

The idea is to find approximated minima and transition state structures by exploring the PES via the AFIR path (which is the path that the system follows under the influence of the AFIR function). There are several AFIR paths and their selection relies on the departure structure (EQ) and the fragments that we select in it. Finally, for a departure structure EQ, the fragments are defined systematically until all of them are explored, unless asked otherwise to the program.

If we focus on the two atoms k and l, a perturbed structure is generated by decreasing (or increasing) their distance by ξ% (20% by default). Then, with the distance k-l fixed, the structure is reoptimized. In the perturbed structure, fragments A and B are defined around the atoms k and l. First, k and l are included in A and B, respectively. Then, all atoms connected to A or B are included in A or B, accordingly, where atoms *i* and *j* are regarded to be connected if $r_{ij}/(R_i+R_j) < 1.5$. This selection is performed twice and atoms directly connected to k and l (first layer) and those connected to them (second layer) are included in A and B, correspondingly. Finally, atoms *i* in A are excluded from B and atoms *j* in B are excluded from A, when $r_{ij}/(R_i+R_j) < r_{kl}/(R_k+R_l)$. In **Figure 2.4** a schematic illustration for an alkyl-CO-carbonyl complex is shown, where the asterisks mark the two atoms k and l.

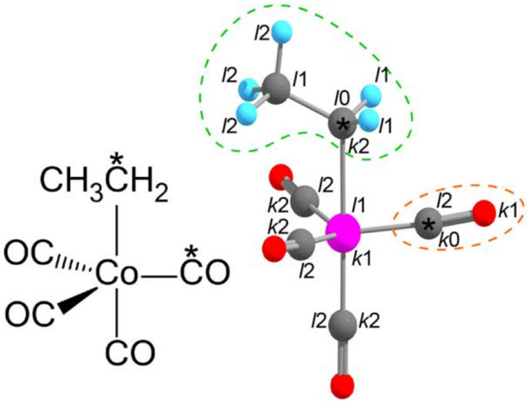

Figure 2.4 Fragment generation around carbon atoms with asterisk marks.

k0 corresponds to k itself, k1 corresponds to atoms immediately connected to k, and k2 corresponds to the ones connected to k1 atoms. Excluding atoms ki (i>0) and lj (j>0) that exist between k0 and l0, the fragments indicated by dashed circles are obtained. Then, with these fragments the minimization of the AFIR function will yield a path that connects the reaction between these two ligands (it yields an aldehyde-like group). In this way, if we select another two different atoms as the new k and l, and repeat the process to get two different fragments, the algorithm explores several pathways systematically, changing the selected atoms automatically to define the new fragments.

Once an AFIR path is found, the stationary points of the approximated PES are reoptimized and connected by IRC calculations at a reasonable DFT level of theory. The DFT reoptimizations can be done “manually” or by explicitly asking the program to do so.

2.5.2 Double-Sphere AFIR (DS-AFIR) algorithm.

What makes this algorithm useful is that it can find a single path linking two given structures. It can even be applied to multistep paths that have more than one transition state. However, the path does not precisely correspond with the kinetically most favorable path but to the shortest one.

During the DS-AFIR the following function is minimized:

$$F^{DS-AFIR}(\boldsymbol{q}_i) = E(\boldsymbol{q}_i) + XY\left|\boldsymbol{q}_i - \boldsymbol{p}_j\right| - X(1-Y)|\boldsymbol{q}_i - \boldsymbol{q}_0| \tag{2.19}$$

where $\mathbf{q}_i$ and $\mathbf{p}_j$ correspond to the current position of the two end-points, X is a parameter given as

$$X = \frac{\delta}{|\mathbf{u}|} - \frac{\mathbf{g_i} \cdot \mathbf{u}}{|\mathbf{u}|^2} \tag{2.20}$$

where $\mathbf{g}_i$ is the PES gradient at $\mathbf{q}_i$ and δ is a parameter. The vector $\mathbf{u}$ is defines as

$$\mathbf{u} = Y\frac{(\boldsymbol{q}_i - \boldsymbol{p}_j)}{\left|\boldsymbol{q}_i - \boldsymbol{p}_j\right|} - (1-Y)\frac{(\boldsymbol{q}_i - \boldsymbol{q}_0)}{|\boldsymbol{q}_i - \boldsymbol{q}_0|} \tag{2.21}$$

where the parameter Y is gives as

$$\begin{aligned} Y &= \frac{Z}{1-Z} \qquad if\ Z > 0 \\ Y &= 0 \qquad\quad\ \ if\ Z \leq 0 \end{aligned} \tag{2.22}$$

using the parameter Z as follows:

$$Z = \frac{|\boldsymbol{q}_i - \boldsymbol{q}_0|}{|\boldsymbol{q}_i - \boldsymbol{p}_j|} + (1 - Y)\frac{(\boldsymbol{q}_i - \boldsymbol{p}_j) \cdot (\boldsymbol{q}_i - \boldsymbol{q}_0)}{|\boldsymbol{q}_i - \boldsymbol{p}_j||\boldsymbol{q}_i - \boldsymbol{q}_0|} \tag{2.23}$$

In **equation (**2.19, we have two forces (second and third terms). The first one (second term) applies forces that make the distance between the two points shorter while the other one (the third term) pushes the current point **q**ᵢ away from the reference point **q**₀, which corresponds to the latest local minimum **q**ₖ along the AFIR path and initially set to the given end-point **q**₁. The parameter X in **equation 2.20** imposes the condition that the component of the derivative of **equation 2.19** along the vector of the sum of two force terms becomes δ. E**quation 2.22** and **equation 2.23** control the weight of the second force term to become larger than that of the first force term around local minima. Conversely, the first force term gets the larger weight around ridges between two minima.

In **Figure 2.5**, we show a scheme for the construction of a DS-AFIR path.

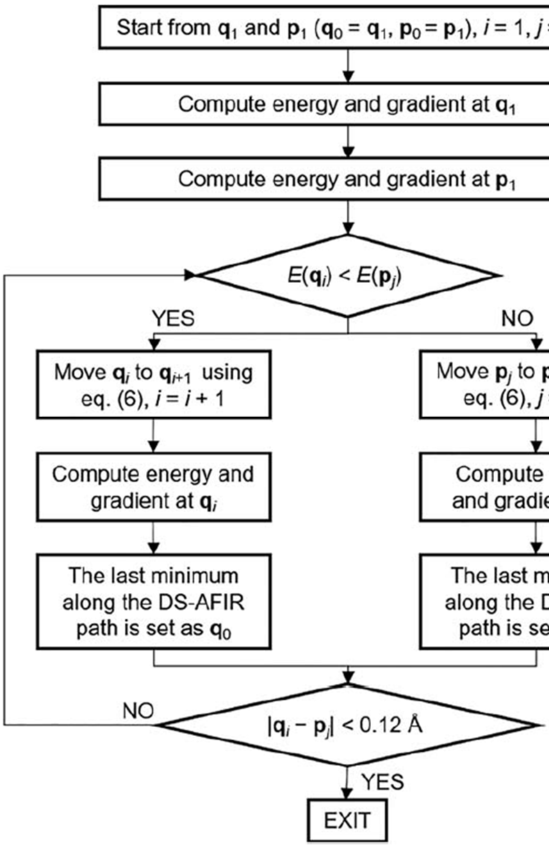

Figure 2.5 Calculation flow for DS_AFIR (taken from reference 25). Here "eq. (6)" refers to the previously described **equation 2.19**.

At first, energy and gradient are computed at the two given end points $\mathbf{q}_1$ and $\mathbf{p}_1$. Then, at an arbitrary step (any point between $\mathbf{q}_1$ and $\mathbf{p}_1$), the one with lower energy is chosen out of $\mathbf{q}_i$ or $\mathbf{p}_j$ and moved to $\mathbf{q}_{i+1}$ or $\mathbf{p}_{j+1}$ by the LQA method on the function of **equation 2.19**, where the second force term is omitted at $\mathbf{q}_1$ and $\mathbf{p}_1$ because these points are identical to the reference points $\mathbf{q}_0$ and $\mathbf{p}_0$, respectively. Then, energy and gradient at the newly obtained point are computed. Before entering the next cycle, the last local minimum along the potential curve is set as $\mathbf{q}_0$ or $\mathbf{p}_0$. This procedure is repeated until the two end points approach each other sufficiently, where the threshold is 0.12 Å $>|\mathbf{q}_i-\mathbf{p}_j|$. Following the DS-AFIR algorithm one finds the shortest path that connects the initial $\mathbf{q}_0$ and $\mathbf{p}_0$ structures. Again, as in the last step, the stationary points of the AFIR path are reoptimized and connected with IRC calculations at DFT level.

Chapter 3

Objectives

As a general objective of this thesis, we wanted to use computational tools (especially DFT) to comprehend the behavior of four organometallic reactions or catalysis with first-row transition metals developed in our research labs (QBIS-CAT group). Our end goal was to achieve a synergic collaboration between the theoretical and experimental chemistry to obtain deeper understanding of the mechanism of the four reactions studied. Therefore, in this work four sets of specific goals were settled for those four reactions:

"Mechanistic aspects of the Aryl-Co(III) masked-carbene formation with diazo esters."

- To give insight into a possible mechanism for the reactions of diazoacetates with a well-defined Co(III)complex.
- To explain the effect of the Lewis-acid additives (like Li(OTf)) in the mechanism.
- To corroborate computationally the effects of changing some variables (the nature of the enolate ligand in the Co(III) complex, the electronic character of the diazo ester, the strength of the nucleophile) in the reaction, and the effect that they have in the mechanism or the RDS (rate-determining step).

"Insight into the Trifluoromethylation Mechanism of a Well-Defined Aryl-Ni(II) Species via Putative Ni(IV) or Ni(II) Intermediates."

- To find a plausible mechanism that explains the detailed steps of the trifluoromethylated reaction.
- To verify if the reaction proceeds via two-electron or one-electron mechanism.
- To propose modifications of our complex to reduce the barrier of the rate-determining step of the mechanism. The efficiency of the new catalysts will be explored computationally in order to determine which of the different new suggested complexes could be worth synthesizing.

"Nickel-Catalyzed Aromatic homologation by Alkyne Insertion versus Alkyne mono-annulation by reductive elimination."

- To propose a mechanistic explanation of the C-F activation selectivity over the C-H activation.
- To propose a mechanism that explains the preference of the reaction to form the aromatic homologation product instead of the mono-annulated one.

"On-ligand amine-to-amide formation by CO insertion on a well-defined Iron(II) complex."

- To explore computationally different possible mechanisms that could explain the unexpected CO insertion that yields the amide product within the ligand scaffold.
- To use the AFIR algorithms as an alternative tool to find possible paths of reaction that could explain the reactivity of the Iron(0) complex.

Chapter 4

Mechanistic Aspects of the Aryl-Co(III) Masked-carbene Formation with Diazo Esters

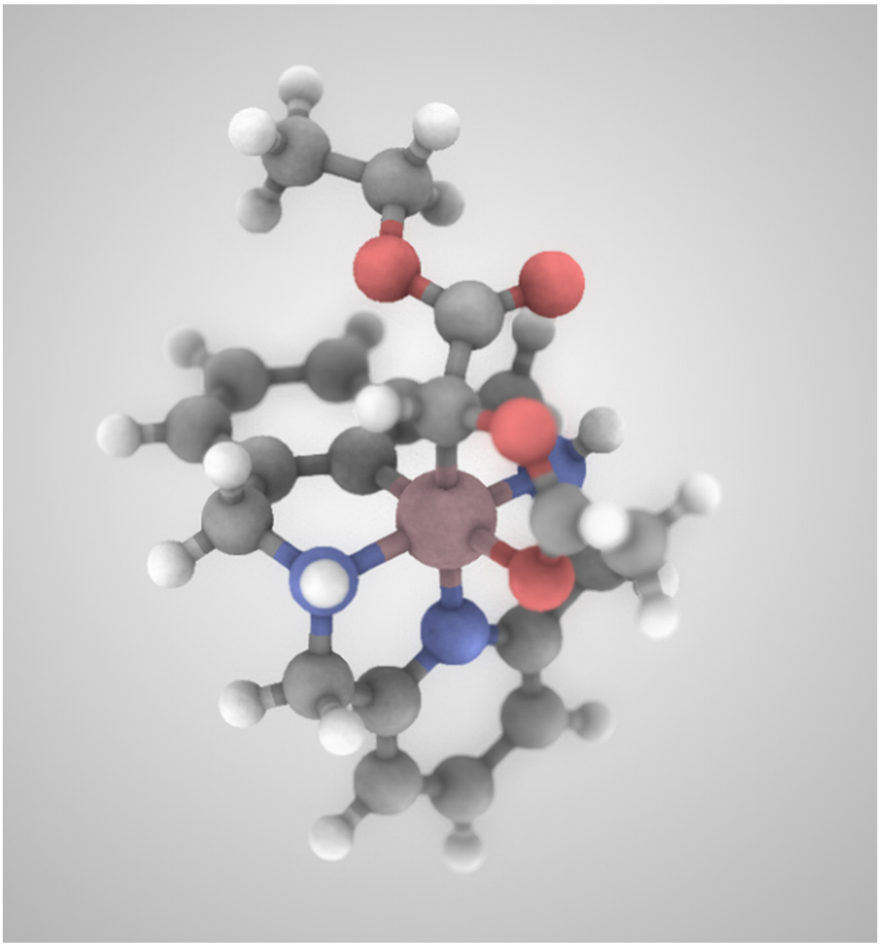

*This chapter corresponds to the theoretical calculations developed for the following publications:

Planas, O.; Roldán-Gómez, S.; Martin-Diaconescu, V.; Luis, J. M.; Company, A.; Ribas, X. Mechanistic Insights into the SN2-Type Reactivity of Aryl-Co(III) Masked-Carbenes for C-C Bond Forming Transformations. *Chem. Sci.* **2018**, *9* (26), 5736–5746. (doi:10.1039/c8sc00851e)

Planas, O.; Roldán-Gómez, S.; Martin-Diaconescu, V.; Parella, T.; Luis, J. M.; Company, A.; Ribas, X. Carboxylate-Assisted Formation of Aryl-Co(III) Masked-Carbenes in Cobalt-Catalyzed C-H Functionalization with Diazo Esters. *J. Am. Chem. Soc.* **2017**, *139* (41), 14649–14655. (doi:10.1021/jacs.7b07880)

Summary

In this chapter we present some of the computational work developed to comprehend the mechanistic aspects of the formation of a family of C-metalated aryl-Co(III) enolates (masked-carbenes) when using diazoacetates as coupling partners. We show the computational results obtained by exploring the different factors that affect the reaction (the presence of additives, the type of carbene, the electronic properties of masked-carbene, etc) and how they all agree with the proposed mechanism of the aryl-Co(III) masked-carbene as the key intermediate in the formation of the C-C bond.

4.1 State of the art.

In recent years, transition metal catalyzed C-H activation has emerged as a powerful and versatile tool in organic synthesis.[102–104] The vast majority of such transformations have been achieved with precious metals like Pd, Ru and Rh. However, new methodologies implementing cost-efficient 3d transition metals have gain attention in the field lately.[18,105–107] In particular, cobalt catalysis has emerged as a valuable asset for the synthesis of different sorts of molecules due to the polarized character of the C-Co bond (compared to the other member of the group 9).[108–111] In general, two types of Co-catalyzed functionalization can occur, the low-valent[65,108] or the high-valent approach.[112]

High-valent cobalt catalysis has been explored and used thoroughly but mainly with Cp*Co(III)[109–111] as well as N,N-bidentate-chelating directing groups.[113] Studies to fully understand the mechanism or pathway of these transformations are still in their infancy[61], and so far it has been proposed that an organometallic Co-(III) intermediate species is usually involved.[114–117]

The use of carbene precursors as coupling partners in Co-catalysis has recently attracted attention due to its efficiency in transformations like carbonylations[118,119] and annulations,[120–126] including Co-radical-based outer-sphere functionalizations (**Figure 4.1a**). In the case of inner-sphere functionalizations, Cp*Co(III) catalysts with diazo esters as coupling partners allow the functionalization of C-H bonds[127–131] (**Figure 4.1b**). Such Co(III) reactivity is currently rationalized by the formation of an elusive Co(III)-carbene (B, **Figure 4.1c**), which can undergo migratory insertion to yield the respective alkyl-Co(III) intermediate (C, **Figure 4.1c**)[132], like in a typical migratory insertion step from a metal-carbene functionalization reaction.[133]

Recently, in our group, we developed a family of aryl-Co(III) complexes via C-H activation[134] by using a macrocyclic model substrate which has been proven to stabilize other organometallic high-valent aryl/alkyl-metal intermediate species. Such complexes showed catalytic capabilities in alkyne annulation reaction yielding either five or six membered-ring products. Then, based on the capabilities of our complexes and the increasing interest in carbene surrogates for the formation of C-C bonds, we decided to study experimentally (work performed by other members of the group) and computationally (work performed by the author of this thesis) the reactivity of the reported aryl-Co(III) complexes (and some derivatives of it) with diazo esters to elucidate the operative mechanism as well as the nature of the key intermediates.

In this chapter we present the **computational results** that support the existence (aligned with the experimental evidence) of a unique C-metalated *cis*-aryl-Co(III)alkyl enolate intermediate that can be assumed as a "tamed" version of the highly reactive Co-carbenes (masked-carbene). Interestingly, this masked-carbene can be used to construct C-C bonds via an unusual S_N2-like pathway. In addition, we present a computational study that rationalizes the electronic and steric effects that govern their formation and their reactivity.

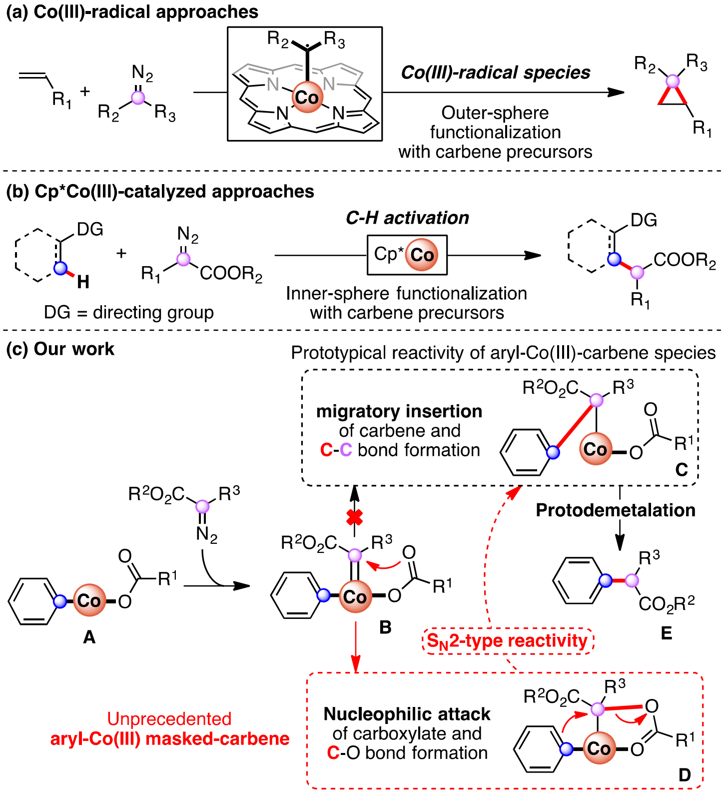

Figure 4.1 Reactivity of Co(III) species with diazo acetates: **(a)** functionalization through Co(III) radical species; **(b)** C-H Activation utilizing Cp*Co(III) catalysts; **(c)** Prototypical migratory insertion mechanism (black) and our work, which proved the existence of new intermediates utilizing macrocyclic model substrates (red).

4.2 Computational Details.

We used Gaussian 09 package[99] to perform all calculations. All geometry optimizations and frequency calculations were carried out with the BP86 functional[76,77] and the def2-TZVP basis set developed by Ahlrichs.[135,136] Empirical dispersion and solvation effects in 2,2,2-TriFluoroEthanol (TFE) were included using Grimme's DFT-D3 approach[137] and PCM-SMD method[94] respectively. All transition states were connected to the corresponding reactants and products with IRC calculations. To refine the final free energy values we carried out Single Point Energy (SPE) calculations at the optimized geometries with the B3LYP[79,81,138,139] functional and def2-TZVP basis set, including PCM-SMD and GD3-dispersion corrections (E_{B3LYP}). The free energy change associated with the change from a standard-state gas concentration of 1 atm to a standard state gas phase concentration of 1 M for the solutes ($\Delta G^{o/*}$) was also included in the final free energies values. In this case, $\Delta G^{o/*}$ at 298.15 K is 1.89 kcal/mol for 1 M standard state solutes. Entropic and Enthalpic corrections were obtained from frequency calculations at 298.15 K (G_{corr}). Then, the final total Gibbs free energy (G) was given by:

$$G = E_{B3LYP} + G_{corr.} + \Delta G^{o/*} \text{ (Equation 1)}$$

Moreover, to check the reliability of the obtained BP86/B3LYP results, we optimized some of the obtained structures with the functional M06L.[82]

4.3 Results and Discussions.

The initial experiments to find the optimum conditions of the reaction are shown in **Table 4.1**, where the complex **2a-OAc** (our organometallic aryl-Co(III) species) reacts with Ethyl diazoacetate (EDA) to yield **3**.

Table 4.1 Evaluation of the stoichiometric conditions

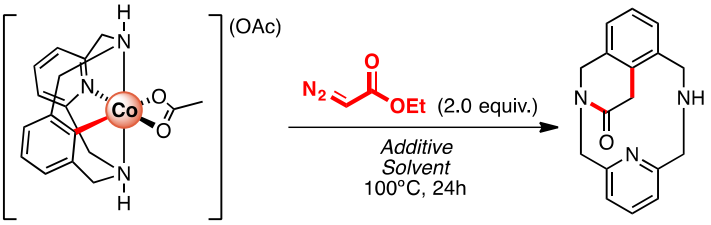

2a-OAc

3

Entry	Additives (equiv.)	Solvent	Yield of 3 (%)[a]
1	None	ElOH	0%
2	None	TFE[b]	10%
3	None	HFIP[c]	31%
4	AcOH (1.0)	TFE	15%[d]
5	H_2O (1.0)	TFE	57%
6	H_2O (2.0)	TFE	82%
7	**H_2O (4.0)**	**TFE**	**96% (91%)[e]**
8	$Mg(OTf)_2$ (1.0)	TFE	67%
9	H_2O (1.0) + $Mg(OTf)_2$ (1.0)	TFE	92% (87%)[e]
10	**Li(OTf) (1.0)**	**TFE**	**95% (88%)[e]**
11	H_2O (4.0)	EtOH	88%
12	Li(OTf) (1.0)	EtOH	91 %

[a] Yield determined using 1,3,5-trimethoxybenzene as the internal standard. [b]2,2,2-trifluoroethanol (TFE). [c]1,1,1,3,3,3-hexafluoro-2-propanol (HFIP). [d]Proto-demetalation of **2a-OAc** was observed. [e]Isolated yield.

The data of **Table 4.1** shows that the reaction does not work effectively in the absence of an additive (in this case, H_2O or a Lewis acid like Li(OTf)). However, interestingly, when the reaction is performed in strictly anhydrous conditions without additives, after fifteen minutes the reaction accumulates enough material of an intermediate that was characterized by spectroscopic analysis (HRMS and NMR); in the first analysis of the results, it was believed to be a carbene intermediate (see below).

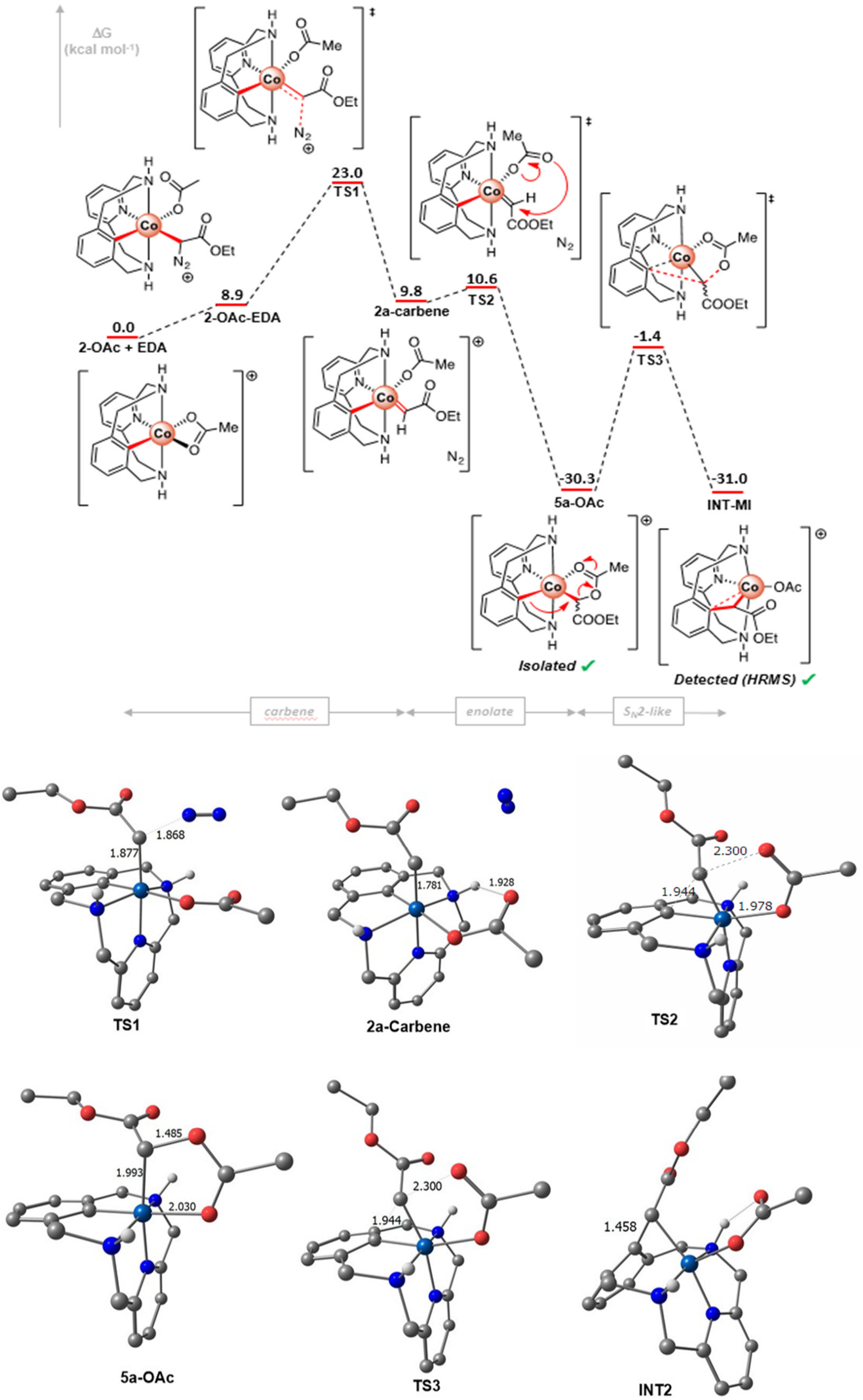

Figure 4.2 Gibbs energy profile of the reaction with some of the relevant calculated structures (Hydrogens were omitted for clarity). Relative Gibbs energy values are given in kcal/mol.

Based on this initial information, we tried to find a plausible mechanism for the reaction, first, in the absence of additives. **Figure 4.2** shows the Gibbs energy profile of the reaction for such a case. The first barrier (**TS1**) corresponds to the addition of the EDA to the Complex **2a-OAc** and the simultaneous release of N_2 to generate the carbene complex **2a-carbene**. Once the carbene is formed, an almost barrierless intramolecular attack from the enolate to the carbene occurs (**TS2**), which yields the thermodynamically stable intermediate **5a-OAc** (~40 kcal/mol more stable than the previous intermediate). **5a-OAc** is followed by the **TS3** barrier (28.9 kcal/mol) which corresponds to an S_N2-like transition state with the acetate acting as the leaving group and the aryl-Co bond as the nucleophile, to finally yield the intermediate **INT-MI** with a very small thermodynamic Gibbs energy gain. From this profile of DFT Gibbs energy, it is clear that the rate-determining step (RDS) is determined by the **TS3** barrier (~29 kcal/mol), which is in line with the low yield of this reaction at the given conditions (at 100 ºC, 29 kcal/mol is quite close to the upper limit of Gibbs energy allowed to the reaction to proceed).

It is relevant to mention that we first thought that the intermediate was a carbene. However, our DFT calculations predicted that, surprisingly, the intermediate was the **5a-OAc** species, which was later confirmed experimentally by the crystal structure of analogous species (replacing the acetate anion with *p*-substituted benzoates). Although **5a-OAc** is not exactly a carbene moiety, it can be considered as a "tamed or masked" carbene because it reacts like the carbene. Nevertheless, the cyclized form (**5a-OAc**) is far more stable than the aryl-Co(III) carbene enolate species (2**a-carbene**). In addition, it was possible to detect the intermediate **INT-MI** by HRMS when MS/MS analysis was performed to some derivatives of **5a-OAc**. The fact that we can accumulate intermediate **5a-OAc** during the reaction corroborates the hypothesis that **TS3** is the rate-determining step.

To ensure that our computational results were not biased by the functional selection, we compared the B3LYP Gibbs energy profile with their counterparts computed with M06 and BP86 functionals. As we can see in **Figure 4.3**, the trends obtained with the three functionals were similar. The main difference is that with M06L it was not possible to find the unstable carbene species and at this level **TS1** is directly connected to **5a-OAc**.

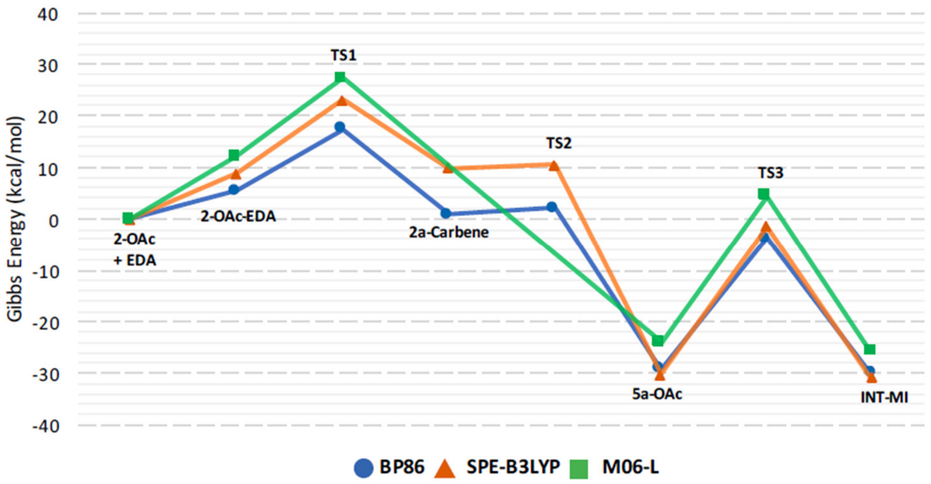

Figure 4.3 Gibbs Energy profiles described by DFT at three different level of theory (BP86, M06L, and B3LYP(SPE)//BP86). All the values are relative Gibbs energies referenced to their corresponding reactants' Gibbs energies at infinite distance.

4.3.1 The effect of the additive in the mechanism.

Now that we have a better insight of the reaction without additives, it is logical to proceed to the reaction with them. According to the experimental results, the additives (water and Lewis acids) were able to improve the yield of the reaction. However, when we used a Brønsted acid there was some decomposition of the product and the yield was quite low (see **Table 4.1**), which led us to think that maybe the reactant **2a-OAc** was sensitive to Brønsted acids. In fact, when the isolated **5a-OAc** was put back into reactive condition with additives, we obtained decent yields of product **3** (**Figure 4.4**), even with AcOH.

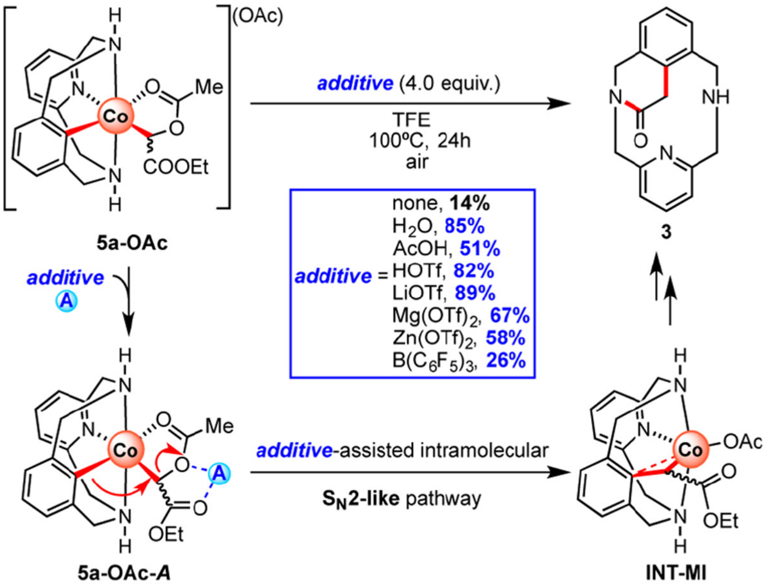

Figure 4.4 Evolution of **5a-OAc** to **3** with additives and rationalization of the observed reactivity.

Based on the mechanism without additives and taking into account that the intermediate **5a-OAc** can furnish **3** by using the additive, we hypothesized that the additive must be playing a role as a coadjutant in the S$_N$2-like transition step, facilitating the exit of the leaving group.

Moving forward, we also computed the S$_N$2-like step in the presence of an explicit atom of Li$^+$ acting as a Lewis acid to explain why the LiOTf considerably improved the yield of **3** starting from **5a-OAc** or **2a-OAc**. Surprisingly, when the Li$^+$ interacts with the enolate and the carbonyl moiety of the intermediate, the molecule is stabilized (see **Figure 4.5**). Then, **TS3-Li** is a barrier of only 22.6 kcal/mol, much lower than **TS3** (with a difference of ΔΔG= 6.3 kcal/mol). Moreover, this reaction step becomes exergonic by almost 13 kcal/mol. Indeed, these results show that the enolate leaving group plays a fundamental role in the mechanism, and the ability of the Lewis acid (LA) to make the enolate a better leaving group (via LA-mediated carboxylate activation) diminishes the energy of the rate-determining step of the reaction.

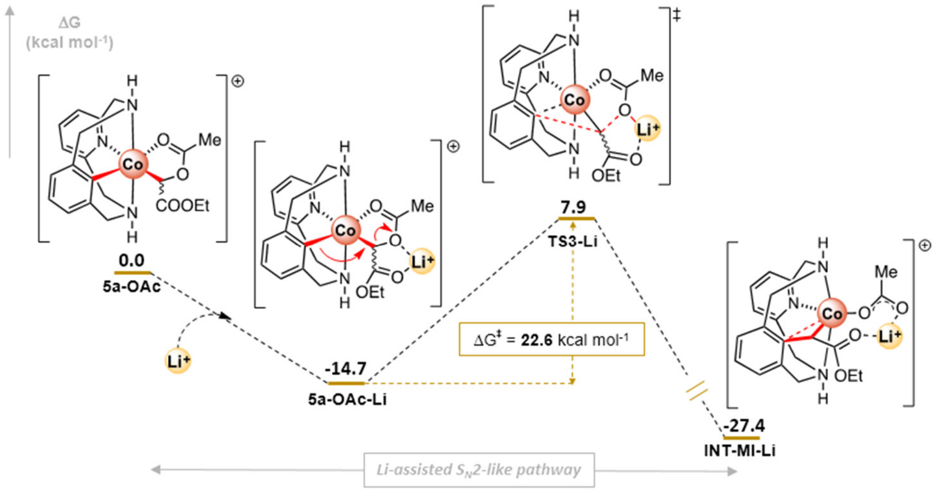

Figure 4.5 Gibbs energy profile of the S$_N$2-type step in the presence of Li$^+$. Relative Gibbs energy values are given in kcal/mol.

Taking into account that the results were in agreement with the experiment, we decided to further explore the effect of the Lewis Acid. With this proposal, we performed experiments with different Lewis acids but this time in a more systematic way to study any pattern in their behavior. As **Figure 4.6** shows, we found out that the stronger the Lewis acid, the better the yield. However, the size of the Lewis acid also negatively affects the yield.

Then, we decided to calculate the intramolecular S$_N$2-like step using LiOTf, NaOTf, KOTf as additives respectively (we chose the Lewis acid of the alkali metals because they bear the same charge, and so the error due to not adding the counter ions will be similar). To our delight, the DFT results were in agreement with the experiments, with Li having the strongest effect over the RDS followed by Na and K respectively (**Figure 4.7**).

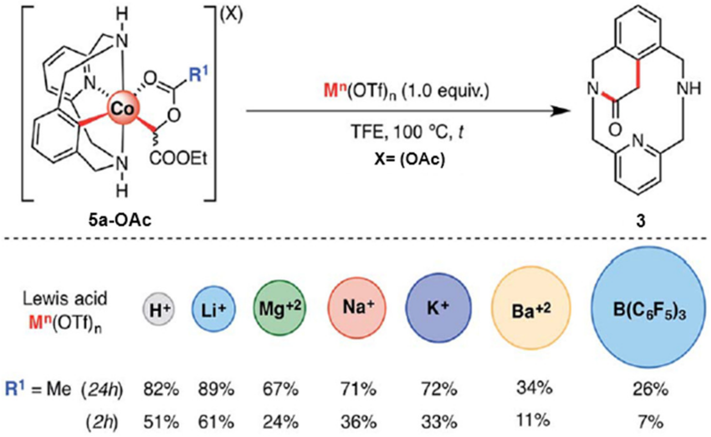

Lewis acid $M^n(OTf)_n$		H^+	Li^+	Mg^{+2}	Na^+	K^+	Ba^{+2}	$B(C_6F_5)_3$
R^1 = Me	(24h)	82%	89%	67%	71%	72%	34%	26%
	(2h)	51%	61%	24%	36%	33%	11%	7%

Figure 4.6 Evolution of organometallic **5a-OAc** intermediates to **3** in the presence of several Lewis acids as additives.

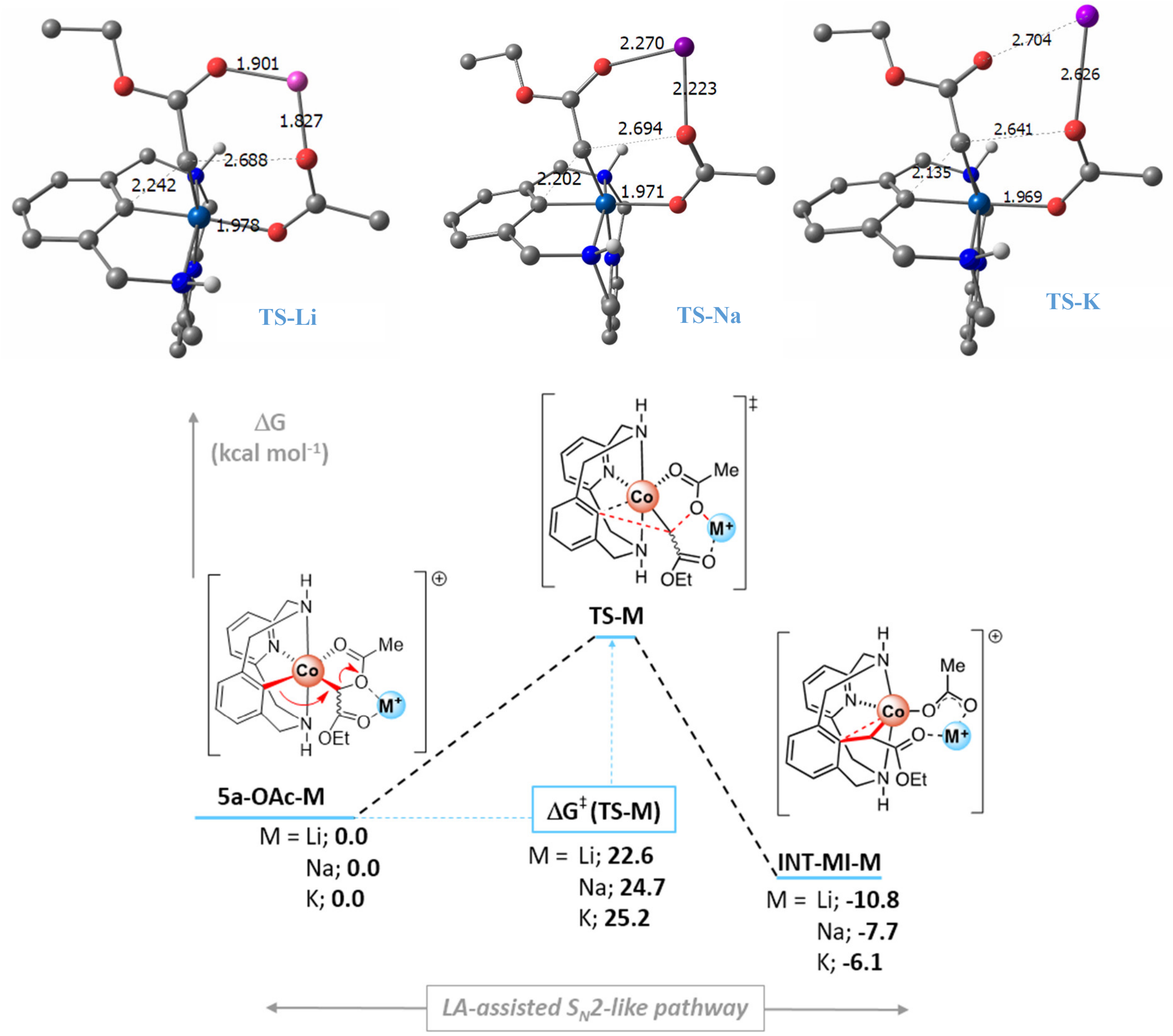

Figure 4.7 Gibbs energy profile of the S_N2-type event in the presence of several M^+ cationic Lewis acids (M = Li, Na and K). Relative Gibbs energy values are given in kcal/mol. On top we have the optimized geometries of the different **TS-M**.

Furthermore, we explored the stabilization of the metal cation by adding explicit molecules of solvent to **5a-OAC-Li**, **5a-OAC-Na**, and **5a-OAC-K** (**Figure 4.8**, (**a**)). Using Li as an illustrative example, we found that we needed at least three molecules of explicit solvent to stabilize the metallic cations. As **Figure 4.8 (b)** shows, the energy difference is relatively small for the change from two to three molecules of 2,2,2-trifluoroethanol (TFE) coordinated to Lithium cation. This means that (as a rough approximation) three molecules of TFE are enough to stabilize the cation. Although the effect of the solvent molecules decreases the exergonicity of the reaction of **5a-OAC** with the LA, our results showed that their interaction is clearly favorable.

(a) Stabilization effect of M⁺ cations with 4a-OAc

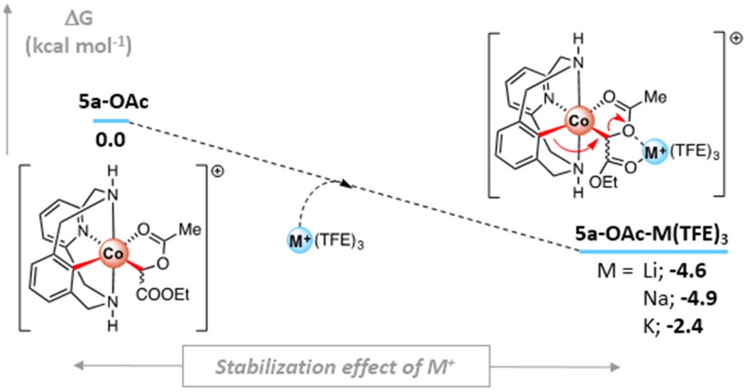

(b) Stabilization effect of Li⁺ cation in 5a-OAc-Li with additional TFE

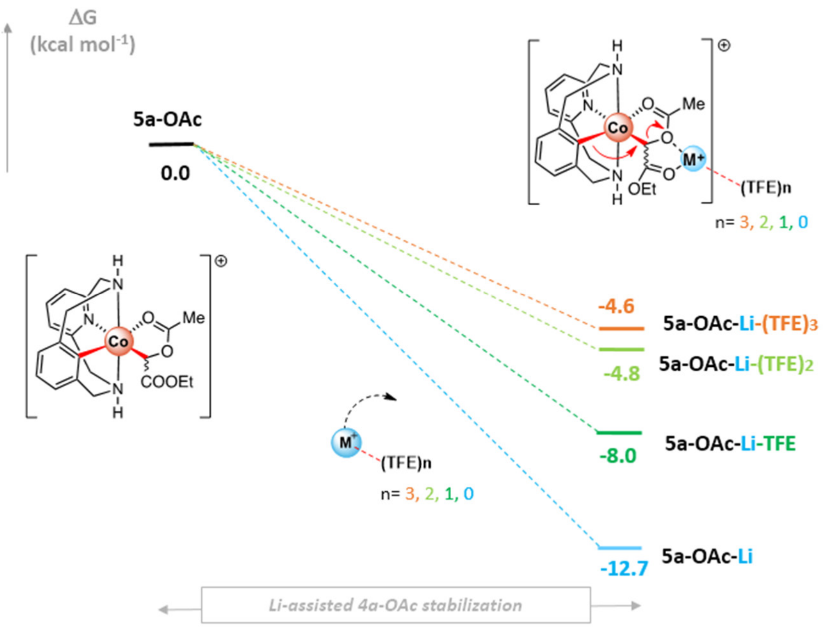

Figure 4.8 (a) DFT Gibbs energy of the adduct formation when **5a-OAc** is mixed with M+ cationic Lewis acids (M =Li, Na and K) taking into account the presence of three explicit TFE molecules.**(b)** Gibbs energy of the TFE-solvated lithium cation binding to **5a-OAc** when 0, 1, 2, 3 molecules of TFE are explicitly considered. Relative Gibbs energy values are given in kcal/mol. [M⁺]= 0.039 mol/L.

4.3.2 Effect of varying the enolate in the mechanism (**2a-OAc** derivatives).

Once we knew that the enolate played an important role as the leaving group in **TS3** and related transition states, we decided to study experimentally and computationally the effect of changing the electronic structure of the enolate by means of using enolate derivatives with different electronic properties.

As **Table 4.2** shows, we were able to synthesize some **2a-X** complexes that yielded product **3a** in relatively good yields except for entry 2 and 3. It is worth highlighting that in the case of the carboxylates **2a-OPiv** and **2a-OTPA**, the yields were quite low for the former and only traces for the later. This indicates that the bulkiness or steric effect of the leaving group considerably affects the reaction.

Table 4.2 Reaction of **2a-X** with EDA to furnish cyclic amide.

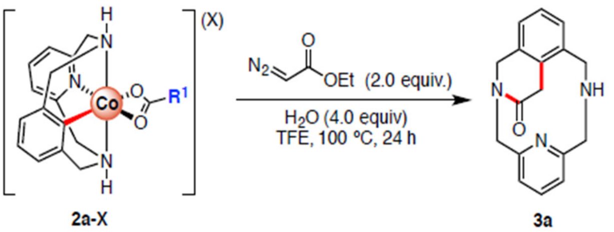

Entry	R^1 (R^{1}CO$_2$)	Yield of 3 (%)[a]
1	**Me (OAc)**	**91%**
2	Piv (OPiv)	23% (20%)[b]
3	**CPh$_3$ (TPA)**	**Traces**
4	CF$_3$ (TFA)	75%
5	Ph (OBz)	78%
6	*p*-OMe-Ph (OBz-OMe)	71%
7	*p*-Me-Ph (OBz-Me)	72%
8	*p*-Cl-Ph (OBz-Cl)	81%
9	*p*-COMe-Ph (OBz-COMe)	85%
10	*p*-CN-Ph (OBz-CN)	80%
11	*p*-NO$_2$-Ph (OBz-NO$_2$)	81%

[a] Isolated yield after silica gel cromatography.
[b] Reaction in presence of 1.0 equiv. of LiOTf.

In addition, it is at this point that we were able to isolate and crystalize some derivatives of the intermediates **5a-X** under anhydrous conditions (**Figure 4.9**), which confirmed the structures of the intermediates **5a-X**. Moreover, those structures matched with the ones obtained computationally (see below).

Since we wanted to study the effect of the substituted enolate in the mechanism, we calculated the whole mechanism for each one of them based on the initial mechanism in anhydrous condition. The results, presented in **Figure 4.10** and **Table 4.3**, show that in several cases it was not possible to obtain the structure of the carbene **2a-carbene-X**, since

TS1 was directly connected to **5a-X.** These results suggest that if **2a-carbene-X** exists, it is a very unstable species.

Furthermore, even when **2a-carbene-X** exists, the barrier **TS1b** is so small that it was not possible to optimize for several derivatives.

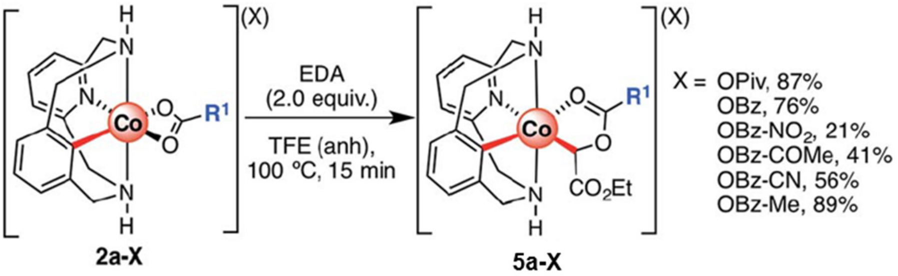

Figure 4.9 Synthesis of C-metalated aryl-Co(III) enolates bearing a variety of carboxylate anions (**5a-X**, where X = carboxylate anion, isolated yields).

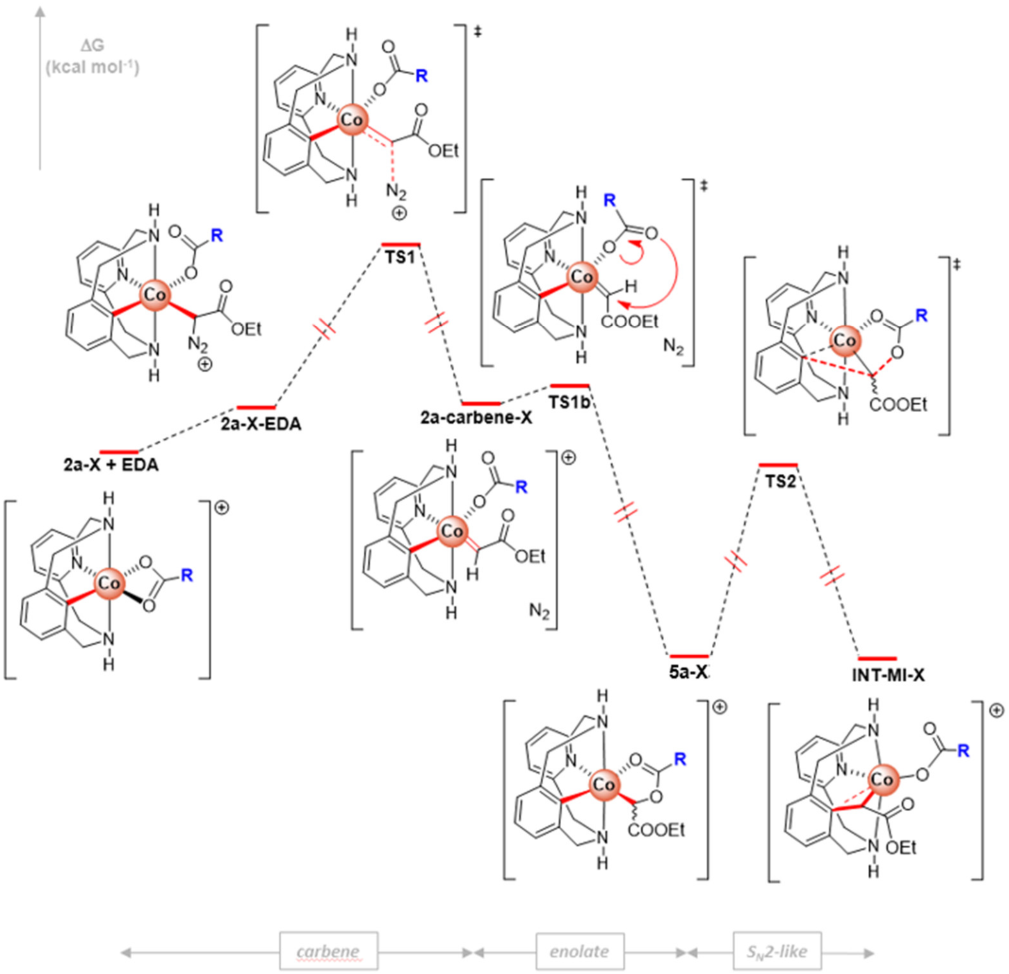

Figure 4.10 Energy profile sketch of the reaction for all the derivatives. The values of the relative Gibbs energies are given in **Table 4.3**

Table 4.3. Gibbs energy (ΔG in kcal/mol) of the reaction of **2a-X** with EDA species. Last row shows the activation barrier (ΔG‡) of the intramolecular S_N2-type C-C bond forming event.

X=	OAc	TFA[1]	OPiv	OBz (B)	B-Cl	B-OMe	B-NO$_2$	B-CN	B-Me	B-COMe
2a-X + EDA	0.0	0.0	0.0	0.00	0.0	0.0	0.0	0.0	0.0	0.0
2a-X-EDA	8.9	1.8	7.3	8.3	8.2	9.5	6.5	7.4	8.3	7.9
TS1-X	23.1	13.7	21.3	21.6	20.8	22.5	19.9	20.6	21.6	21.7
2a-carbene-X	9.8	—	10.0	11.2	—	—	—	9.2	10.7	10.3
TS1b-X	10.6	—	—	—	—	—	—	—	—	—
5a-X	**-30.3**	**-25.3**	**-32.0**	**-29.8**	**-30.0**	**-30.2**	**-29.3**	**-29.9**	**-30.9**	**-31.0**
TS2-X	-1.4	-5.6	-3.2	-1.4	-2.0	-1.1	-2.4	-2.0	-1.7	-1.44
INT-MI-X	-31.0	-35.2	-30.9	-31.0	-30.6	-29.2	-31.5	-31.2	-30.0	-29.93
ΔG‡ (TS2)	**28.9**	**19.7**	**28.8**	**28.4**	**28.0**	**29.1**	**26.9**	**27.9**	**29.2**	**29.6**

It is worth noticing that the fastest RDS of all the derivatives is the one for **2a-TFA**, the trifluoroacetate derivative, which is in agreement with the fact that it is the best leaving group. Therefore, **2a-TFA** is expected to have the lowest activation energy. Furthermore, the high relative Gibbs energy of the intermediate **5a-TFA** agrees with the fact that it was not possible to isolate it experimentally.

To gain further insight, we decided to plot the correlation between the calculated activation energies against the Hammett parameter values of the benzylic derivatives to study in a more appropriate manner the electronic effect on the reaction rate (**Figure 4.11**).

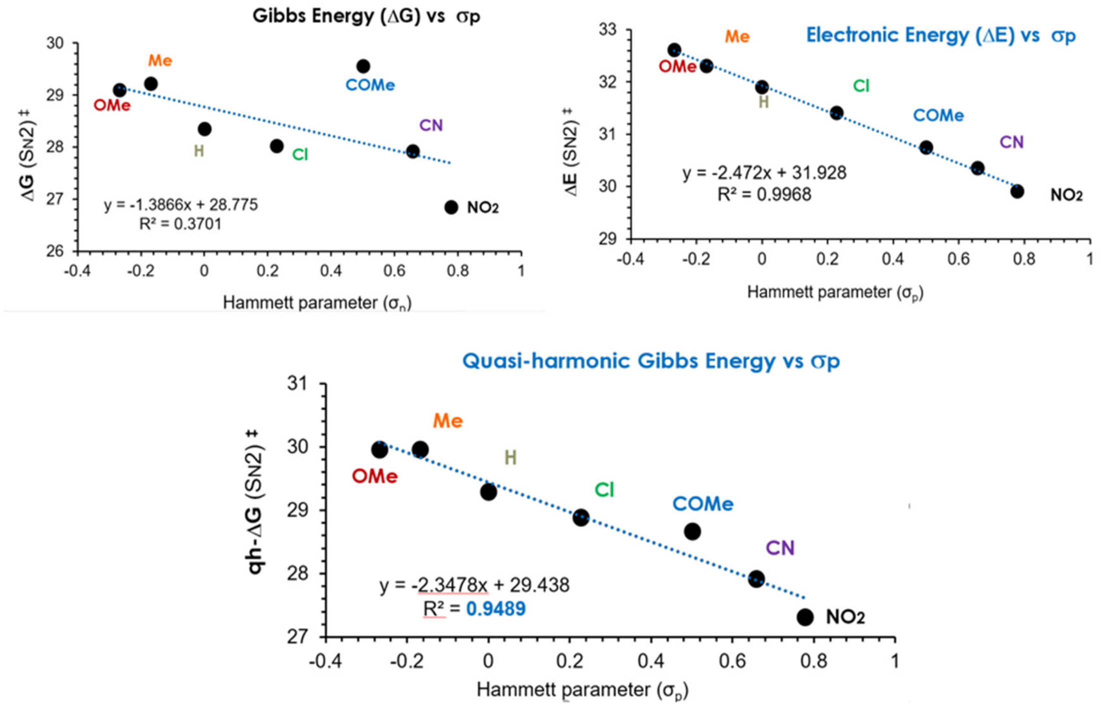

Figure 4.11 Hammett parameter plotted against **a)** Gibbs activation energy **b)** Electronic energy **c)** quasi-harmonic corrected Gibbs Energy values.

In the beginning, when we plotted the Gibbs activation barriers (ΔG‡), the correlation was very low (R2=0.37) but then, when we plotted the electronic energies (ΔE‡) of the **TS2-X** against the Hammett parameter, we obtained an excellent correlation (R2=0.99).

This likely indicates that the entropic corrections obtained from the frequency calculations using Gaussian 09, under standard conditions, were not the best ones. Therefore, we decided to recalculate the frequency calculations with a more rigorous model, the pseudo-harmonic model (see more in **chapter 2**, **section 2.3.6**, for more details). Once we obtained the recalculated values, the correlation between the corrected Gibbs activation barriers (qh-ΔG‡) versus the Hammett parameters was sufficient (R_2= 0.95).

In summary, **Figure 4.11** shows the relation between the energy required to overcome the rate-determining step (activation energy) and the Hammet parameters. The more electron-withdrawing the substituent on the carboxylate, the lower the activation barrier is.

4.3.3 Effect of the nucleophile's strength on the S$_N$2 type event.

After studying in depth the leaving group, the next logical step was to computationally study the effect of changing the electronic properties of the nucleophile in the S$_N$2 step. To achieve this goal, we calculated the Gibbs energy profile of the reaction for the species with a strong electron-donating group (OMe) and a strong electron-withdrawing substituent (NO_2) in the *para* position on the aryl-Co(III) complex (**Figure 4.12**). As we expected, augmenting the nucleophilic character of the C-metalated aryl-carbon with an electron-donating group decreases the activation barrier to form the C-C bond and increases the stability of **INT2b** (blue profile)**.** In the opposite direction, an electron-withdrawing group reduces the nucleophilicity of the aryl-carbon, increasing the activation barrier and decreasing the stability of **INT2c** (green profile).

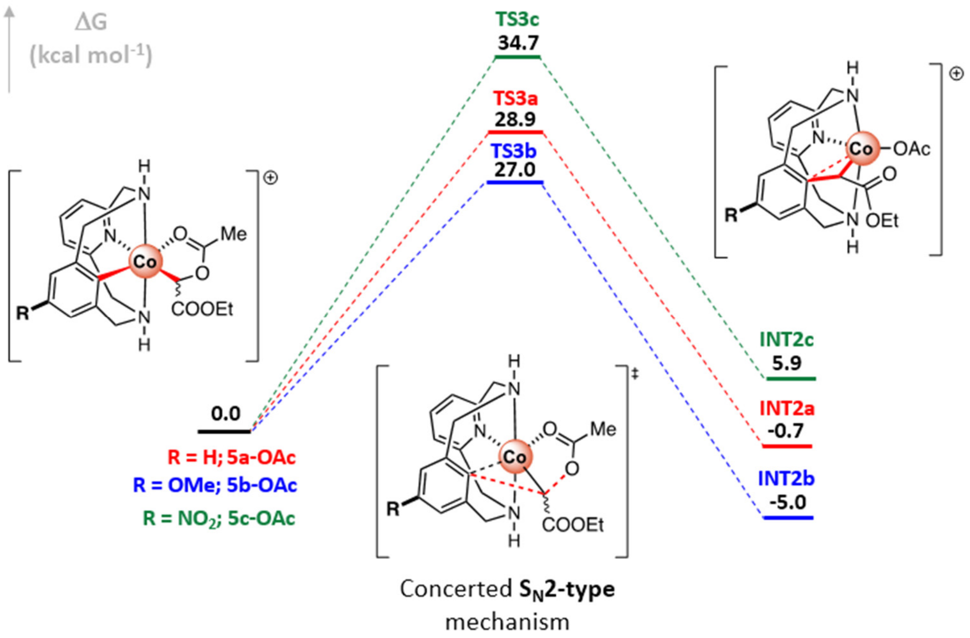

Figure 4.12 Gibbs energy profile of the S$_N$2-type event of *p*-substituted C-metalated aryl-Co(III) complex enolates **5x-OAc** (**R** = H (x=a), OMe (x=b) and NO_2 (x=c)). Relative Gibbs energy values are given in kcal/mol.

In addition, we were curious if a change in the character of the nucleophile would affect the initial part of the mechanism, therefore we calculated the whole mechanism for both derivatives (**Figure 4.13**). As we expected, the steps that did not involve the nucleophilic carbon were almost unaffected. The most noticeable difference is in the **TS3c** and **TS3b** and their respective products **INT2c** and **INT2b**. This indicates that in the rate-determining step (the S$_N$2-like event), the nucleophile plays a relevant role as important as the role of the leaving group. All this strongly supports the idea of a concerted S$_N$2-like transition state as the rate-determining step of the mechanism.

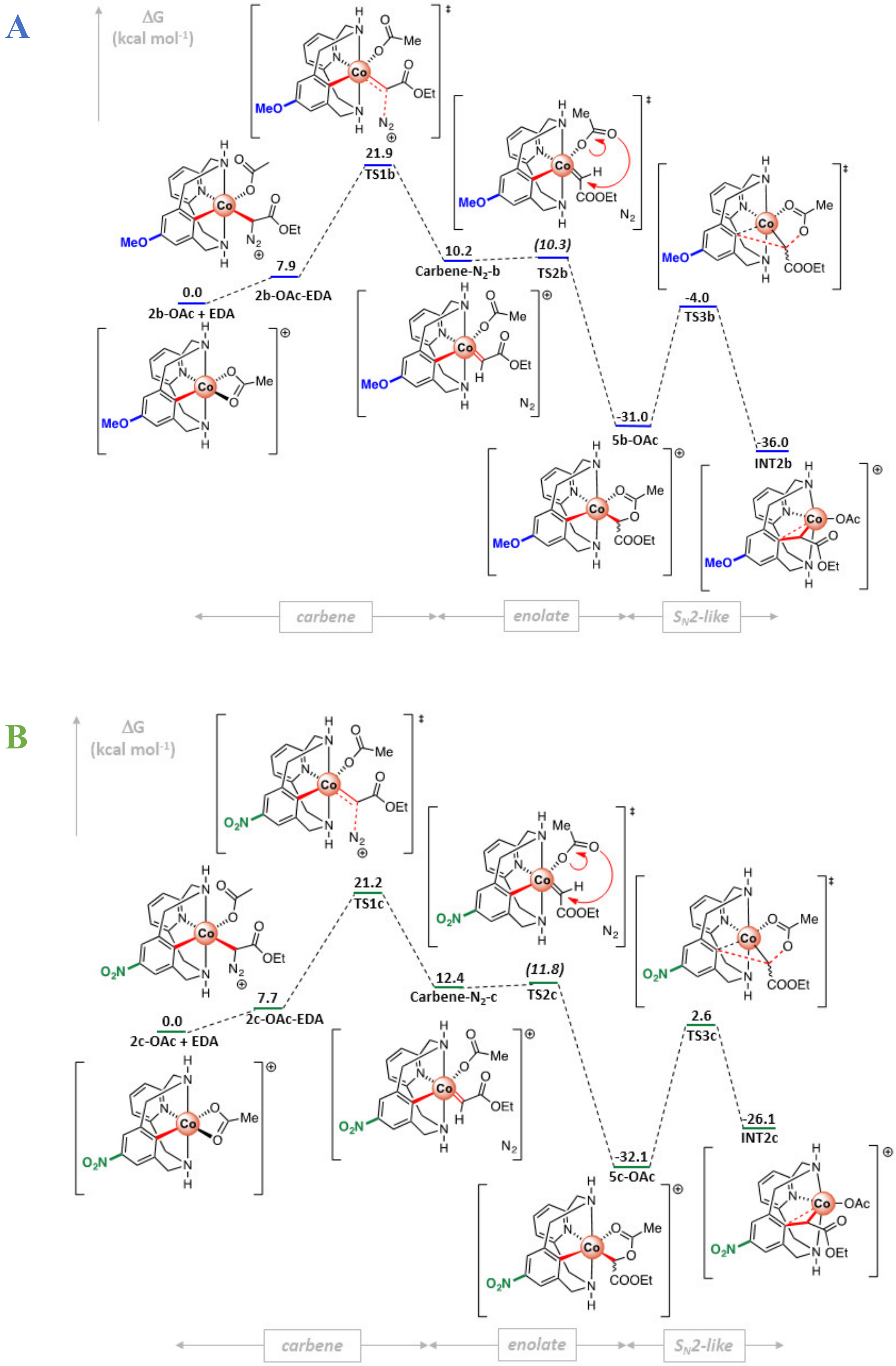

Figure 4.13 Gibbs energy profiles for **A)** the reaction of the electron rich *para*-substituted complex **2b-OAc** with EDA **B)** the reaction of the electron poor *para*-substituted complex **2c-OAc** with EDA

4.3.4 Effect of the α-substituted diazoacetates.

We explored another variable, the electronic character of the diazo ester by means of substituting it with an electron-withdrawing group in the *alpha* position. We only studied this variant computationally because the experimental evidence showed that the *alpha* electron-donating groups did not react (**Figure 4.14**). The figure also shows that in the case of the methyl or phenyl *alpha*-substitution, only some traces of the respective product **3** were found, which means that steric impedance is probably playing a role in the mechanism.

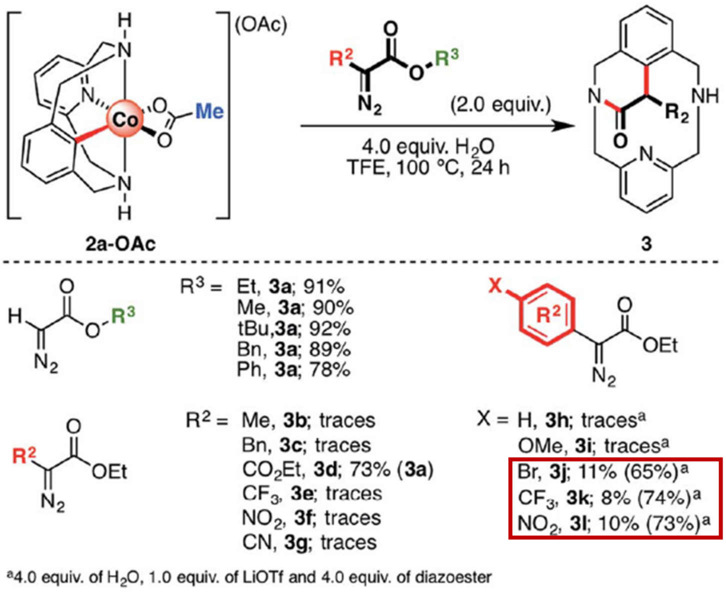

Figure 4.14 Reaction scope with several ester-substituted (R^3) and *α*-substituted (R^2) diazo-compounds. Yields were determined after isolation by silica column chromatography

Then, to explore the effect of the electron-withdrawing α-substituent on the diazo ester, we use the *α*-(*p*-substituted phenyl) diazoacetate (**EDA-$PhNO_2$**) as reactant with **2a-OAc**. **Figure 4.15** shows the Gibbs energy profile of the reaction. From this we can see that, as expected, the first transition state with **EDA-$PhNO_2$** is higher in energy (ΔΔG= 5.4 kcal/mol more) than the one with **EDA**. In accordance with the trend shown in the formation of the previous **4a** intermediate, the formation of **4a-OAc-$PhNO_2$** is very exergonic. Then, the S_N2-like event has a barrier of 35.9 kcal/mol to yield the endergonic intermediate **INT-MI-$PhNO_2$**. As we can see, the barrier of the previous step is high enough to require more drastic conditions. Moreover, the endergonic character of the product makes the formation of **3l** even more unlikely. This profile is in line with the fact that during the experiments (in anhydrous conditions) it was possible to detect the species **4a-OAc-$PhNO_2$** by HRMS. In addition, the intermediate **INT-MI-$PhNO_2$** was detected by HRMS when MS/MS analysis was applied with high collision energy (20eV), which agrees with the DFT result.

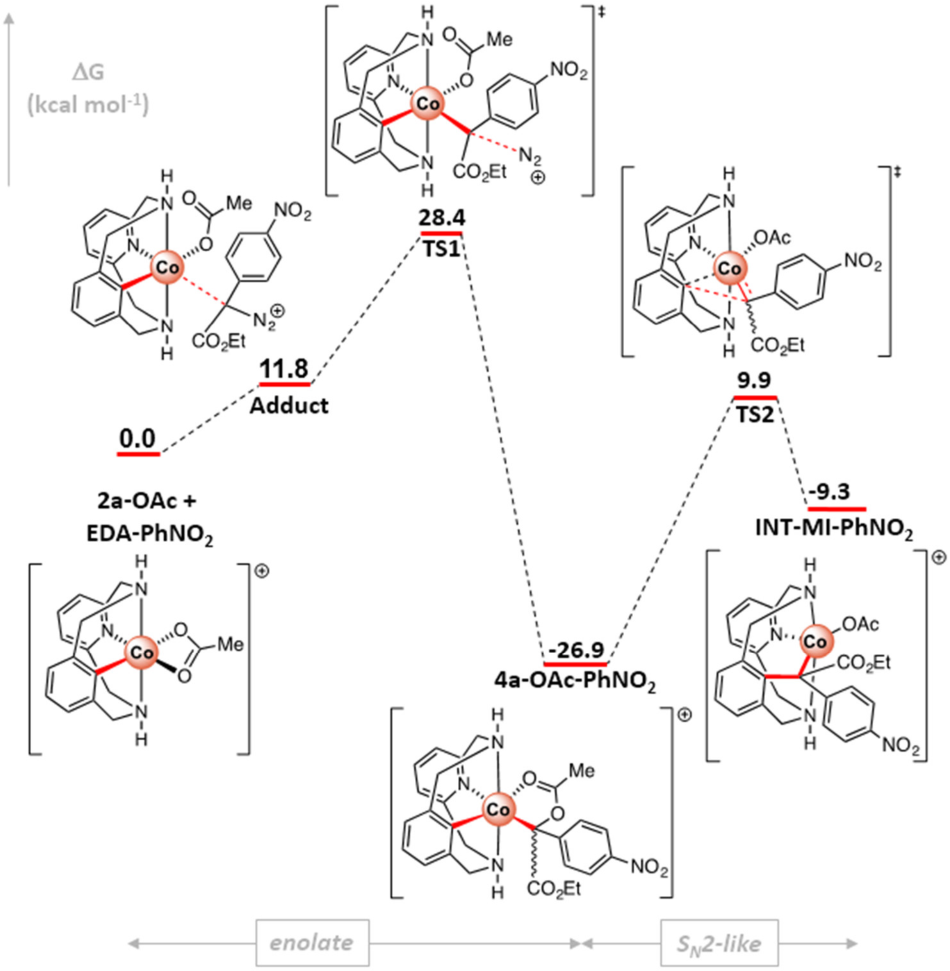

Figure 4.15 Gibbs energy profile of C-metalated aryl-Co(III) enolate formation and the S_N2-type event using **EDA-PhNO$_2$**. Relative Gibbs energy values are given in kcal mol/L

Interestingly, the transition state **TS2**, when using **EDA-PhNO$_2$**, exhibits an asynchronous behavior instead of the synchronous behavior that shows **TS3** when **EDA** is used (**Figure 4.16** shows the structure of both transition states). This is in agreement with the shape of the IRC plots of both transition states. The sharpness of the **TS3** peak concurs with the fact that both events occur at almost the same time. Instead, in the graph for **TS2** the plot looks like two fused peaks or a major peak with a shoulder. This type of behavior is typical of an asynchronous event, *i.e.*, the events are “almost” two events but close enough to be like one size-step event.

According to the results for structures **3j**, **3k** and **3l** (**Figure 4.14**), we obtained decent yields of the product when using **EDA-PhNO$_2$** because the reaction is performed with additives (H_2O and LiOTf). Therefore, we calculated the S_N2-like event in the presence of Li^+ acting as a Lewis acid (**Figure 4.17**). The figure clearly shows a **TS2-Li** barrier lower than **TS2** by 22.5 kcal/mol and it shows how the formation of the intermediate **INT-MI-PhNO$_2$** is now exergonic, which agrees with the fact that experimentally, in the presence of additives, the products are generated and the intermediates detected. It should be noted that the S$_N$2-like event occurs in an electrophilic tertiary carbon in an asynchronous manner, which is a very rare example of bimolecular substitution reaction.

As an additional remark, the steps that connect all the **INT-MI-X** with products **3** are very likely proto-demetalation steps, which in several cases were verified by deuterium labeling experiments. Therefore, we did not consider it necessary to study this step on the mechanism by computational means.

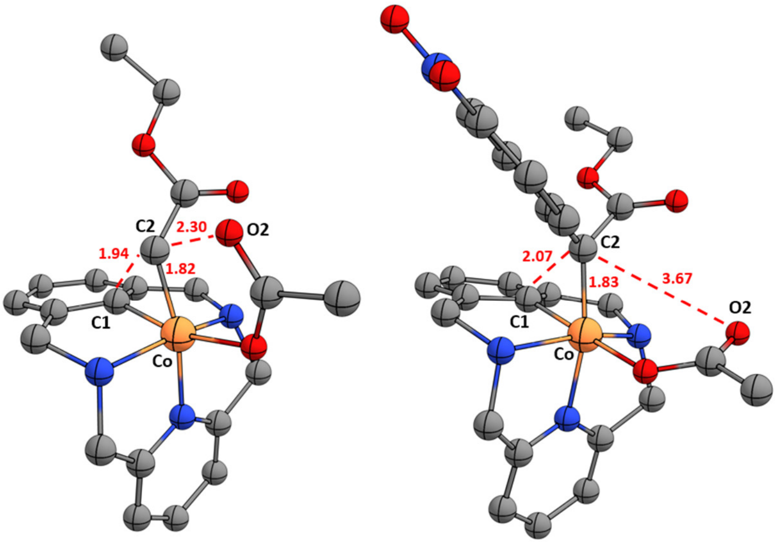

Concerted S$_N$2-type transition state (**TS2**)

Asynchronous S$_N$2-type transition state (***TS3***)

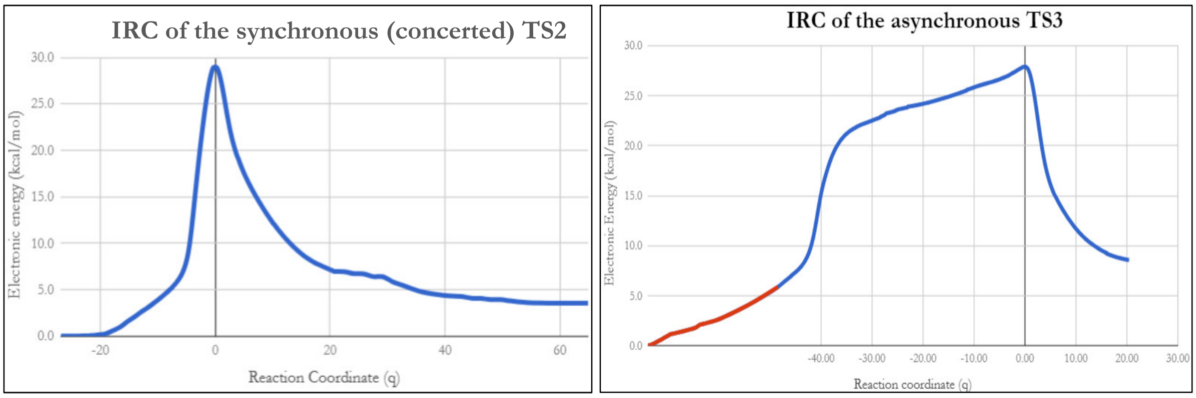

Figure 4.16 TOP: Computed transition state structures of the corresponding concerted S$_N$2-type C–C bond forming step with ethyl diazoacetate (left, synchronous) and **EDA-PhNO$_2$** (right, asynchronous). Selected bond distances are depicted in red. BOTTOM: IRC profiles for the concerted S$_N$2-type C-C bond forming step with ethyl diazo acetate (left, synchronous) and **EDA-PhNO$_2$** (right, highly asynchronous).

(a) Stabilization of TS2 and its intermediates with Li$^+$

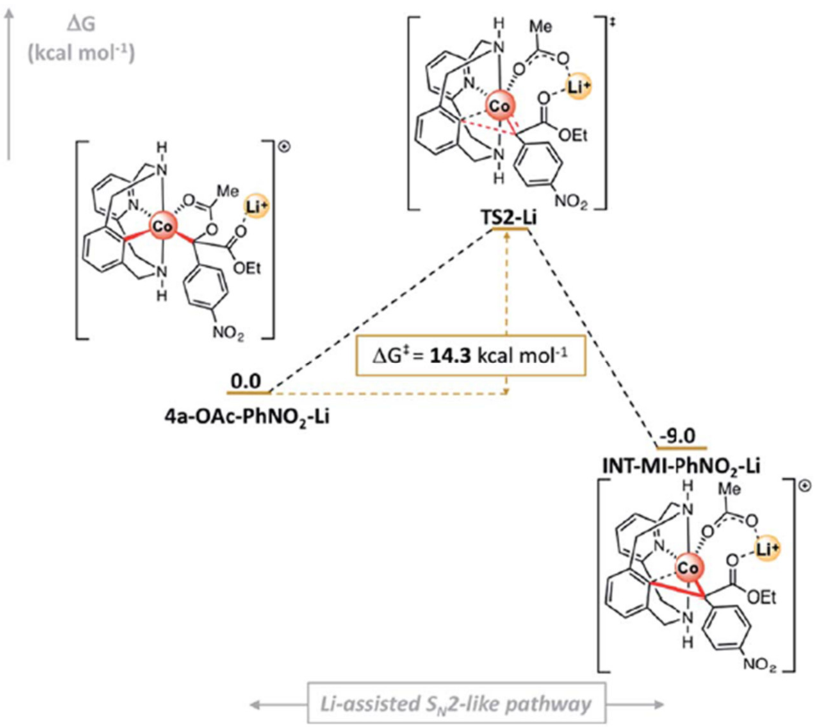

(b) Stabilization effect of Li$^+$ cation with 4a-OAc-PhNO$_2$

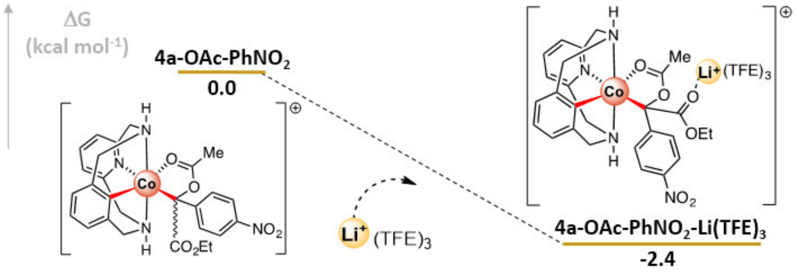

Figure 4.17 (a) Bonding energy of **4a-OAc-PhNO$_2$-Li-TFE$_3$**. **(b)** Gibbs energy profile of the S$_N$2-type event using **EDA-PhNO$_2$** in the presence of Li$^+$. Relative Gibbs energy values are given in kcal/mol

4.3.5 The effect of changing Cobalt by Rhodium.

During the exploratory phase of the reaction, we investigated a Rhodium-analogue of the reacting complex, using the same ligand template and similar experimental conditions (**Figure 4.18 (a)**). To our surprise, the reaction yielded the intermediate **6b-OAc**, which is quite interesting because it is not that common to find Rh(III)-alkyl species from carbenes.

Therefore, for the sake of curiosity, we calculated a plausible reaction mechanism for this analogous complex of Rhodium based on the one already studied for aryl-Co(III) species (**Figure 4.18** (b)).

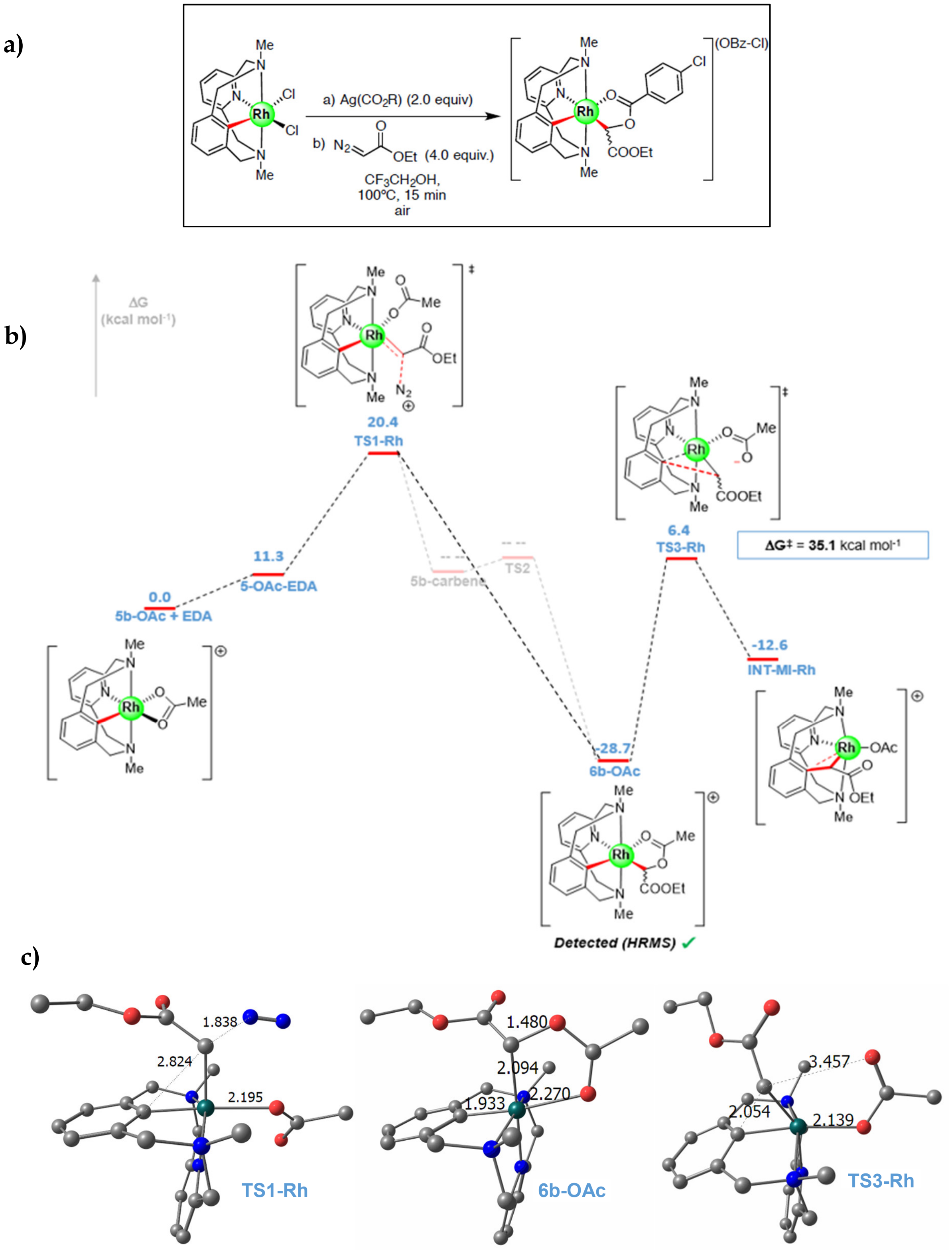

Figure 4.18 (a) Stoichiometric reaction of **6b-Cl** with EDA to furnish the intermediate species **7b-OBz-Cl** in presence of Ag(OBz-Cl). **(b)** Gibbs energy profile of C-metalated aryl-Rh(III) enolate formation and the S_N2-type event using **EDA**. Relative Gibbs energy values are given in kcal/mol. **(c)** Optimized structures of some of the species (Hydrogens omitted for clarity).

As expected, the Gibbs energy profile shows an accessible **TS1-Rh** that generates a very exergonic intermediate **6b-OAc**, followed by a highly energetic **TS3-Rh** (~ 35 kcal/mol) that yields an endergonic product **INT-MI-Rh**, which explains why we detect the intermediate **6b-OAc** but not the product.

It is worth mentioning that we did not find the **5b-carbene** and **TS2** corresponding structures, even though we tried.

In general, we have seen how the calculations performed to establish a mechanism of the reactivity of **EDA** (and derivatives) with **2a-OAc** (and derivatives or analogues) fit well with the experimental results. We were able to predict the structure of the intermediate (even before it was characterized by spectroscopy); we also explored in deep the parameters that controlled the masked-carbene's reactivity from a computational perspective. In addition, the DFT study gave us insight into the fascinating S_N2-like rate-determining step of the reaction and how the electronic character of the leaving group, the nucleophile, and the diazo ester can dramatically affect the reaction as well as the presence of Lewis acids. Moreover, the synergic understanding of the theoretical and the experimental evidences highlights the relevance of analyzing organometallic mechanism from both computational and experimental perspectives.

Chapter 5

Insight into the Trifluoromethylation Mechanism of a Well-Defined Aryl-Ni$^{(II)}$ Species via Putative Ni$^{(IV)}$ or Ni$^{(II)}$ Intermediates

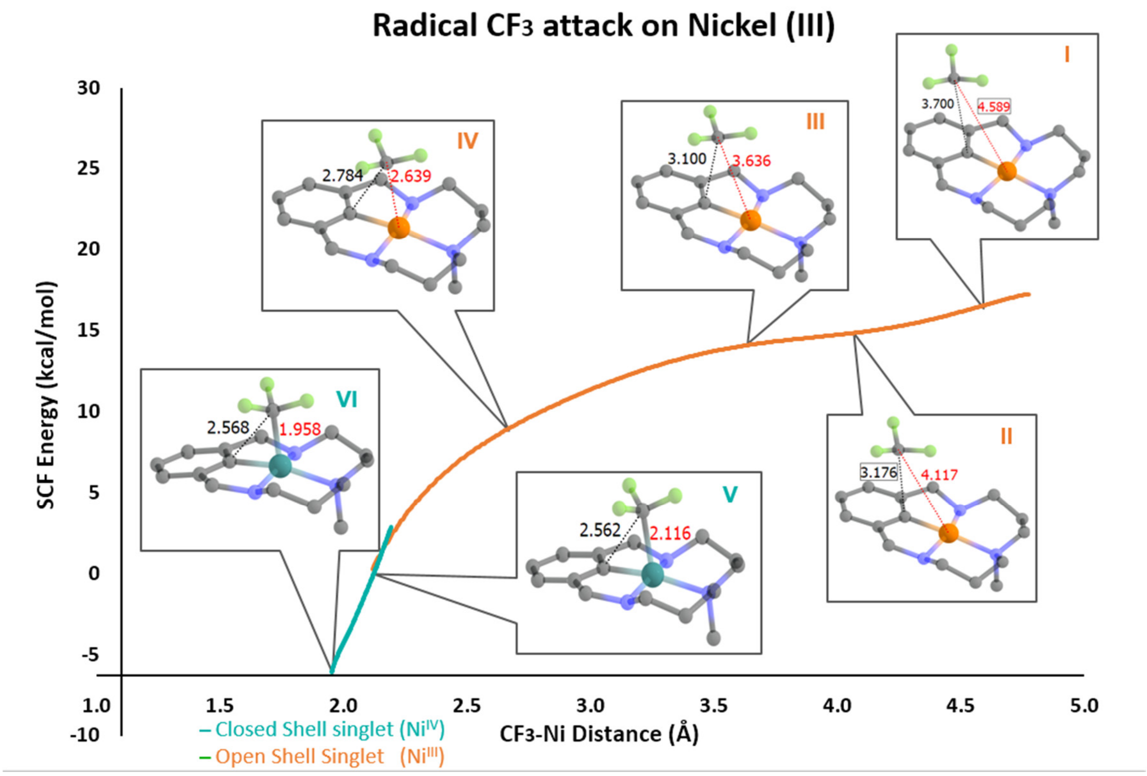

*This thesis chapter contains the calculations performed for the following publication:

Rovira, M.; Roldán-Gómez, S.; Martin-Diaconescu, V.; Whiteoak, C. J.; Company, A.; Luis, J. M.; Ribas, X. Trifluoromethylation of a Well-Defined Square-Planar Aryl-Ni II Complex Involving Ni^{III}/CF$_3$· and Ni^{IV}−CF$_3$ Intermediate Species. *Chem. – A Eur. J.* **2017**, *23* (48), 11662–11668. (doi:10.1002/chem.201702168)

Summary

In this chapter, we summarize the computational efforts to shed light onto the mechanism of the reaction between a mononuclear aryl-Ni^{II} complex with a trifluoromethyl source (Umemoto's reagent) to yield a trifluoromethylated aryl complex as a product. As a remarkable feature of this chapter, we found that the Ni center experiences several oxidation states (Ni^{II}/Ni^{III}/Ni^{IV}/Ni^{II}) during the reaction, caused by an initial single electron transfer, followed by a barrierless addition of the CF3 radical, and finally by a reductive elimination step. In addition, we computationally explored some derivatives of the template ligand and suggested which derivatives could be worth synthesizing based on their predicted properties.

5.1 State of the Art.

The trifluoromethyl moiety's ability to drastically change some physicochemical and pharmacological properties in several molecules has led to the development of a new diverse set of trifluoromethylation methodologies during the last decades[140–142]. Although most of the successful ones are palladium-based catalysis,[142–144] some interest has been directed toward the replacement with cheaper and more abundant catalytic sources like first-raw transition metals like Nickel or Copper.

It is commonly proposed for nickel-catalyzed C-C and C-X functionalization that the formation of Ni^{0}/Ni^{I}/Ni^{II}/Ni^{III} intermediates during their reactions[51,52,145–147] is usually a result of the $1e^-$ or $2e^-$ redox processes.[51,52,148–152] In recent years, the existence of Ni^{IV} intermediates in Ni^{II}/Ni^{IV} redox transformations has also been proposed.[153,154] Some of the Ni^{IV} intermediates have been well-characterized, but always using octahedral model substrates.[155–159] These kinds of studies have incited interest in trapping and exploring the reactivity of high-valent Nickel species.

Therefore, it is not strange to turn to the rich redox chemistry of Nickel to develop new trifluoromethylation methodologies, like the one developed by Sanford and co-workers which is based on a Ni^{IV} intermediate (see **Figure 5.1** (a)).[160] Consequently, it becomes paramount to properly comprehend the mechanistic features to gain predictability in the development of better Nickel-based reactions. Furthermore, it can be of general interest to gain insight into the behavior of high-valent Nickel, especially in atypical non-octahedral environments.

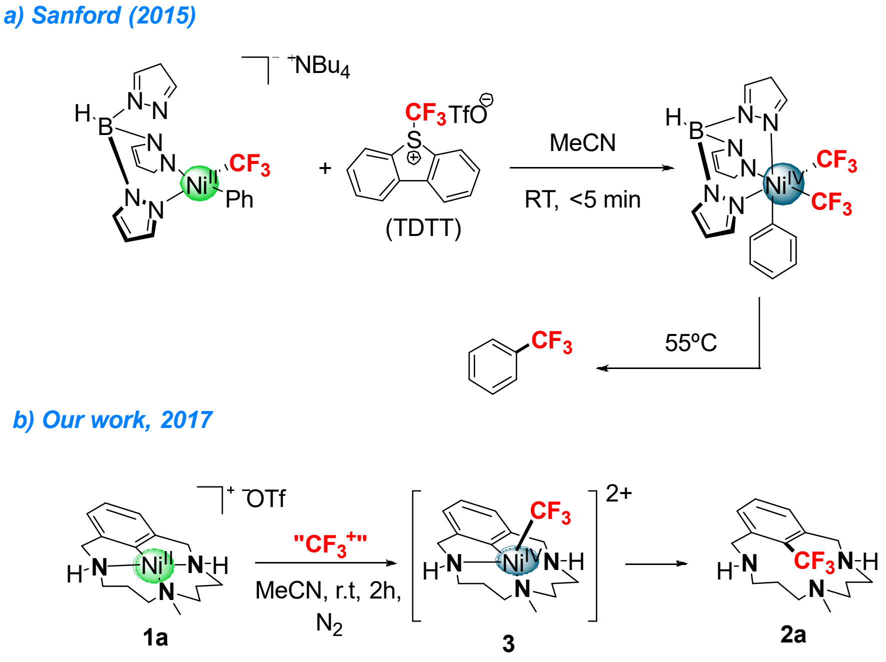

Figure 5.1 a) Ni^{IV} species reported by Sanford and co-workers and **b)** the system studied in his work.

With this in mind, we developed an organometallic square-planar aryl-Ni^{II} model system that enables the formation of Ni^{IV} species during the electrophilic trifluoromethylation of the aryl-Ni^{II} system (**Figure 5.1** (b)). Computational studies were carried out to comprehend the mechanism involved behind this reaction, exploring the plausible mechanistic routes it could be based on (both the 1e$^-$ and 2e$^-$ pathways).

5.2 Computational Details.

All calculations were performed with Gaussian 09 program.[99] Geometry optimizations were obtained using the Becke three-parameter functional with the Becke 88 exchange functional and the Lee, Yang, and Parr correlation functional (B3LYP)[79,81,138,139] along with the TZPV basis set developed by Ahlrichs.[161,162] The empirical dispersion was described using the D3 version of Grimme's model with Becke-Johnson damping algorithm (GD3BJ)[75] approach and the solvation effects in Acetonitrile were simulated using the PCM-SMD method developed by Truhlar *et al.*[94] Subsequent frequency calculations at the same level of theory were performed to evaluate enthalpy and entropy corrections at 298.15 K (Gcorr.) and to ensure that all local minima had only real frequencies while a single imaginary frequency confirmed the presence of transition states. All transition states were connected to the corresponding reactants and products with IRC calculations. Finally, single point energy calculations were done with a more flexible basis set, cc-pVTZ,[163,164] including the solvent effects and GD3BJ dispersion corrections (Ecc-pVTZ). The Gibbs energy variation of 1.89 kcal/mol due to the change of conventional 1 atm standard state for gas-phase calculations to a standard-state gas-phase concentration of 1.0 M (except for acetonitrile which is considered at its liquid concentration) was also included, $\Delta G^{o/*}$. Then, the final total Gibbs free energy (G) was given by:

$$G = E_{cc\text{-}pVTZ} + G_{corr.} + \Delta G^{o/*} \quad \text{(Equation S1)}$$

It is worth adding that all the calculations (especially the ones involving radicals) were performed with broken-symmetry DFT. Moreover, we used Gaussian's keywords *guess=(mix)* and *guess=(mix,always)* to destroy the $\alpha-\beta$ and spatial symmetries in the guess orbitals of the SCF procedure during the optimizations.

5.3 Results and Discussions.

We developed, in our group, organometallic aryl-Ni^{II} complexes **1-Me** and **1-H**, which were isolated and structurally characterized by X-ray spectroscopy and other techniques (see **Figure 5.2**).[165] Some features worth highlighting about these complexes are that they were quite stable (did not show any reactivity) in presence of certain nucleophiles (phenols, boronic acids, and activated methylene compounds, amongst others). The specific experimental conditions in which the reaction were carried out are described in **Figure 5.3**, which depicts the reaction of the complex **1-H** with the trifluoromethylating agent 5-(trifluoromethyl)dibenzothiophenium triflate (TDTT) in acetonitrile, at room temperature and under Nitrogen atmosphere for only four hours to yield a 99 % of the trifluoromethylated product (**4-H**).

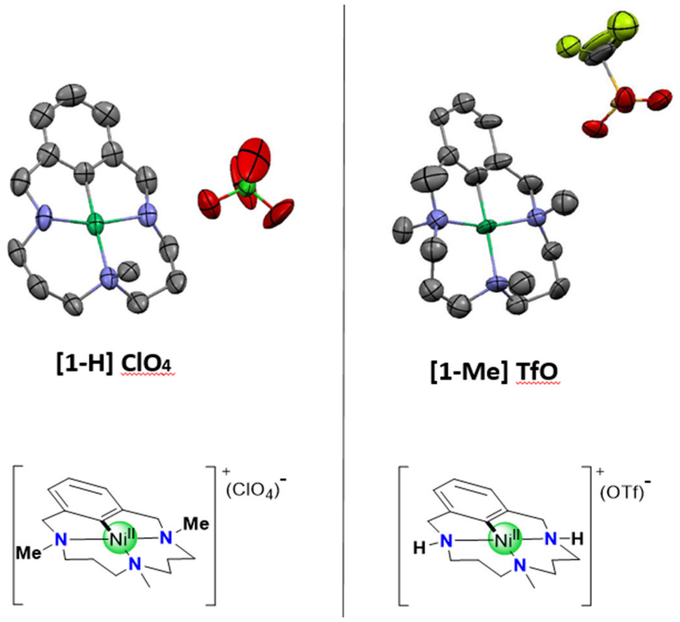

Figure 5.2 X-ray crystal structure of both complexes, **1-H** and **1-Me**. H atoms omitted for clarity.

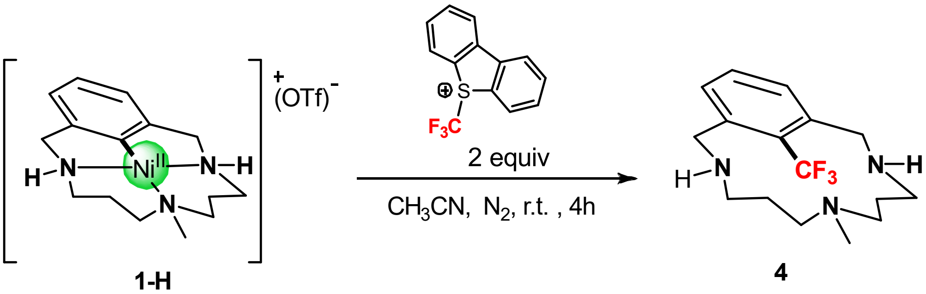

Figure 5.3 Experimental conditions of the trifluoromethylation reaction.

Taking into account that both the $1e^-$ and $2e^-$ oxidation processes are possible, we considered three plausible alternative mechanisms for the reaction (A, B, C), described in **Figure 5.4**. In hypothetical mechanism **A**, the first step is a $2e^-$ oxidative addition-like reaction of the CF_3 source, TDT^+ (counterions omitted for clarity), to the metal complex to yield the intermediate **3,** followed by a reductive elimination that generates the new C-CF_3 bond in the product (**4**). In the case of mechanism **B**, it proceeds via a single electron transfer (SET) from the metal to the TDT^+ to generate a Ni^{III} complex (**6**) and a CF_3 radical, followed by a rapid addition of the latter to the aryl moiety of the complex (**6**) (the one with the C-Ni^{III} bond). The last option, mechanism **C**, is a combination of mechanisms **A** and **B**. The first step of mechanism **C** involves the formation of the Ni^{III} and the CF_3 radical. However, in this third suggested pathway, the CF_3 radical reacts with the Nickel instead of the aryl carbon (like in mechanism **B**) to yield the intermediate Ni^{IV} complex, which will finally undergo reductive elimination to yield the product and Ni^{II}.

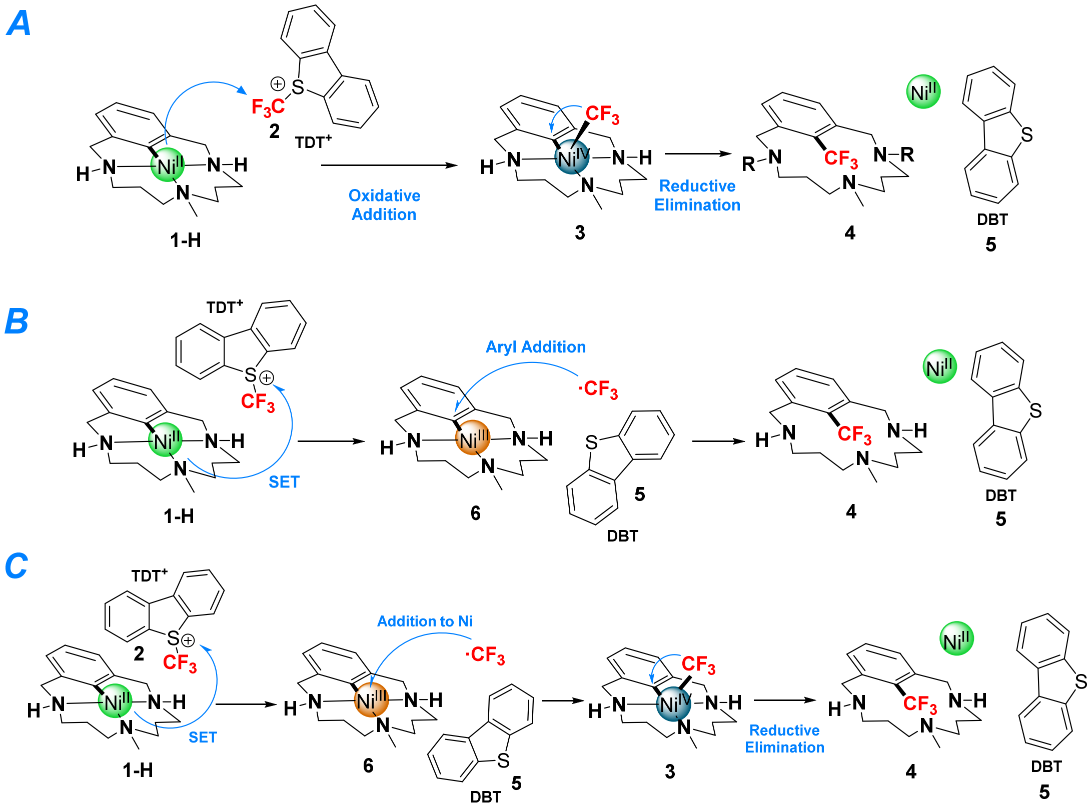

Figure 5.4 The three proposed mechanisms, **A**, **B**, and **C**. Mechanism **A** implies the transfer or flow of two electrons (2e⁻) during the reaction (oxidative-addition-like step followed by a reductive-elimination step); **B** can be described as single electron transfer (SET) followed by a direct radical CF_3 addition in the aryl group; **C** contains the first step of **B** and the last step of **A**, and so it can be considered a combination of **A** and **B**.

5.3.1 Mechanism **A**.

We took as initial structure of the Ni^{II}-aryl complex the coordinates of a similar structure as a template (the N-methylated Ni^{II}-aryl complex), which was obtained by X-ray diffraction. From this template, we calculated the different thermodynamic species that correspond to mechanism A. Then, we calculated the oxidative addition that yields the Ni^{IV} complex (**3**). For this step we computed two plausible transition states, TS_1 and $TS_{1\text{-alt}}$, which correspond respectively to an S_N2-like attack and a side-fashion attack to the CF_3. In **Figure 5.5**, we can see that the Gibbs energy of TS_1 is almost 10 kcal/mol lower than the one of $TS_{1\text{-alt}}$. Even so, both values are high enough to not allow the reaction to proceed at the given conditions (25 °C). Moreover, there is almost no thermodynamic gain in energy when transforming **1-H** into **3**, which already suggests that this step is not favorable.

However, we explored the next step of the reaction, the reductive elimination, assuming that the complex **3** was formed. As **Figure 5.5** shows, the barrier for the transformation of **3** (singlet) into **4** (singlet or triplet) is quite small, just 7.1 kcal/mol. Furthermore, the formation of **4** is clearly exergonic by -28.7 kcal/mol and -35.3 kcal/mol for both the singlet and triplet states, respectively.

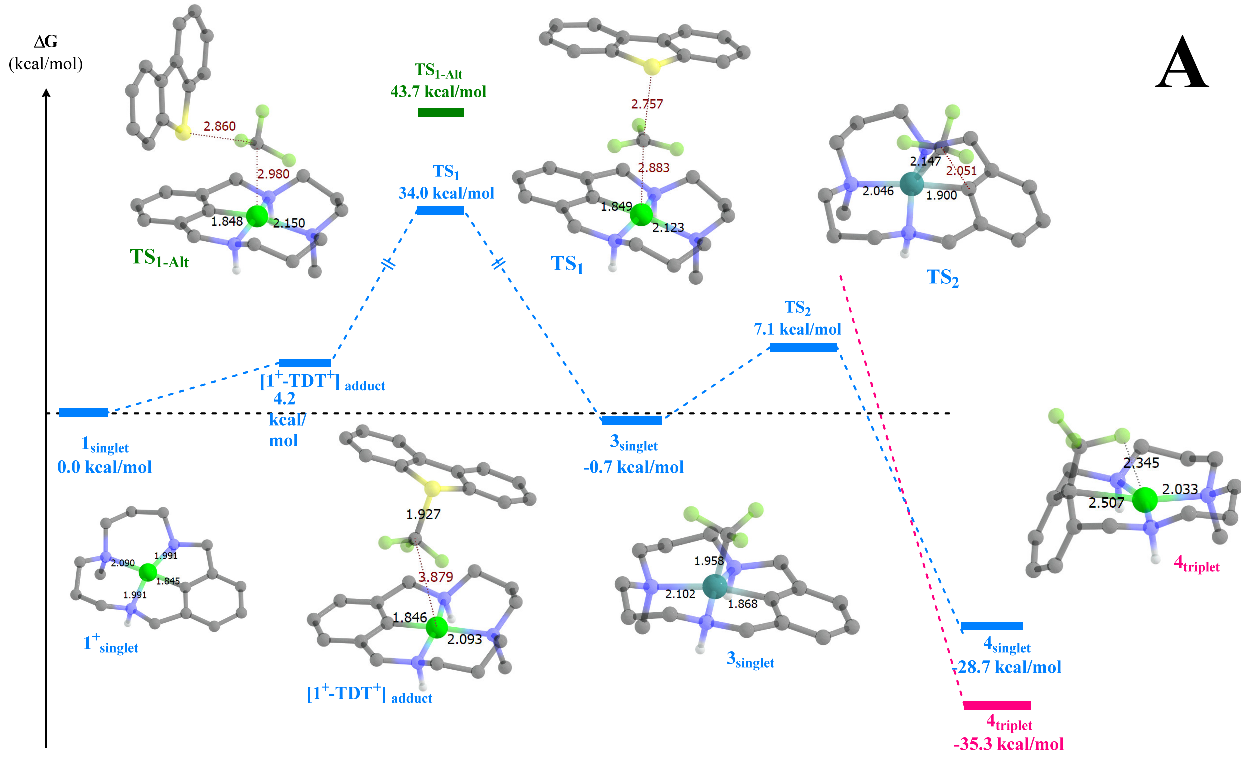

Figure 5.5 Free energy profile for the proposed mechanism **A** computed at B3LYP-GD3BJ/cc-pVTZ//B3LYP-GD3BJ/TZPV level. TS$_1$ and TS$_{1\text{-Alt}}$ correspond to the two plausible transition states that connect the Ni^{II} and Ni^{IV} species through an oxidative addition-like step. The former represents an S$_N$2-like attack between the species, while the latter describes a lateral-type attack. TS$_2$ is the transition state of the reductive elimination step of pathway A. Blue lines represent the singlet state pathway, whereas magenta ones describe the triplet profile. Atomic color code: Carbon, Nitrogen, Fluorine, Sulphur; In the case of Nickel, different colors are assigned to different oxidation states: Nickel (II), Nickel (IV).

The second step of the reaction is kinetically and thermodynamically favorable. However, the first step, the oxidative addition, is kinetically unfavorable at standard conditions. This led us to explore other versions or alternatives of the oxidative addition. We tried to include explicit counter ions to complete the octahedral coordination sphere with a molecule of solvent (acetonitrile) and calculations at higher temperatures, but none of these approaches yielded more favorable Gibbs energy values for the oxidative addition. Therefore, we discarded mechanism **A** as the mechanism for our reaction because the high barrier didn't match with the mild experimental conditions.

5.3.2 Mechanism **B**

In the case of mechanism **B**, the first step of the reaction occurs via single electron transfer (SET) to yield a radical Ni^{III} intermediate (**6**) and a radical CF_3 moiety. The energy barrier related to a single electron transfer was calculated with the Marcus approximation (procedure described in chapter 2) and it is only 18 kcal/mol, feasible for the system at the given conditions (shown in **Figure 5.6**). From these results, it is clear that the first step of the reaction prefers the $1e^-$ pathway to the $2e^-$ one. Then, once we have the Nickel(III) intermediate species, we try to find a transition state to connect $\mathbf{6_{radical}}$ intermediate with product **4**. Unexpectedly, we were not able to find a direct addition over the aryl-Carbon. Instead, our calculations were always yielding the intermediate **3**; in other words, the CF_3 radical was axially coordinating to the Ni^{III} center in lieu of the aryl-C center. From this fact, we devised the plausible mechanism **C**.

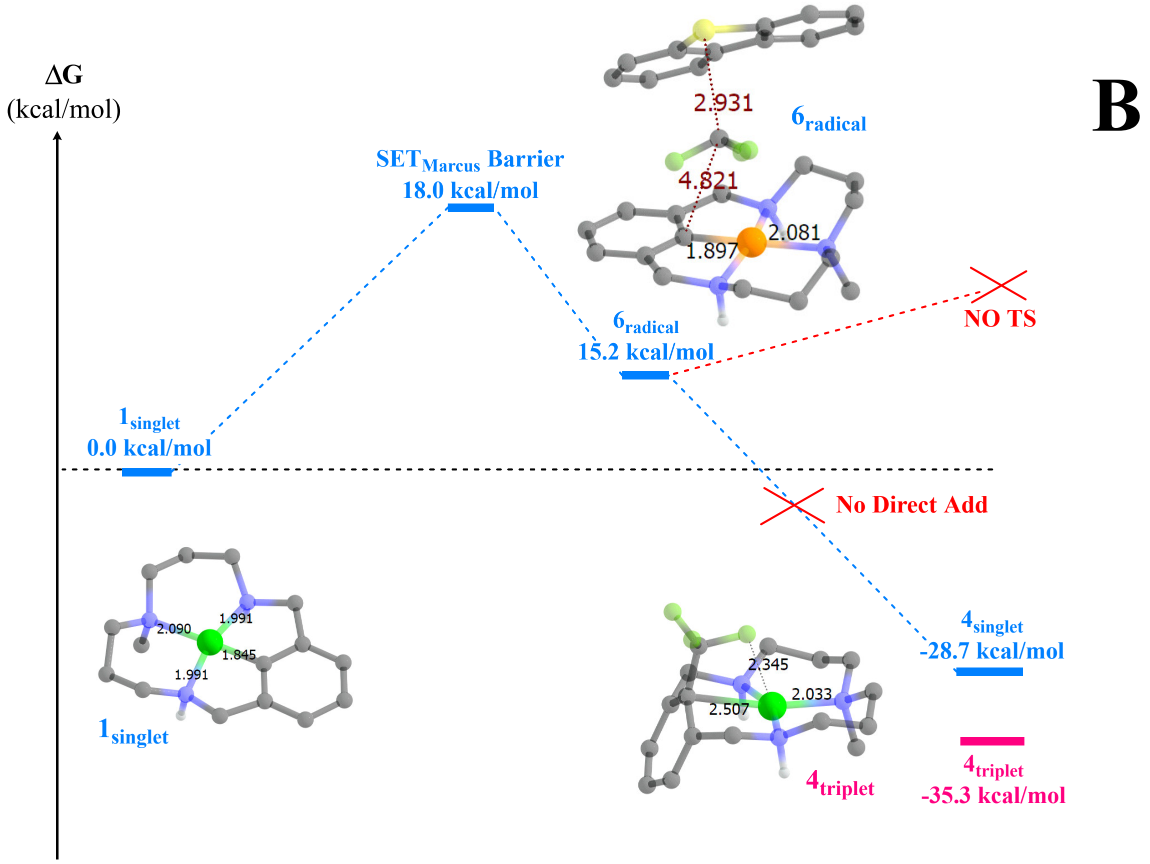

Figure 5.6 Gibbs energy profile for the proposed mechanism **B** computed at B3LYP-GD3BJ/cc-pVTZ//B3LYP-GD3BJ/TZPV level. The SET energy barrier ($\mathrm{SET_{Marcus}}$ Barrier) defines the first step of the reaction. No TS for the direct addition of the radical to the aryl carbon was found. Blue lines represent the singlet state pathway, whereas magenta ones describe the triplet state species. Atomic color code: Carbon, Nitrogen, Fluorine, Sulphur; In the case of Nickel, different colors are assigned to different oxidation states: Nickel (II), Nickel (III).

5.3.3 Mechanism **C**

As we mentioned before, mechanism **C** is a combination of mechanism **A** and mechanism **B**, in which the first part corresponds to the first step in **B** (a single electron transfer that yields Ni^{III} and CF_3 radical) and the second part corresponds to the final step in **A** (a reductive elimination from Ni^{IV} to Ni^{II} complex). In both cases, the Gibbs energy barriers were low enough to occur at the given conditions (18 kcal/mol for the SET and 7 kcal/mol for the reductive elimination). However, the step that connects mechanisms **A** and **B** was still missing, in other words, the connection between intermediate $\mathbf{6_{radical}}$ (the CF_3 radical with the Ni^{III} complex) and $\mathbf{3_{singlet}}$ (Ni^{IV} complex with the CF_3 added over the Ni center).

Based on our findings in mechanism **B**, we hypothesized that once the CF_3 radical is formed, the addition of the fluorinated moiety over the Ni^{III} (or the aryl-C) atom is barrierless. Therefore, to corroborate our hypothesis we followed the approach of the trifluoromethyl radical to the Nickel complex by IRC. In fact, the IRC path (**Figure 5.7**) showed no barrier during the process. In order to perform a more exhaustive exploration of the PES, we tried several initial points (some close to the C-aryl atom) and even in those cases the addition of the CF_3 radical to the Nickel was always barrierless.

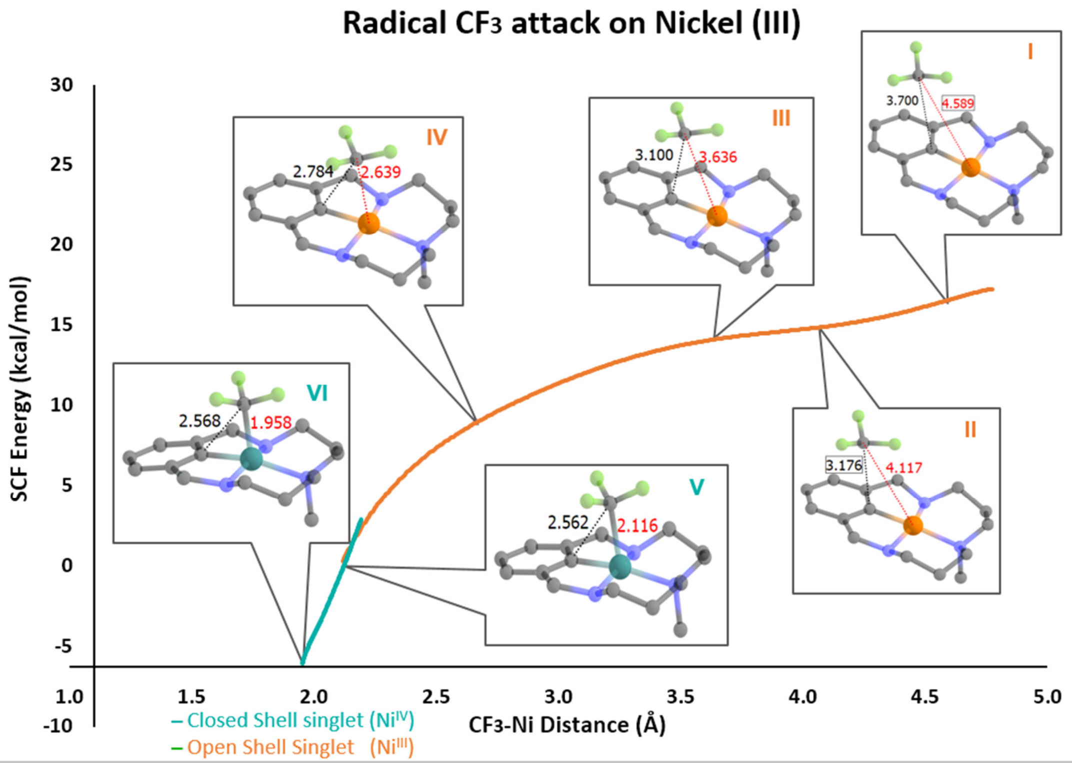

Figure 5.7 Energy profile computed at the B3LYP-GD3BJ/TZPV level and geometries of snapshots of the $CF_3\cdot$ attack of the Ni^{III} to generate Ni^{IV}. The plot shows the electronic energy profile of the barrierless approach of the radical to the Ni^{III}. Atomic color code: Nickel (III), Nickel (IV).

It is worth mentioning that we explored the PES of the system (CF_3 addition to Nickel, which is composed of two doublets) in triplet, open-shell singlet, and closed-shell singlet. Out of these three, the lowest in energy was the open-shell singlet for Ni-CF_3 distances larger than 2.2 Å; for shorter distances, the closed-shell singlet is the most stable. **Figure 5.7** illustrates the IRC path of this process (we used IRC calculation with persistent broken-symmetry to ensure that we were following the open-shell singlet until the Ni-CF_3 bond is formed). **Figure 5.8** shows the spin density of two selected points during the CF_3 radical addition (4.41 Å and 3.19 Å CF_3-Ni distances). From here we can see that the spin density is located where we expected, in the Carbon atom of the CF3 moiety and the Ni center of the complex, which is in agreement with the fact that the attack occurs on the Nickel and not on other parts of the complex.

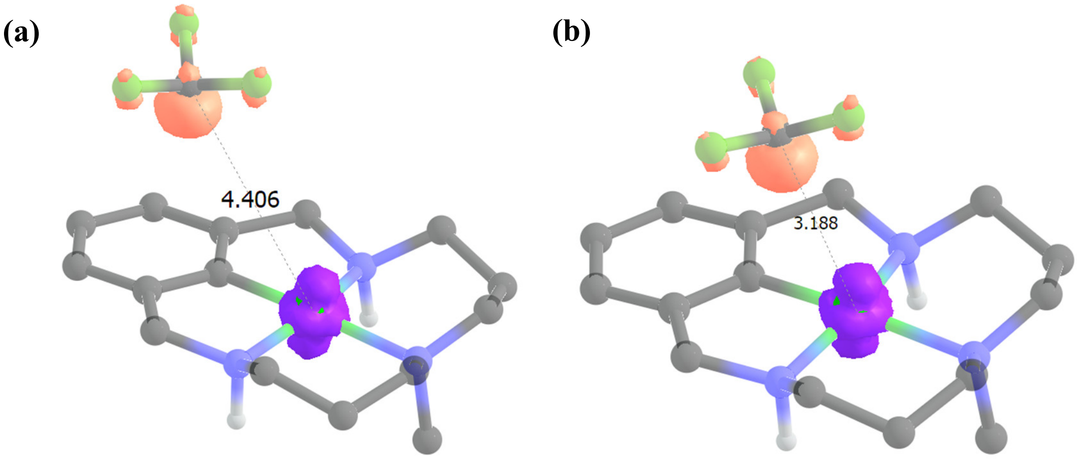

Figure 5.8 Computed spin density map that shows the two unpaired electrons (open-shell singlet) for two points of the IRC calculation of the CF_3 attack on the Ni^{III} complex. **(a)** CF_3-Ni distance = 4.406 **(b)** CF_3-Ni distance = 3.188. Contour value: 0.040

At this point, having understood the connection between mechanisms **A** and **B**, we can depict the Gibbs energy profile of mechanism **C** (**Figure 5.9**). As we can see, the rate-determining step is the SET. Once the CF_3 radical is generated, the reaction proceeds with almost no energetic cost (the 7 kcal/mol barrier of the reductive elimination is smaller than the SET barrier), therefore, the reaction is expected to be fast. Indeed, the largest barrier of mechanism **C** (*i.e.* 18 kcal/mol) fits with the experimental evidence.

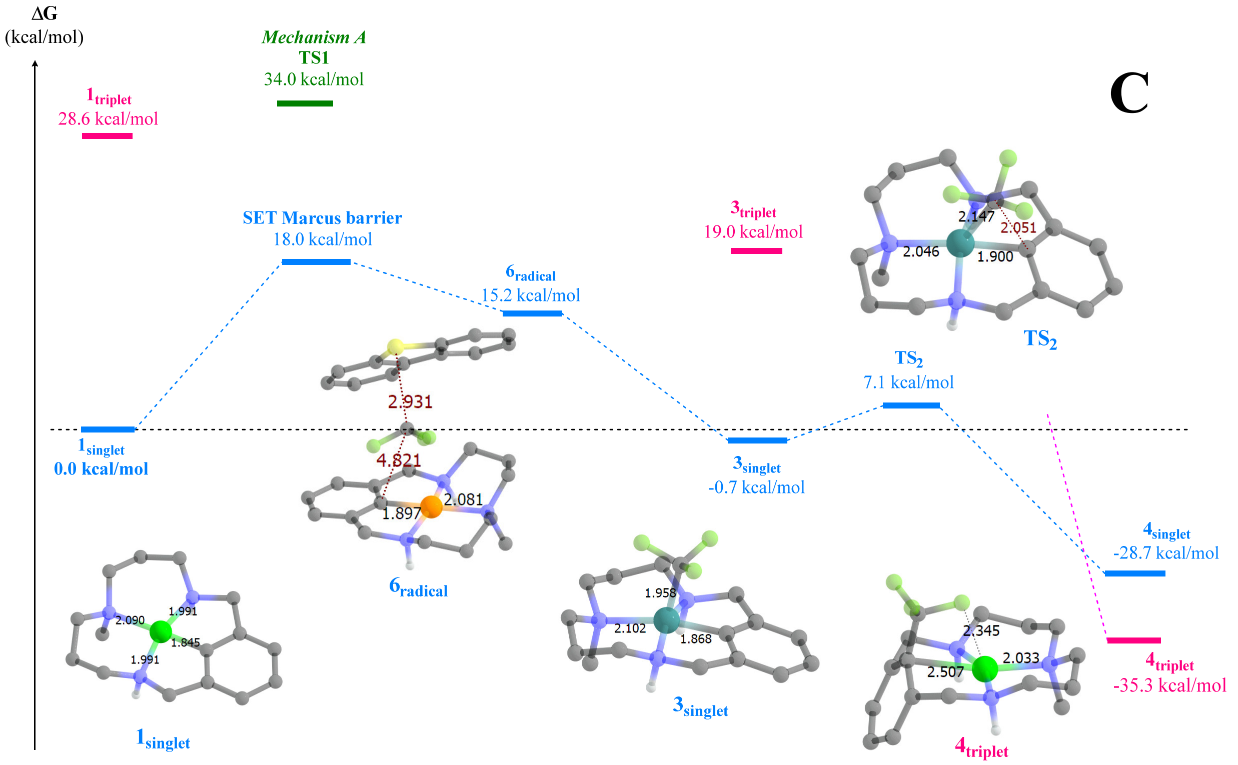

Figure 5.9 Gibbs energy profile for mechanism **C**. Free-energy values were calculated at the B3LYP-GD3BJ/cc-pVTZ//B3LYP-GD3BJ/TZPV level. The blue profiles correspond to the most stable open- or closed-shell singlet states, whereas the magenta lines represent the triplet states. The Gibbs energy of the rate-determining transition state of mechanism **A** (TS_1) is depicted to compare it with the value of the single-electron-transfer Marcus barrier. The zero Gibbs energy values of the profile correspond to the free energies of reactants at infinite distance. Atomic color code: Carbon, Nitrogen, Fluorine, Sulphur, Nickel (II), Nickel (III), Nickel (IV).

5.3.4 Exploration of Nickel-complex **1** derivatives.

Since we were able to find a mechanism that properly explains the kinetics of the reaction, using DFT calculations, we wanted to investigate further. Therefore, we tried to understand and predict the reactivity of several derivatives of our Nickel complex **1** based on the mechanism that we found. In this way, we may find an interesting candidate worth synthesizing experimentally in the near future.

Therefore, we decided to computationally explore several *para*-aryl (and some *meta-aryl*) derivatives of **1** (**Figure 5.10**).

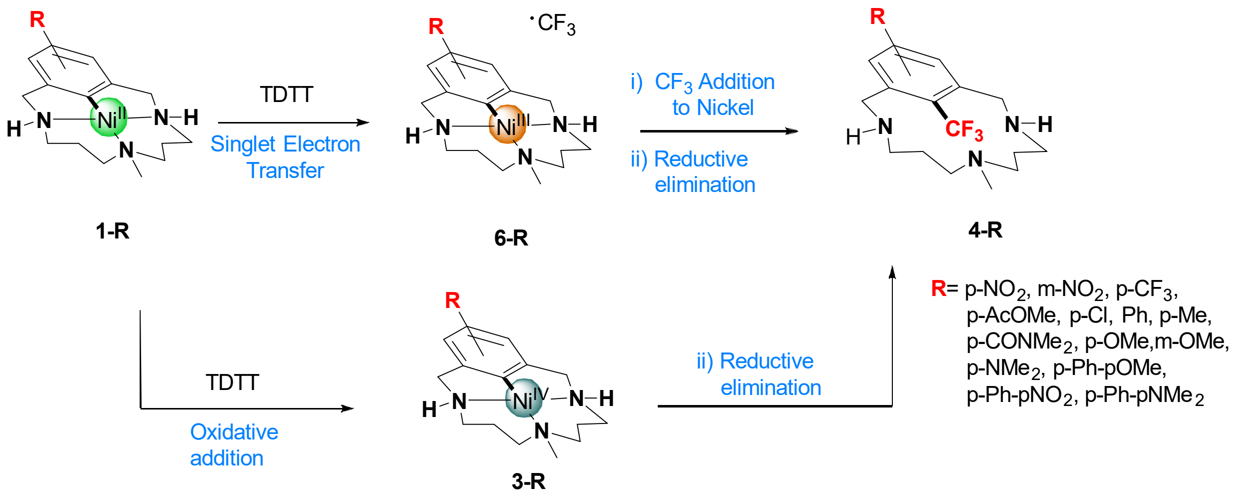

Figure 5.10 One electron and two electron mechanistic routes to transform **1-R** into **4-R** for any of the derivatives described.

Since the radical mechanism is the one that we found most favorable, we thought that knowing the thermodynamic energy of the Nickel(III) complexes (**6-R**, the product of SET) could give us some insight regarding the reactivity of the Nickel derivatives. Moreover, the Ni^{III} complex intermediates are far easier and faster to calculate than the Marcus barrier for all the species. In **Figure 5.11**, the energy of all the Nickel(III) complex derivatives (**6-R**) is depicted.

The first result that we notice is the trend that the red points clearly show, that is, the more electron-withdrawing the substituent, the higher the Gibbs energy difference of the Ni^{III} complex (with respect to the Ni^{II} complex). This behavior is coherent, since the more electron-withdrawing the group, the harder it will be to take an electron from the Nickel because the effect of the EWG on the aryl also affects the Nickel through the aryl-C-Nickel bond.

On the contrary, strong electron-donating groups do not have a strong effect in the energy difference between Ni^{III} and Ni^{II} complexes, and they show very similar values to the reference energy difference (the blue dashed line, **R=H**). This could be attributed to the similar gain in stabilization that both Ni^{II} and Ni^{III} complexes suffer. In the case of the orange points, which correspond to an extra *p*-substituted-aryl substituent, we can observe the same pattern caused by the electron-withdrawing/donating effect of the substituents but with a more subtle effect than their counterparts without the extra phenyl ring. It is very likely that this is due to the fact that the electron attractor (or donor) groups are further away from the Nickel and, therefore, their influence is smaller.

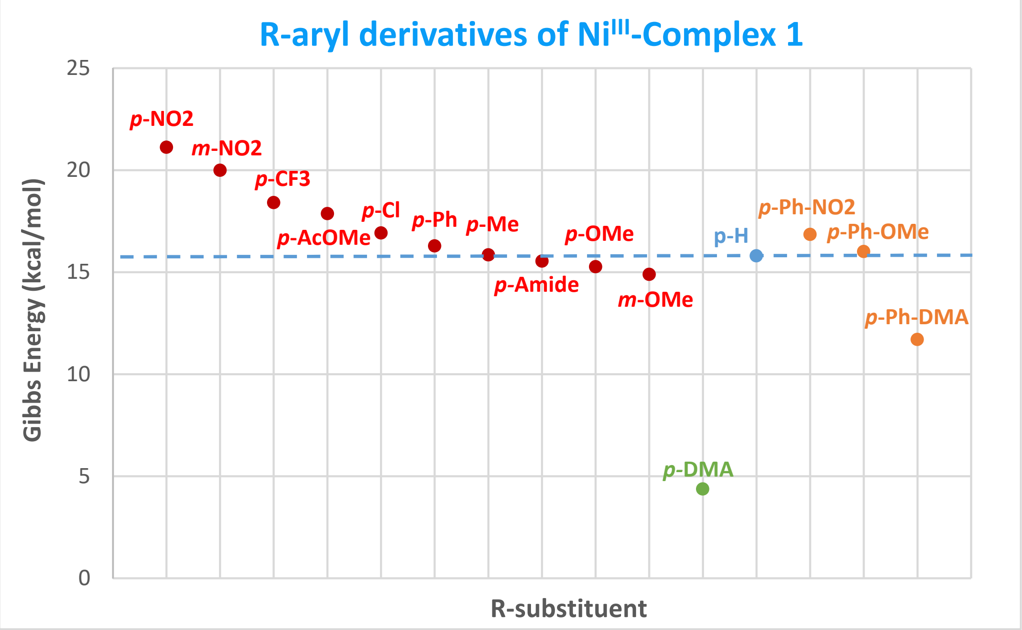

Figure 5.11 Gibbs Energy difference of the Ni^{III} complexes (**6-R**) with their respective Ni^{II}-complexes (**1-R**). The Gibbs energy difference of **6** corresponds to the **blue** dashed line (**R=H**). The **red** points correspond to molecules with different types of electron-withdrawing and electron-donating groups in *para* and *meta* positions to the aryl-Ni^{III} complex. In **orange**, we depicted the Gibbs energy difference of the radicals that insert an extra *p*-substituted phenyl ring in the *p*-aryl position of the Nickel complex. In **green**, we show the energy difference of the *p*-*N*Me$_2$-aryl-Ni^{III} complex, which suffers an abrupt stabilization in comparison with the others.

In the case of the *para*-dimethylamine substituent, (*p*-DMA), the point in green in **Figure 5.11**, there is a strong stabilizing effect. The Gibbs energy difference of the *p*-DMA substituted Ni^{III} complex (with respect to the Ni^{II} complex) is around 10 kcal/mol lower than the Gibbs energy difference of the non-substituted complex (**R=H**). This behavior does not follow the pattern, which make it interesting to study further.

Then, we calculated the Marcus barrier for the formation of the Ni^{III} complex for the substituents R= *p*-DMA, *p*-OMe, and *p*-NO$_2$ (with the last two used as a references of derivatives that followed the pattern). We also calculated the transition states **TS$_1$-R** to determine whether the substituents favored the 2e$^-$ path (mechanism **A**). These results are described in **Figure 5.12**. As expected, we observed that the SET barriers follow a similar pattern to the one in **Figure 5.11**: i) the electron-withdrawing group has a strong destabilizing effect; ii) the electron-donor one slightly affects the barrier; and iii) the *p*-DMA substituent highly stabilizes the barrier, diverging from the pattern. The same tendency is observed in the **TS$_1$-R** transition states; however, the SET barriers are always lower in energy than **TS$_1$-R**.

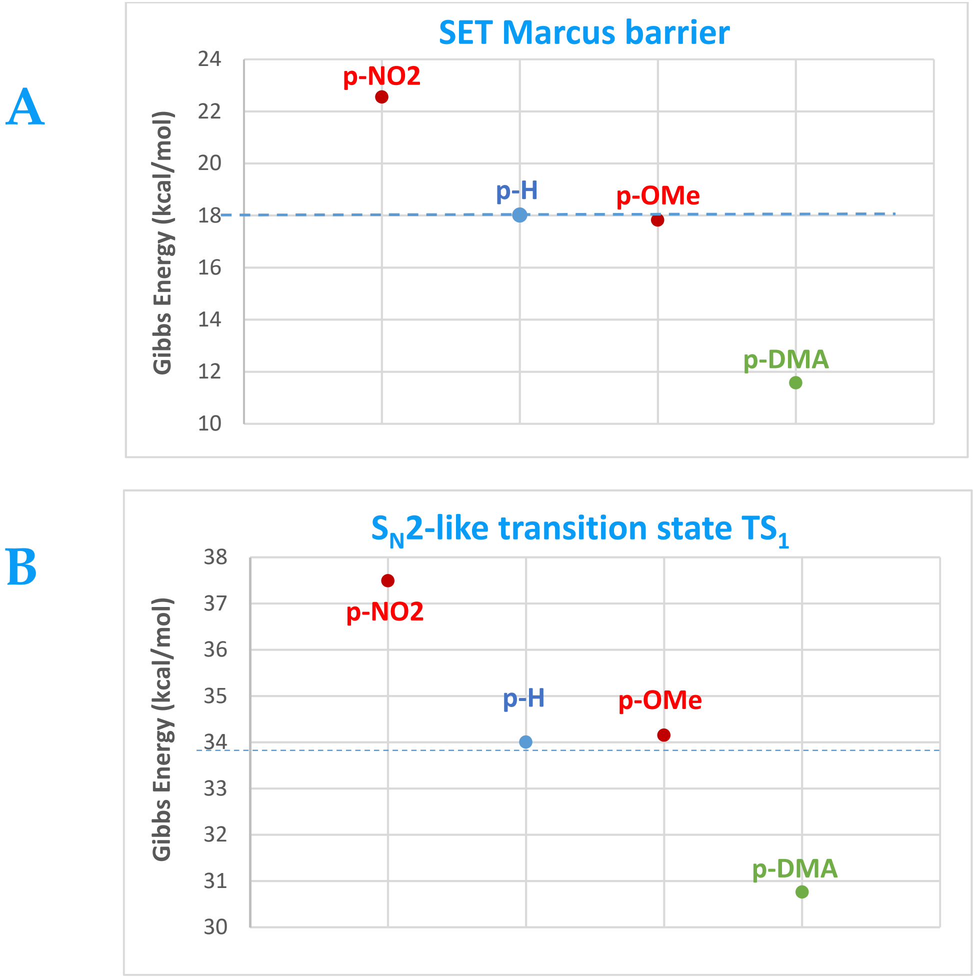

Figure 5.12 A) Single electron transfer Marcus barrier of the formation of the Nickel(III) complex via mechanism **C** for the derivatives R= *p*-NO_2, *p*-OMe, *p*-DMA, *p*-H. **B)** S_N2-like transition state **TS_1** of the formation of Nickel(IV) via mechanism **A** for the derivatives R= *p*-NO_2, *p*-OMe, *p*-DMA, *p*-H.

The fact that the *p*-DMA-aryl-Ni^{III} complex, the *p*-DMA SET barrier, and *p*-DMA-TS_1 were so low in energy compared to the other derivatives led us to think that the *p*-DMA substituent could induce the formation of a non-innocent ligand. To verify this, we explored the total spin density of the *p*-DMA, *p*-NO2, *p*-OMe and *p*-H Ni^{III} complexes (**Figure 5.13**). As the figure shows, the spin density of these Ni^{III} complexes is located in the metal center except for the *p*-DMA substituted complex, in which the spin density is distributed through the ligand, especially over the Nitrogen atom of the dimethylamine moiety, verifying that the ligand is non-innocent.

Additionally, we explored the LUMO (since we are using broken-symmetry, with LUMO we refer to the "unoccupied β-SOMO" in radical species) of the four selected derivatives with the intention of rationalizing their reactivity with the CF_3 radical (**Figure 5.14**). In the case of the *p*-H, *p*-NO_2, and *p*-OMe substituted ligands, the LUMO is localized on the Nickel, which indicates that if the Ni^{III} complex reacts with the CF_3 radical, the trifluoromethyl moiety will attack the Nickel center. Instead, with the *p*-NMe_2 substituted ligand, the LUMO is delocalized over the aromatic moiety, the dimethylamine group, and slightly over the metal. The highest contribution is localized on the Nitrogen of the dimethylamine group and the aromatic Carbon bonded to the Nickel. This shape of the LUMO led us to think that the CF_3 radical will react with the amine moiety or the aryl carbon one in lieu of reacting directly with the Nickel center.

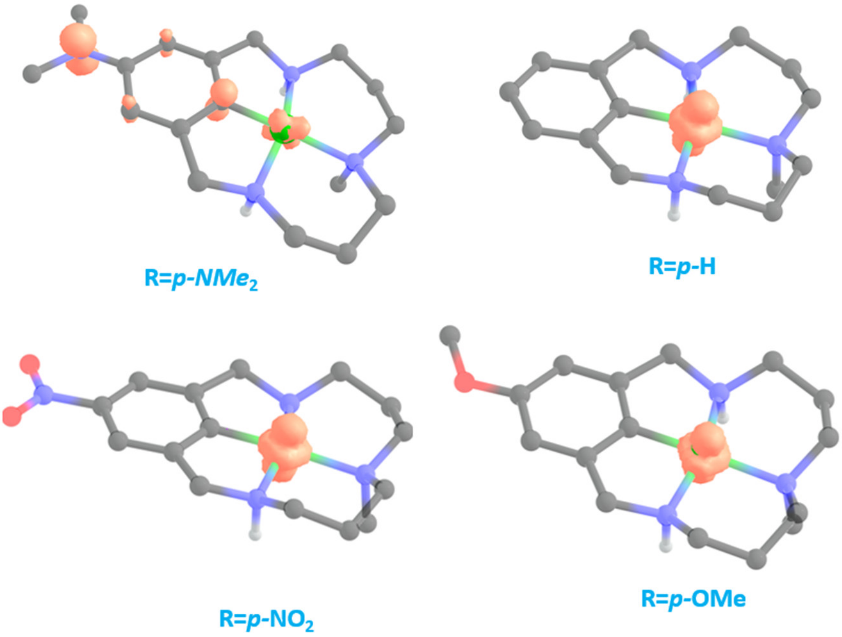

Figure 5.13 Computed total spin density map that shows the localization of the unpaired electron of the four derivative (R-) Ni^{III}-complexes. Contour value: 0.016.

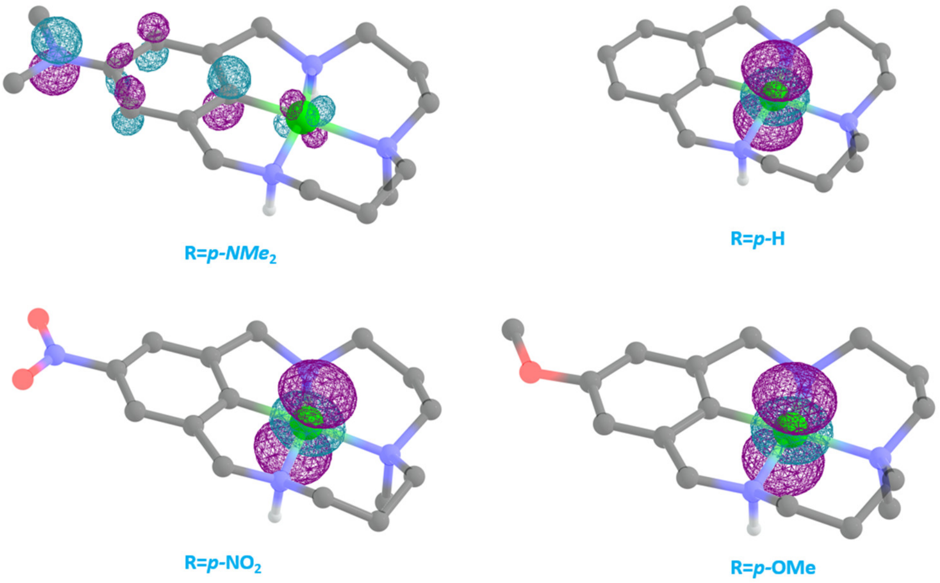

Figure 5.14 LUMO (“unoccupied β-SOMO” in radical species in broken-symmetry context) distribution for the R-derivatives of the Ni^{III} complex. Contour value: 0,075.

In summary, our predictions suggest that the most interesting complex to synthesize would be the *p*-NMe_2-substituted Ni^{III}-complex. However, we are fully aware that the selectivity of the reaction could be affected (according to its spin distribution) by the presence of other possible sites for the radical attack of the CF_3. Nevertheless, we think that it would be interesting as an initial step in the exploration to find better catalysts for this reaction.

5.3.5 Reactivity of the Palladium analogue Complex **1-Pd**

Taking advantage of the acquired knowledge about the reaction with Nickel, we thought that it could be interesting to explore computationally the same reaction with a late transition metal of nickel's group (group 10), like Palladium, just for the sake of knowledge. Nevertheless, we were fully aware that Palladium chemistry is prompt to only perform $2e^-$ reactions and that the few times that Pd(III) has been reported it has been in bimetallic or dimeric complexes.[19,142]

Specifically, we wanted to investigate if the trifluoromethylation of a similar aryl-palladium (II) complex could occur via the proposed mechanism **A**, **B** or **C**, provided that the experimental reaction works and that it does not lead to unexpected side products.

In **Figure 5.15**, we have depicted the analogous intermediates of the mechanisms **A** and **C**, some of the triplet spin states of the species and the rate-determining step barrier for the two mechanisms **A** and **B** (the **TS_1-Pd** and **SET_{Pd}-barrier**). As it can be seen, a SET step to Pd^{III} is more favorable that the oxidative addition to Pd^{IV}, thus in the case that the reaction actually happens experimentally, a SET pathway will be the preferred mechanism for the trifluoromethylation reaction, although higher temperatures than a Ni-based reaction will be necessary.

In summary, we studied three types of mechanisms to describe the behavior of the trifluoromethylation of a Ni^{II} complex, from which we realized that the most favorable one is mechanism **C** (a single electron transfer, followed by a CF_3 radical attack over the Nickel center and a reductive elimination as the final step). Then we explored the mechanism of some derivatives of complex **1**, from which we found the complex **1-*p*-NMe_2** especially interesting due to its non-innocent ligand effect on the complex. Finally, for mere scientific curiosity we explored the mechanism of a Palladium analogue of complex **1.**

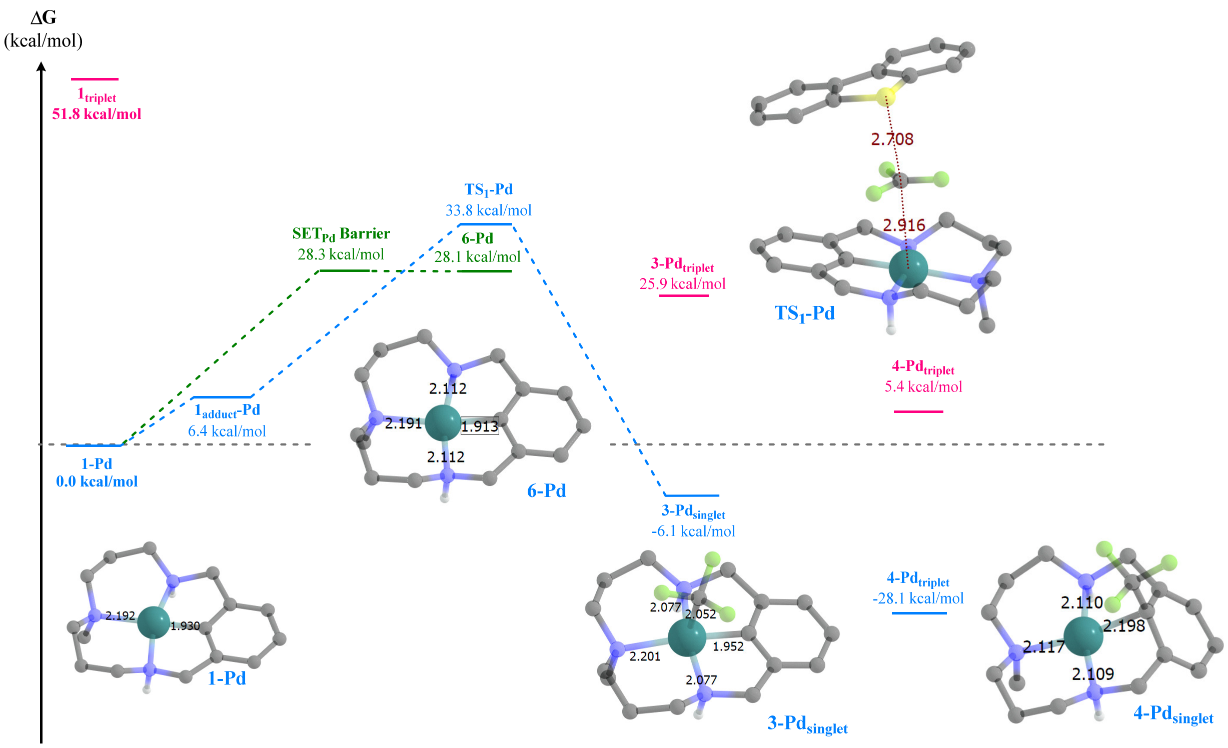

Figure 5.15 Gibbs Energy profile for the analogous aryl-Pd^{II} complex with a trifluoromethyl source (TDTT). The blue lines correspond to the species related to mechanism **A**, the green ones with the first step of mechanism **C**. The magenta lines represent the triplet spin state of some species. Color code: Carbon, Nitrogen, Fluorine, Sulphur Palladium.

Chapter 6

Nickel-Catalyzed Aromatic Homologation by Alkyne Insertion versus Alkyne Mono-annulation by Reductive Elimination

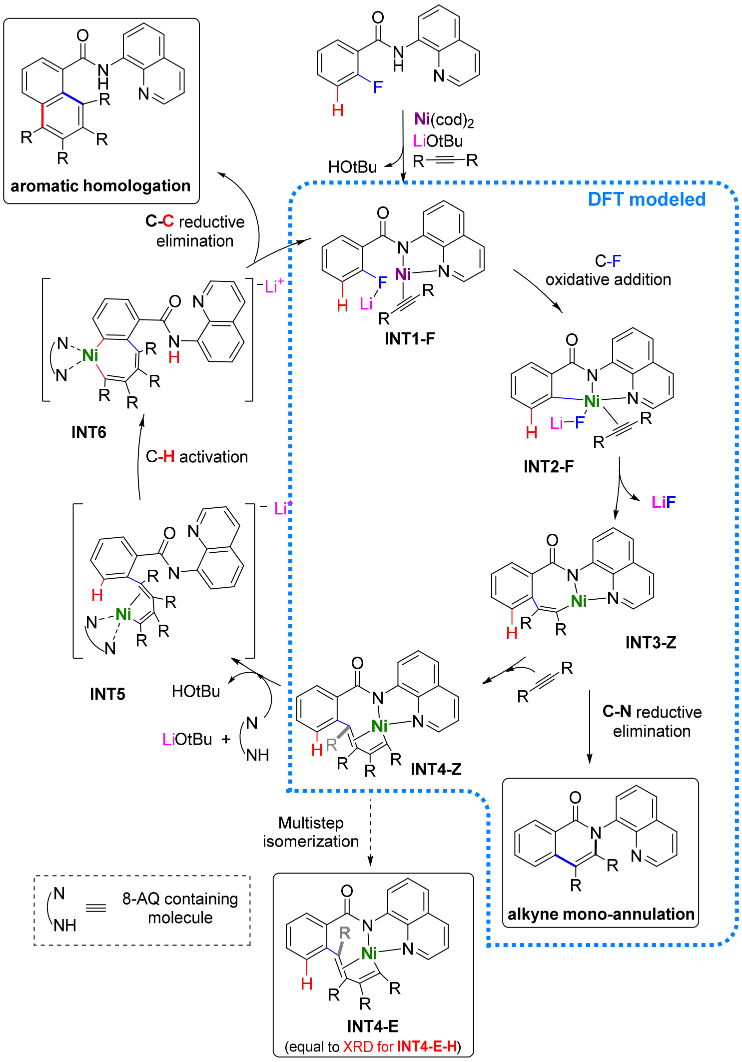

* This thesis chapter contains the calculations performed for the following publication:

L. Capdevila, T. H. Meyer, S. Roldán-Gómez, J. M. Luis, L. Ackermann, and X. Ribas, Chemo-Divergent Nickel(0)-Catalyzed Arene C–F Activation with Alkynes: Unprecedented C-F/C-H Double-Insertion. *ACS Catal*. **2019**. (***Accepted Manuscript***, doi:10.1021/acscatal.9b03620).

Summary

In this chapter, we present a computational mechanistic investigation of the key step of a nickel-catalyzed C-F activation (instead of a C-H activation) to form C-C bonds with alkynes that determines the chemoselectivity to an aromatic homologation or a mono-alkyne annulation product. Here, we focus our computational efforts in finding the selectivity of the C-F over the C-H activation; a suitable explanation for the formation of an unprecedented 9-membered nickelo-cyclic intermediate characterized by X-ray diffraction and the products obtained exploring several hypotheses of this part of the mechanism. In addition, we attempt to explain the chemo-divergent behavior of the C-C bond formation depending on the electronic character of the alkyne, with or without EWG as substituents that can yield the aromatic homologation product or the mono-alkyne annulated one, respectively.

6.1 State of the Art.

The ability of fluorinated motifs to drastically change the physicochemical and biological properties of almost any substance has positioned them as one of the must-contain features of target molecules for applications in several chemical related areas like catalysis, medicine, and material sciences.[166–169] In the pharmaceutical context, fluorinated motives confer stability and a greater lifetime to a large number of products and motives like aryl fluorides. However, it is quite common to find that such stability can be too strong, making a lead compound poorly biodegradable. Furthermore, in general, a transition metal-activated Ar-F functionalization is more challenging than Ar-H or Ar-Hal (Halogen, Cl, I, Br) activation, usually displaying low selectivities and requiring electronically biased polyfluorinated substrates.[170–172] Thus, it is of paramount relevance to develop new sustainable methods for the functionalization of C-F bonds as practical strategies that allow regio- and chemo- selectivities in fluorinated-arene moieties.

Regarding nickel-catalyzed C–C formation reaction via C–F cleavage of fluoroarenes, a few cross-coupling reactions of the type Kumada-Corriu,[173–181] Suzuki-Miyaura[182–186] and Negishi[187] can be found. However, all these methods use activated aryl nucleophiles, such as highly reactive Grignard reagents, zincates and boronic acids as the coupling partner for the C–C formation via transmetallation (**Figure 1.1 a**).

Alkyne insertion reactions are compelling methods for the synthesis of cyclic compounds by means of transition metal-catalyzed C–H activations. Some examples can be found in the synthesis of isoquinolones,[188–192] indoles,[193–196] or even polysubstituted[197–199] arenes. In such a context, Chatani[200] and Huang[201] have reported nickel-catalyzed[105] aromatic homologation reactions by a double C-H activation using 8-aminoquinolines as directing groups (**Figure 1.1 b**).

Motived by the increasing interest in this topic, we developed a new nickel(0)-catalyzed cyclization of fluoroarenes by alkyne insertion reaction. Using catalytic amounts of Ni(COD)$_2$, the C-F activation is preferred over the C-H activation of fluoroarenes bearing an 8-aminoquinoline group (8-AQ) to yield isoquinolones (mono-alkyne annulation product) and polysubstituted arenes (aromatic homologation product). Furthermore, we were able to isolate an unprecedented organometallic nickel(II) metalacycle featuring a doubly inserted acetylene, as a key intermediate in the aromatic homologation mechanism (**Figure 1.1 c**).

To gain a better insight into the mechanism of the reaction, we decided to computationally study the essential steps to understand the chemo-divergent C-C formation with acetylene. Therefore, we computed the mechanism for the formation of the key isolated intermediates and also for the competitive reaction that yields the formation of isoquinolones, which is the favored event in the case that the alkyne has electron-withdrawing substituents in its structure.

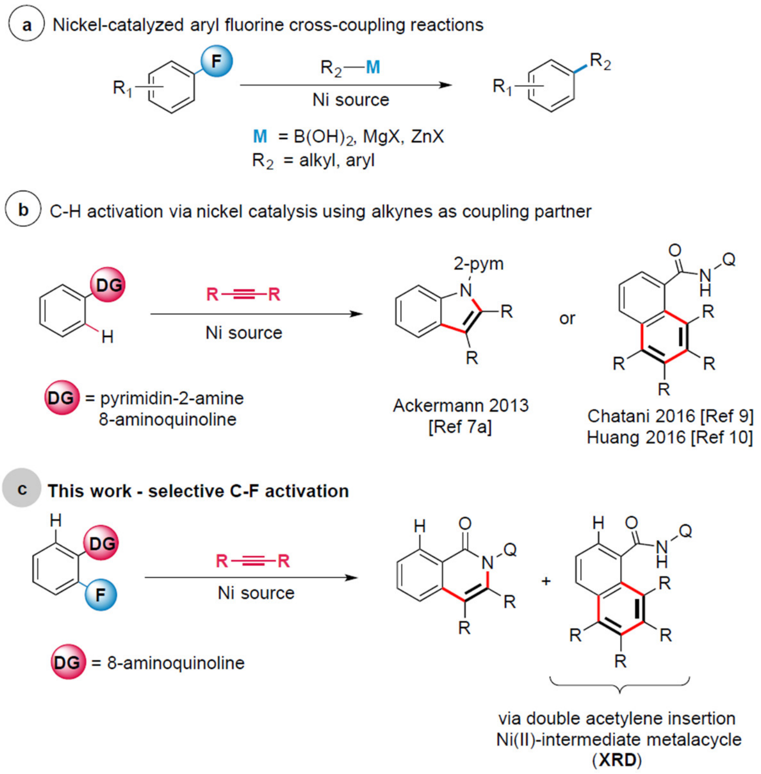

Figure 6.1 **(a)** Nickel-catalyzed C–F activation reactions using highly reactive, preactivated R-M nucleophiles. **(b)** Alkyne annulation via C–H activation by nickel catalysts. **(c)** Nickel-catalyzed C–F functionalization with internal alkynes.

6.2 Computational Details.

All DFT calculations were performed with the Gaussian 09 Revision E.01 program.[99] Geometry optimizations were carried out using the M06L functional[82] along with the def2SVP basis set and its respective density fitting basis set (w06).[135,136] To check the reliability of the chosen functional, some calculations with B3LYP[79,81,138,139] were also performed, along with the def2SVP basis set. Grimme's Dispersion model with Becke-Johnson damping function, GD3BJ[137], was added to the B3LYP functional to improve accuracy. Solvation effects were included as a Polarizable Continuum using the SMD model.[94] Subsequently, we performed frequency calculations to each of the optimized structures to ensure that all local minima have only real frequencies and all transition states have only one imaginary frequency. To calculate the Gibbs energy (ΔG), *i.e.*, to evaluate the entropic and enthalpic corrections, we used the python program Goodvibes (developed by Funes-Ardoiz and Paton).[97] The Gibbs energies were computed using the quasi-harmonic treatment (developed by Truhlar)[95] with a frequency scale factor of 1.0, a frequency cut-off value of 50 cm^{-1} and a temperature value of 413.15 K (140 °C). The free energy correction associated with the change from a standard-state gas phase pressure of 1 atm to a standard-state gas phase concentration of the different reactants was also included in the final Gibbs energy differences.

We also performed IRC calculations (using the LQA algorithm)[202,203] to verify that the transition states were connected with their respective reactants and products. Finally, single point energy calculations on the equilibrium geometries, including solvent effects, were computed with the more flexible basis set Def2-TZPV[135,136]and their respective functional (M06L or B3LYP).

Therefore, the Gibbs energy values (**ΔG**) reported in this chapter are calculated at M06L/Def2-TZVP//M06L/Def2-SVP & B3LYP-GD3BJ/Def2-TZVP//B3LYP-GD3BJ /Def2-SVP, including solvent effects (SMD), using the vibrational quasi-harmonic model (frequency cut-off 50 cm^{-1} & scale factor 1.0), assuming a temperature of 413.15 K, and a concentration of 0.02 M for the Ni catalyst, 0.2 M for the 8-AQ and 0.4 M for DPA.

6.3 Results and Discussions.

The optimized experimental conditions of the nickel-catalyzed arene C-F activation (specifically 2-fluoro-N-(quinoline-8-yl)benzamide) with the alkyne (diphenylacetylene, DPA) are described in **Figure 6.2**. Under these conditions, it was possible to generate the aromatic homologation products as the major species (63%) and the mono-alkyne annulation product as the minor product (17%). In addition, after just five minutes of reaction, a stable intermediate was detected, isolated and characterized by single-crystal X-ray diffraction (**Figure 6.2**). The ^{1}H NMR quantification of this intermediate species accounts for ~89% of the total Ni content. Furthermore, to verify that the isolated molecule was an intermediate and not a side product of the reaction, the isolated intermediate was dissolved in 1,4-dioxane and exposed to the same temperature (140 °C), and the mixture yielded the desired aromatic homologation product (23%). In the case that the isolated INT4 is combined with five equivalents of **1a** and base (LiOtBu) at 140 °C and in 1,4-dioxane, the reaction proceeds faster and with higher yields (41%). Therefore, the reaction requires an extra bidentate ligand (it can be reactant **1a** or product **2a**; the latter would be in an autocatalytic fashion) to proceed to the polysubstituted arene product **2a**.

Because of the high relevance of this intermediate, we decided that our calculations should focus up to the formation of the **INT4** intermediate. Indeed, this species is one of the keys that defines the chemoselectivity for the aromatic homologation path.

Based on the reported literature for C-H nickel activation by alkyne insertion with 8-aminoquinolines[200,201], we proposed a mechanistic path for the formation of the **INT4** intermediate (**Figure 6.3**). First, the strong base, Lithium tert-butoxide, deprotonates the amide group of the substrate **1a** and the Nickel coordinates to the just-formed bidentate ligand, **8-AQ**, to generate **INT1**; then, an oxidative addition over the C-F bond occurs (instead of activating the C-H) yielding the intermediate **INT2**. We believe that it is at this point that the LiF is formed, leaving a nickel-ligand vacancy that allows the coordination of the diphenylacetylene to form **INT3** by nickel-assisted alkyne insertion. After this, a second alkyne insertion can occur, yielding the isolated intermediate, or a reductive elimination, producing the alkyne mono-annulation product.

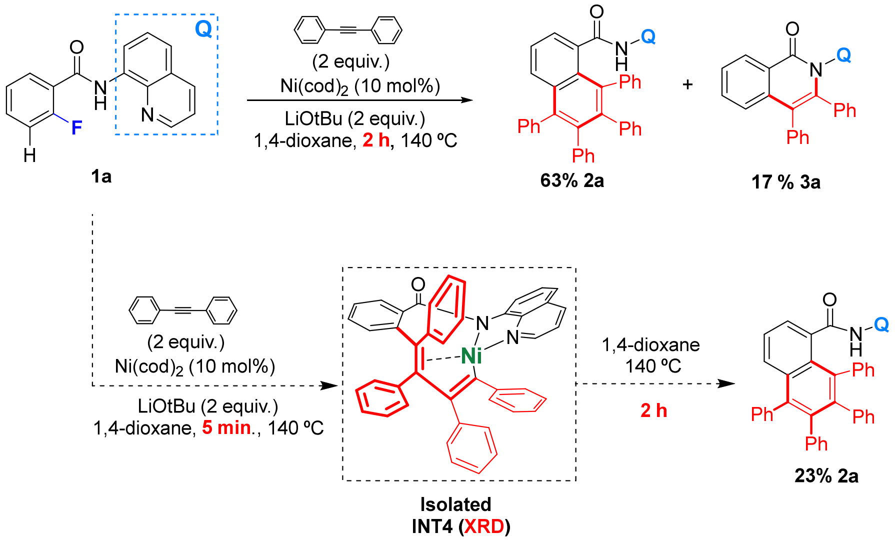

Figure 6.2 C-F functionalization of substrate **1a** with diphenylacetylene and a Nickel(0) source (0.1 eq) to yield the aromatic homologation product **2a** and the alkyne mono-annulation product **3a**. Intermediate **INT4** can be isolated after five minutes of reaction. Following similar reaction conditions, **INT4** yields **2a**.

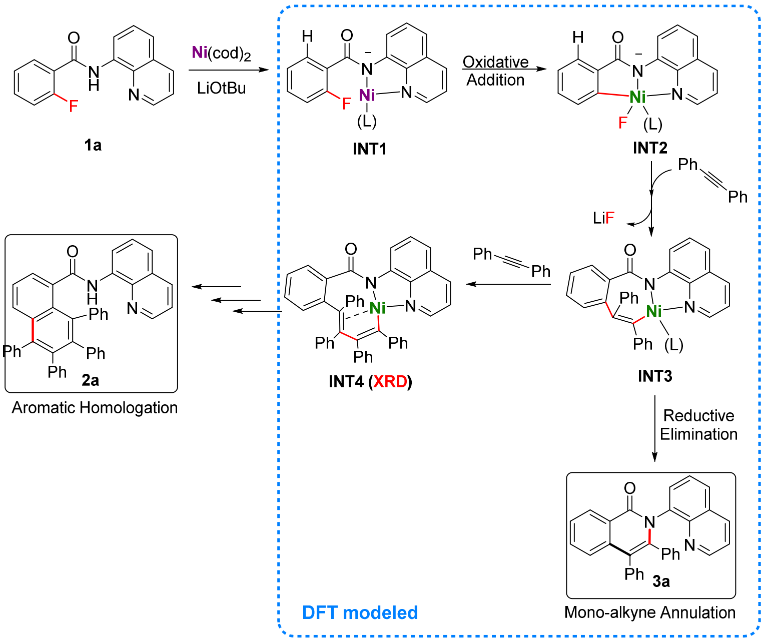

Figure 6.3 Initial mechanistic proposal of the formation of **INT4** and mono-alkyne annulation product. Highlighted in blue is the reaction steps that we simulated by DFT calculations

From this proposal, we considered that it would be relevant to understand the chemoselective activation of C-F over C-H in the conversion from **INT1** to **INT2**, the divergent behavior of the **INT3** to form **INT4** via a second alkyne insertion, and the formation of **2a** via reductive elimination from the same **INT3**. In this manner, we will be able to find a suitable explanation for the selectivity of the reaction based on DFT calculations and the previously obtained evidence from the experiments.

6.3.1 C-F activation versus C-H activation

The first thing that we calculated was the selectivity of the C-F over the C-H activation because it is one of the novel aspects of the experimental results. Therefore, we started the calculations from the reactants Ni(COD)$_2$, Diphenylacetylene (DPA), and **8-AQ** (which is the deprotonated product of the acid-base reaction of LiOtBu with **1a**). We explored several conformations of **8-AQ** and chose the most stable one, which happened to be the one with the explicit counterion, Lithium cation, in a coordinative fashion with the F moiety and the deprotonated N amide moiety of **8-AQ**.

Then we proceeded to the formation of **INT1**. In this case, we also explored different conformers from which two were selected: the most stable that showed a tendency (or the appropriate geometry) to activate the C-H bond (**INT1-H**) and another one that showed C-F activation as the preferred one (**INT1-F**). As **Figure 6.4** shows, both intermediates are slightly endergonic, although the Gibbs energy of **INT1-H** is 3.5 kcal/mol lower than **INT1-F**. On the contrary, the stability order of the transition states changes to $TS_{C\text{-}H}$ over $TS_{C\text{-}F}$ by 4.6 kcal/mol (**Figure 6.4**). This clearly supports C-F activation as the preferred kinetic path over the C-H activation. Moreover, the yielded intermediates **INT2-H** and **INT2-F** showed a surprisingly large difference in Gibbs energy (49.4 kcal/mol), favoring the latter as the more stable one (exergonic).

Interestingly, the plunge in energy during the formation of **INT2-F** is due to the formation of the very stable salt LiF. Without the presence of the Li cation, experimentally, the reaction does not proceed (*i.e.* using KOtBu as a base), which emphasizes the relevance of the LiF formation. It is worth highlighting that the analogous species of **INT2-H** and **INT2-F** without the DPA ligand were higher in energy (without the DPA they can adopt square planar geometries, which are in principle more stable). We believe that the high energy of **INT2-H** is caused by the instability of the generated hydride. In summary, the C-F activation is kinetically and thermodynamically favored over the C-H activation, which is in agreement with the experimental result.

We also found one transition state (**$TS_{2\text{-}3}$** = 23.2 kcal/mol) that correlates the C-C bond formation between the aryl-C of **INT2** and the alkyne-C of the DPA moiety that yields **INT3a-Z**, which is a conformational isomer of **INT3-Z** (*vide infra*). We were not able to find a single-step conformational change connecting **INT3a-Z** to **INT3-Z**. We hypothesize that there must be a multistep conformational change that connects both isomers. However, in our case, it is not the main focus of interest. What is relevant is that **INT3a-Z** is higher in energy than **INT3-Z**, which is the most stable one of all the explored INT3 isomers (*vide infra*).

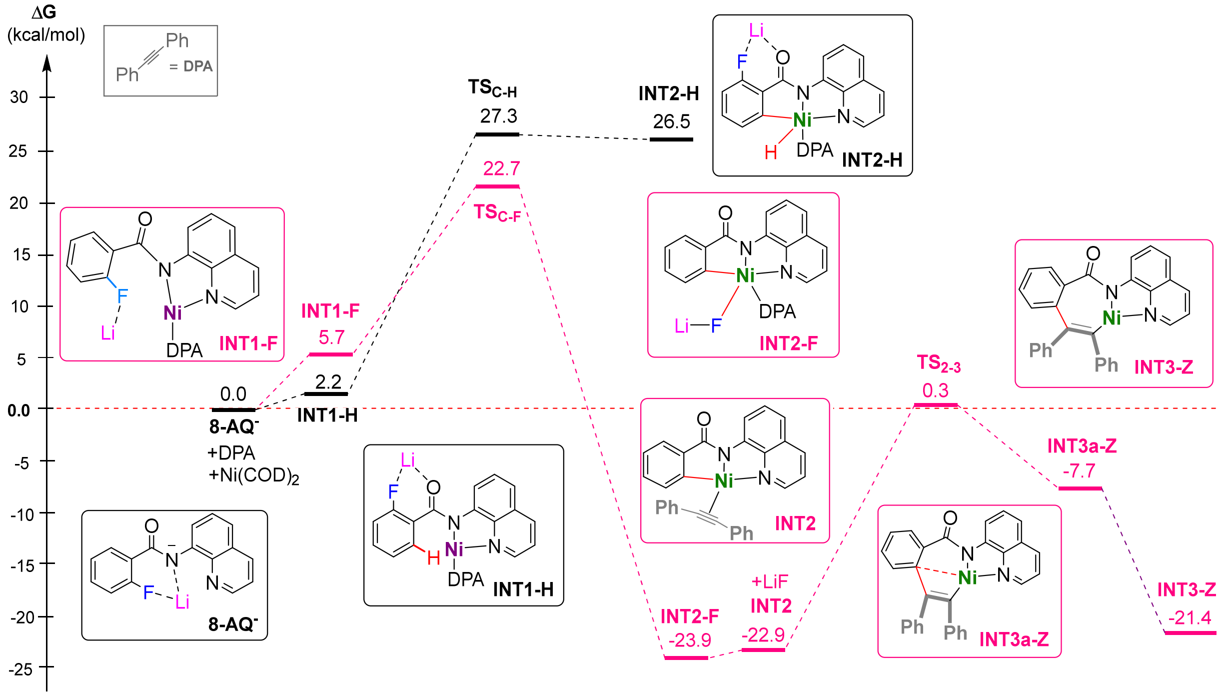

Figure 6.4 Gibbs energy profile for the C-F (pink) versus C-H activation (black) via **INT2-F** and **INT2-H**, respectively, followed by the first DPA insertion at **INT2-F**. The reaction was modeled by DFT at M06L/Def2-TZVP//M06L/Def2-SVP level of theory.

6.3.2 The reactivity of **INT3**

Since the structure of **INT3** contains an alkene moiety (generated by the alkyne first insertion), we can have two possible configurational isomers, **INT3-E** or **INT3-Z**. **INT3-E** has the substituents of the alkene directed in opposite directions (if one is down, the other is above the alkene bond plane); **INT3-Z** has the phenyl substituents on the same side of the alkene plane. This implies that each of these isomers could react with another diphenylacetylene to generate different **INT4** isomers, **INT4-E** and **INT4-Z** (see Figure 6.5 A). Although the isolated intermediate has the structure of the **INT4-E** isomer, we considered it relevant to study both systems to gain a better insight into the reactivity of the two isomers.

In the case that **INT3** reacts to produce the mono-alkyne annulation, the situation is different, since both isomers, **INT3-E/Z,** lead to the same product, **3a**. This is because the alkene moiety is part of a planar aromatic structure (isoquinolone), in which the alkene can only acquire the Z configuration. Therefore, we would have two different transition states coming from different isomeric reactants but yielding the same product. Since the reductive elimination is an intramolecular reaction, the presence of a ligand L, in principle, is not necessary for the reaction to happen (as opposed to the second alkyne addition, which requires a second DPA as ligand). Hence, for each isomer, two mono-alkyne annulation reactions are possible: with and without the Diphenylacetylene as a ligand (see Figure 6.5 B).

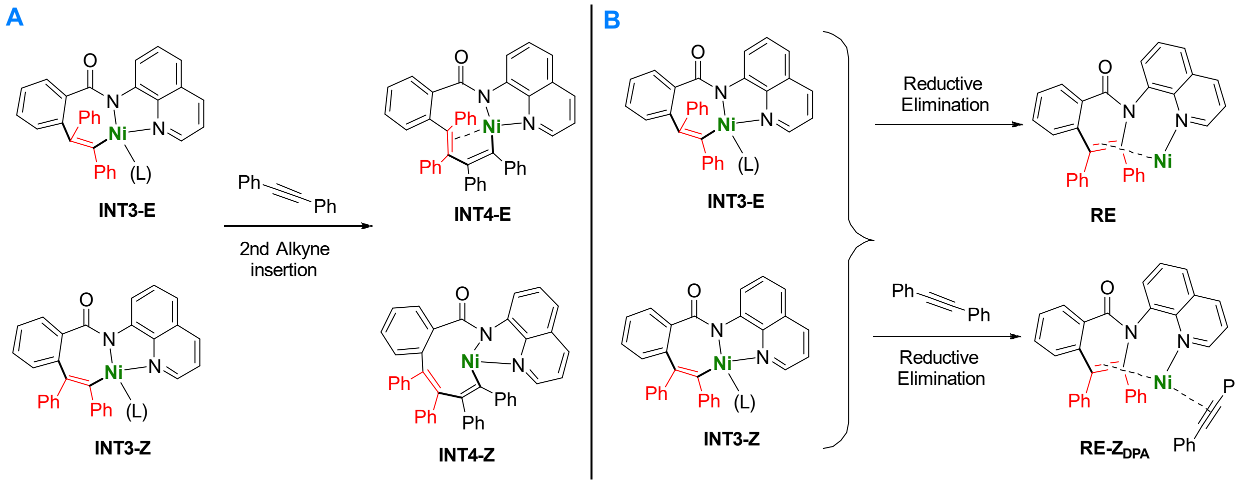

Figure 6.5 A) Representation of the isomers E/Z for the intermediates INT3 and INT4. **B)** Representation of the products and reactants of the reductive elimination that leads to the mono-alkyne annulation products, with and without an extra PDA ligand**.**

Figure 6.6 shows the Gibbs energies profiles for the three type events calculated (2nd DPA insertion, reductive elimination with DPA, and reductive elimination without DPA as ligand) that transform **INT3-Z** (B) and **INT3-E** (A) into products.

Profile A shows the reactivity of isomer **INT3-E** (the one that generates the experimentally characterized isomer **INT4-E**). One can see that the Gibbs energy of the adduct **INT3-DPA** is higher (>15 kcal/mol) than that of the reactants at infinite distance —we tried several coordinative-orientations between **INT3-E** and DPA but in all cases they had a higher energy than reactants. Following the light blue line in the Gibbs energy profile, we find the transition state for the second DPA insertion (33.4 kcal/mol), which is quite high considering that **INT3-E** is already a reactive species. In the case of the reductive elimination, the extra DPA stabilizes the transition state, lowering the Gibbs energy by 10.5 kcal/mol (from 34.8 kcal/mol without DPA to 24.3 kcal/mol with DPA). The most stable product structure in Profile A is **INT4-E**, whose Gibbs energy is about 15 kcal/mol lower than the C-N formation product.

In profile B the reactivity of the **INT3-Z** is explored. The comparison of profile B with A shows that in general the energy of the Z-isomers is lower than the energy of their counterparts in E-conformation, except for the products **RedEli** and **RedEli**$_{\mathbf{DPA}}$ (as they become the same product regardless of the initial **INT3-E/Z** isomers) and the product **INT4**. The high thermodynamic stability of **INT4-E** shown by our calculations is in agreement with the experimental isolation and characterization of this intermediate.

In addition, in profile B, the transition state Gibbs energy for the second DPA addition (**TS-Z$_{3-4}$**) and the reductive elimination with DPA ligand (**TS-Z$_{RE-DPA}$**) are quite similar, with a mere difference of 1.2 kcal/mol. This is, indeed, in agreement with the experimental fact that the reaction can yield both products, the aromatic homologation product (**2a**) and the mono-alkyne annulation one (**3a**), although the latter in a lower yield.

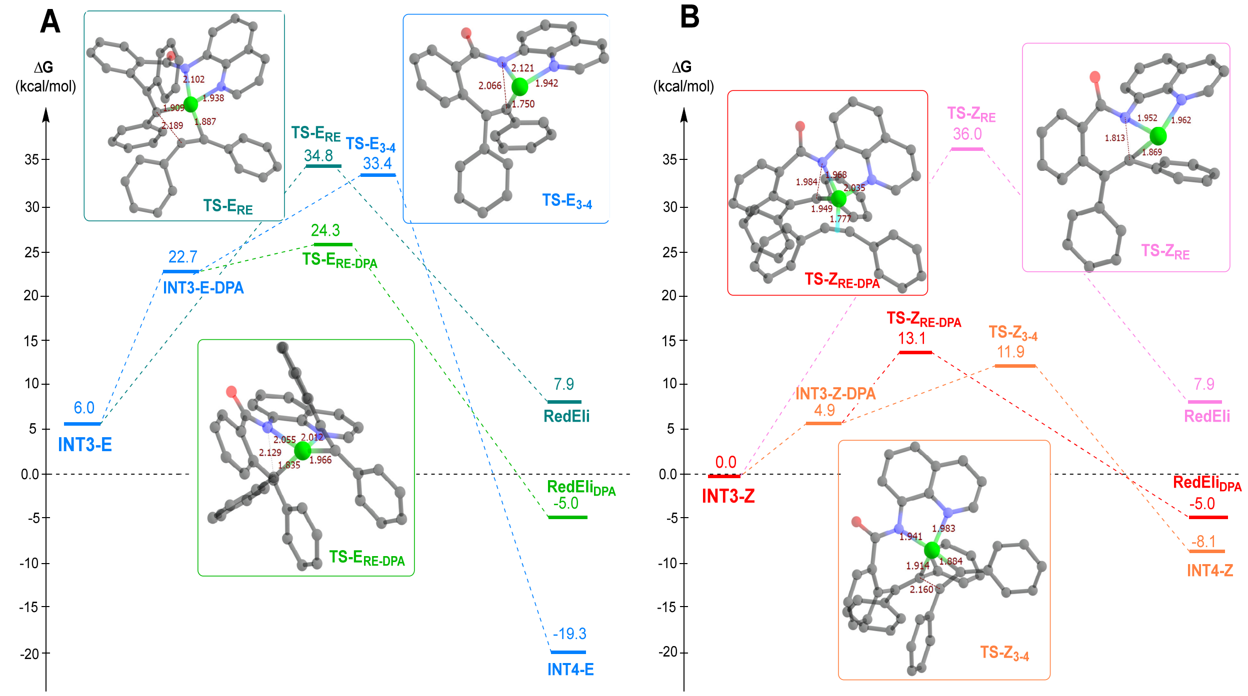

Figure 6.6 A) Gibbs energy profile for the three reactivity paths of **INT3-E**: second DPA insertion (blue), reductive elimination without extra DPA (teal), and reductive elimination with extra DPA ligand (green). **B)** Gibbs energy profile for the three reactivity paths of **INT3-Z**: second DPA insertion (orange), reductive elimination without extra DPA (violet), and reductive elimination with extra DPA ligand (red). The reaction was modeled at M06L/Def2-TZVP//M06L/Def2-SVP level of theory; energies given in kcal/mol.

It is noteworthy that in both profiles the transition state energy for the reductive elimination without DPA is quite similar and very high in energy (*ca*. 35 kcal/mol). From this we can infer that the absence of an extra ligand to stabilize the nickel complex that is "losing" one of its ligands (the alkene) during the annulation takes a drastic toll on the energy barrier.

Taking into account that the stabilization on the Nickel by the ligands can have a greater effect on the Gibbs energy than the energy gap between the two alkene conformations (like in the previous example), we decided to explore the geometric disposition of the ligands around the Nickel(II) to understand why **INT4-E** was more stable than its counter-isomer **INT4-Z**. Indeed, we found that the coordination of the ligand around the Nickel is the one that grants the extra stability. In the case of **INT4-Z**, the ligands are arranged in a semi square planar arrangement around the Nickel with a distortion from the plane of 50° (the torsion angle of N1N2C3C4, where N1, N2, and C3 are almost on the same plane of the Nickel) as shown in **Figure 6.7 A**. On the other hand, in the case of **INT4-E**, the ligands are distorted from the plane by -23° (torsion angle of N1N2C3C4 in **Figure 6.7 B**). Therefore, the E-isomer has a more square planar character than the Z-isomer, which confers to the former the extra stability to overcome the disfavoring energy that comes from being the lesser stable alkene conformation.

Even though we have rationalized parts of the reactivity of **INT3**, this description of the system does not fully explain why **INT4-E** is isolated, since the most feasible reaction path for the formation of **INT4** is via the Z-isomer. Therefore, to find a plausible explanation we explored the effect of different factors that we considered relevant to understand the nature of the connection between the isolated intermediate **INT4-E** and the events during the reaction.

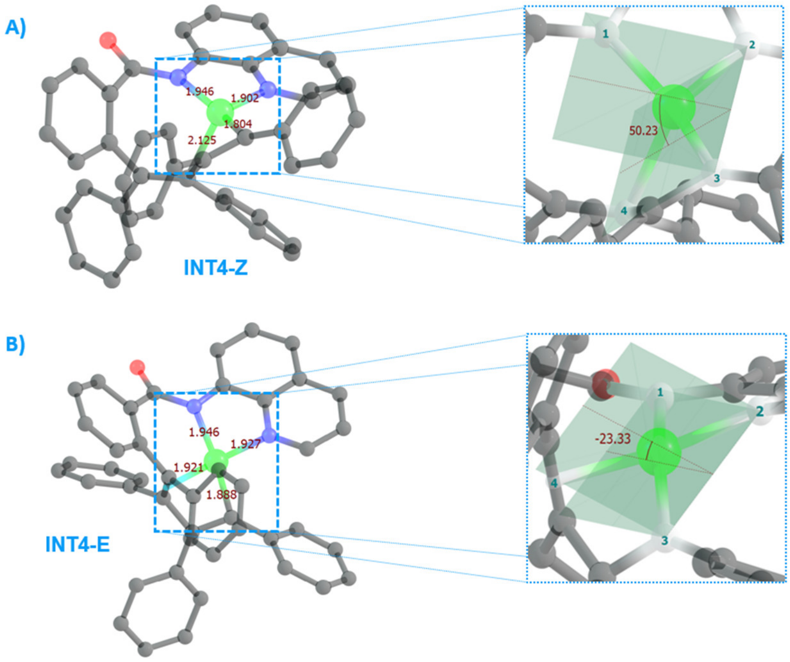

Figure 6.7 Optimized geometries of a) **INT4-Z** and b) **INT4-E**. The enlarged sections highlight the distortion of the square planar geometry of the ligands in the complex by measuring the dihedral angle N1N2C3C4. Atom-color code: Carbon, Nitrogen, Oxygen, Nickel (Hydrogen atoms have been omitted for clarity).

6.3.3 Exploring the formation of **INT4-E**.

First, we examined the effect of varying the functional for the calculations. For this, some of the optimized species were obtained with another functional, in this case, B3LYP-GD3BJ, using the same basis sets and the same approximations as in the M06L calculations (see **Figure 6.8**). In general, the same pattern was obtained and both functionals led to the same conclusions: i) **INT3-Z** is more stable than **INT3-E** while **INT4-E** is more stable than **INT4-Z**; ii) the second DPA-insertion is kinetically more favorable than the mono-DPA annulation; iii) the transition states connected to **INT3-Z** have a far lower energy than their counterparts connected to **INT3-E**.

Next, we attempted to find a transition state of the isomerization between E and Z **INT3** isomers. Unfortunately, we were not able to find a transition state for this reaction. Although we performed several relaxed scans on the PES to find the isomerization transition state and several attempts by chemical intuition, the electronic energy of the scans scaled up to approximately 50 kcal/mol; therefore, this process did not seem feasible.

Moreover, we exhaustively tried to find a simple mechanism for the isomerization between **INT4-Z** and **INT4-E**, but it was extremely difficult due to the conformational flexibility of the ligands.

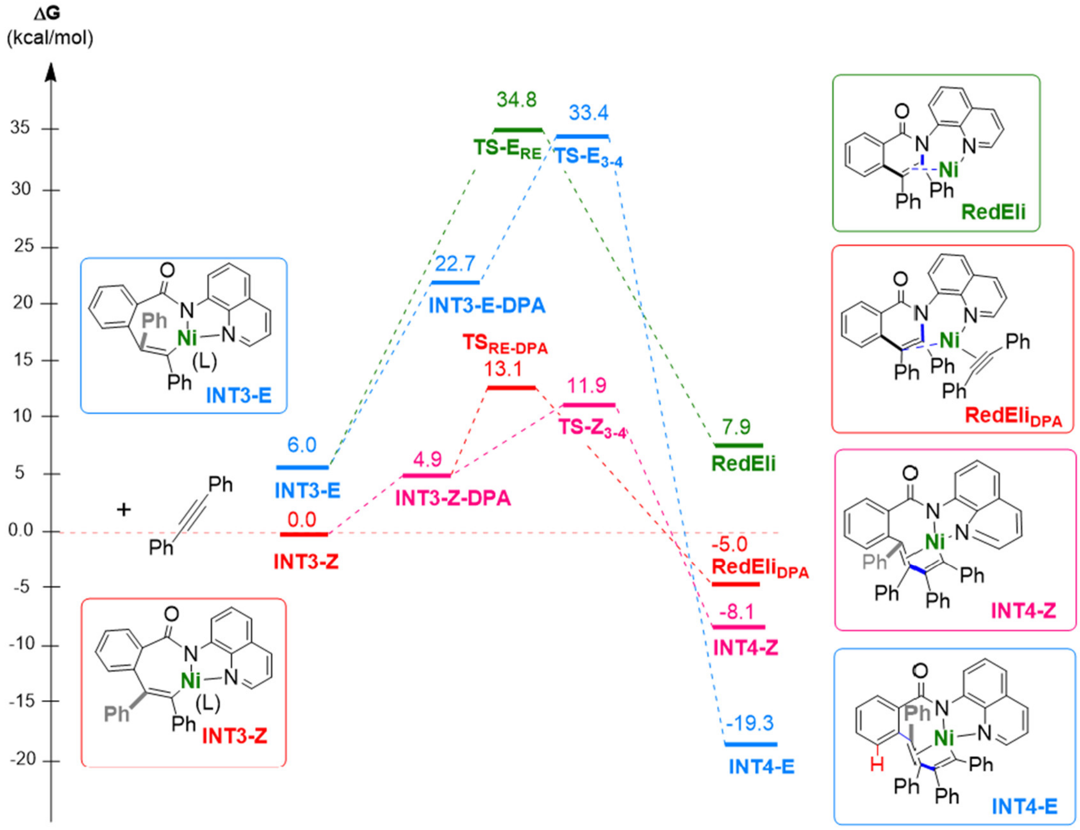

Figure 6.8 Gibbs energy profiles for the transition from the mono-alkyne intermediates (**INT3-E** or **INT3-Z**) to the double inserted alkyne compounds **INT4-E** (in blue) or **INT4-Z** (in pink), as well as the pathways for the intramolecular alkyne mono-annulation from **INT3-E** (in green) and from **INT3-Z** with a second DPA coordinated to the metal (in red). The reaction was modeled at M06L/Def2-TZVP//M06L/Def2-SVP level of theory; energies given in kcal/mol.

In addition, we investigated the **INT3** formation, since the key to understanding the stereoselectivity that leads to the experimental isolation of **INT4-E** might be found in the kinetics of the first alkyne insertion. In **Figure 6.9** the transition state for the formation of both **INT3** isomers is shown. We must say that we did not start the Gibbs energy profile for the reaction from **INT2** because this intermediate is a negatively charged species, and that would require the use of diffuse functions in the basis set (which, in general, do not converge easily). Therefore, we stared the Gibbs energy profile from an intermediate (**INT2.5**) where it is assumed that LiF is already formed (see **Figure 6.9**). As we might expect, **INT2.5** is a three-coordinated Nickel and therefore slightly unstable. Hence, when a DPA molecule is added as a ligand, the complex gains stability. The isomeric divergence is generated in the following step, when the DPA is inserted into the activated C-Ni site, yielding two different transition states, which favors the formation of the Z isomer, instead of the E- isomer (**TS-E$_{2.5\text{-}3}$** is an approximate TS with a fixed coordinate, since we were not able to find the relaxed TS for this step. Nevertheless, this approximate value allowed us to discard this path as the most favorable one).

These results are in line with previous findings; however, this fact does not explain why we get the intermediate **INT4-E** experimentally while the Z-isomers route is the most efficient path computationally.

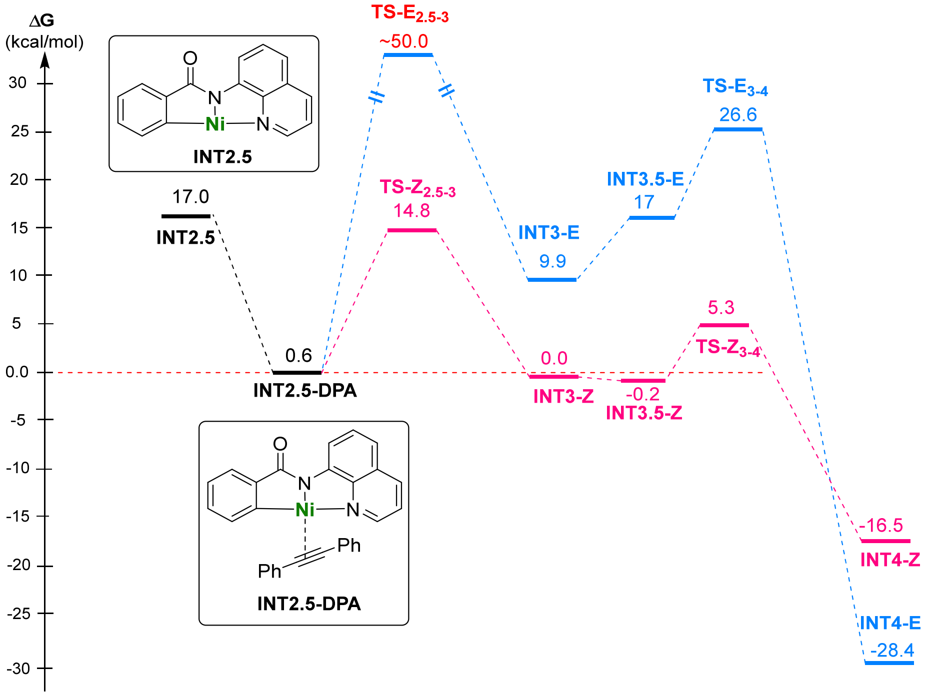

Figure 6.9 Gibbs energy profile of the reaction between **INT2.5** and DPA to form **INT4-E** or **INT4-Z**. Highlighted in black are the species located before the formation of **INT3-Z/E**. The value of **TS-E$_{2.5\text{-}3}$** is approximated. The reaction was modeled at B3LYP-GD3BJ/Def2-TZVP//B3LYP-GD3BJ/Def2-SVP level of theory; energies are given in kcal/mol.

Continuing our investigation of the formation of **INT4-E**, we wondered whether the F$^-$ ligand plays a role defining which isomer is the most stable. Based on this, we computed several structures that included the Fluoride anion as a ligand and explicit Lithium ions as counterions. We only show the most relevant ones in **Figure 6.10** to highlight two facts: the Z-isomers are still more stable than the E-isomers; the formation of the LiF molecule, as expected, is far more favorable that having the ions separately interacting with the complex.

Finally, we explored another hypothesis based on the intermediate identified by Huang and coworkers [201], in which two 8-aminoquinolines are coordinated to the Nickel center. In our case, we wanted to see if this plausible **INT3-AQ** was more stable in E or Z conformation. Therefore, we optimized two different types of structure for this pair of isomers: one with both deprotonated 8-aminoquinolines, adding an explicit Li^+ counterion to compensate charges in the Nitrogen region and the other pair with the counterion in the Oxygen region of the amide (see **Figure 6.11**). Again, in both cases the Z-isomer of **INT3-AQ** was lower in energy.

What we can learn from computationally exploring all these different pathways for **INT3** formation is that **INT3-Z** is kinetically and thermodynamically more favored than its stereoisomer **INT3-E** by at least 10 kcal/mol. Therefore, we have arrived at the conclusion that the reaction path proceeds via the Z-isomer. However, there must be a multistep isomerization that connects the intermediate **INT4-E**, which was experimentally isolated, with the intermediate **INT4-Z**, the reactive species in the catalytic cycle.

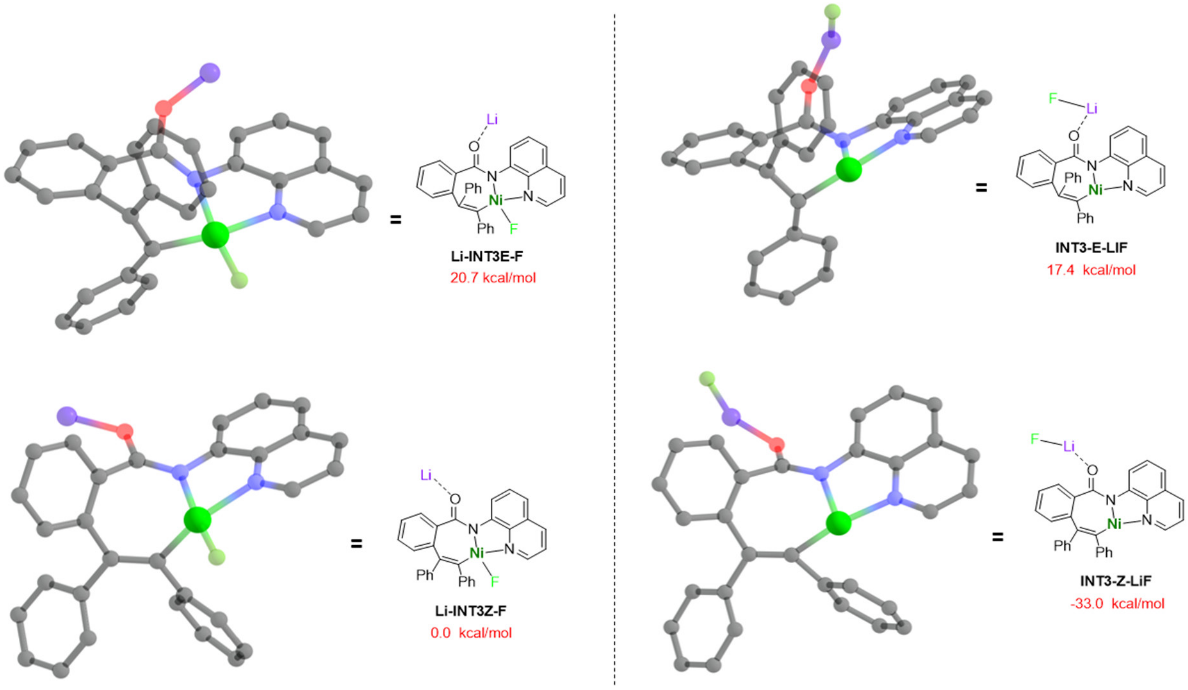

Figure 6.10 Optimized structures and relative Gibbs energies of INT3 species with explicit F- and Li^+ ions included. The ones on the left assume Fluoride as Nickel ligand, and the ones on the right assume the LiF already formed. The energy values are calculated at B3LYP-GD3BJ/Def2-TZVP//B3LYP-GD3BJ/Def2-SVP level of theory. Atom-color code: Carbon, Nitrogen, Oxygen, Nickel, Fluorine, Lithium (Hydrogen atoms have been omitted for clarity).

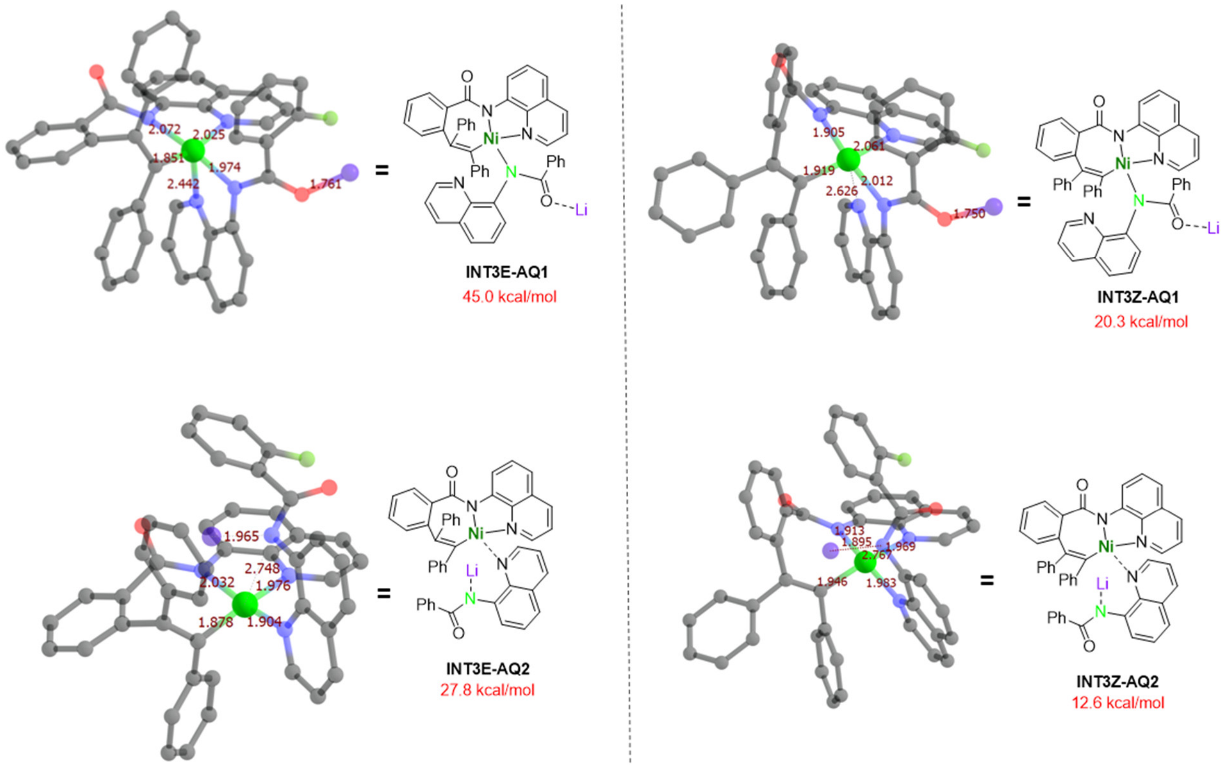

Figure 6.11 Optimized structures and relative Gibbs energies of **INT3** bonded to a second 8-Aminoquinoline (**INT3-AQ**). **AQ1** E and Z isomers with the counterion bonded to the carbonyl are depicted on top; the pair at the bottom (**AQ2**) are both isomers with the counterion bonded to the N of the amide. The Gibbs energy values are calculated with M06L/Def2-TZVP//M06L/Def2-SVP level of theory and the zero of energy is assumed as the reactants at infinite distance. Atom-color code: Carbon, Nitrogen, Oxygen, Nickel, Fluorine, Lithium (Hydrogen atoms have been omitted for clarity).

In summary, we propose a mechanism for the reaction (**Figure 6.12**), based on the evidence we found experimentally, computationally, and on similar literature reported previously (reported by Huang And Chatani)[200,201] for aromatic homologation by activating C-H bonds with Ni sources.

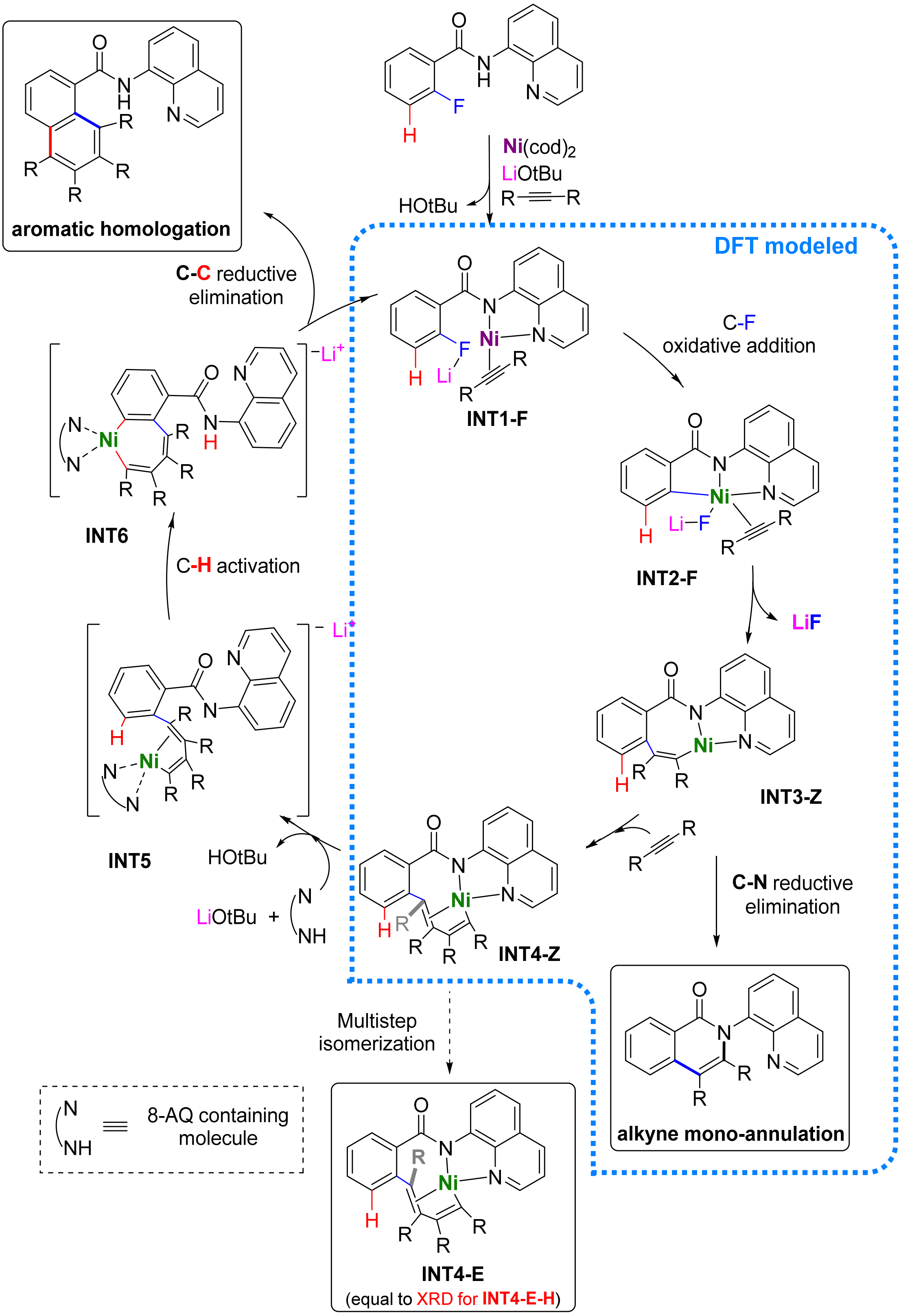

Figure 6.12 Global mechanistic proposal for the formation of the aromatic homologation product and the alkyne mono-annulation one. Ni(0) is depicted in purple and Ni(II) in green.

6.3.4 The effect of the *p*-CF$_3$ substituent.

According to the experimental results, when the reaction is performed with *p*- substituted alkyne with an EWG, such as *p*-CF$_3$-diphenylacetylene, the reaction prefers to yield the mono-alkyne annulation product instead of the aromatic homologation product (see **Table 6.1**). Based on this, we computationally explored the divergent reaction of **CF$_3$-INT3** with *p*-CF$_3$-diphenylacetylene to generate **CF$_3$-INT4** (which leads to **2aa**) or **CF$_3$-RedEli** (which leads to **3aa**) to better understand the change of the reaction with DPA.

Table 6.1 C-F functionalization using different symmetric alkynes. Highlighted in blue is the extreme case in which the aromatic homologation is blocked by using CF$_3$ substituent.

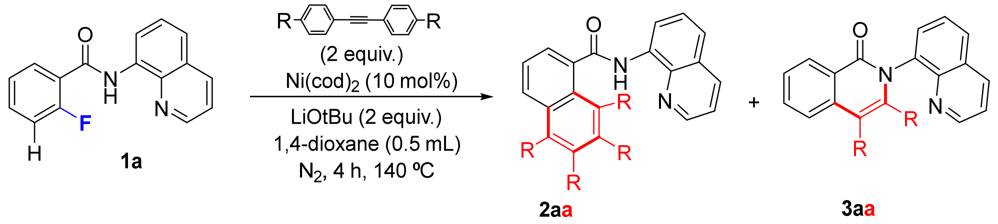

Entry	R	Yield of 2ax[a]	Yield of 3ax[a]	Total yield
1[b]	H	63 % **2aa** (60 %)	17 % **3aa** (11 %)	80 %
2	Me	40 % **2ab** (40 %)	14 % **3ab** (6 %)	54 %
3	F	40 % **2ac** (36 %)	43 % **3ac** (34 %)	83 %
4	Cl	34 % **2ad** (30 %)	39 % **3ad** (29 %)	73 %
5	Br	37 % **2ae** (25 %)	37 % **3ae** (34 %)	74 %
6	MeC(O)	-	36 % **3af** (22 %)	36 %
7	CF$_3$	-	**88 % 3ag (83 %)**	**88 %**

Then, we optimized all the related species for both E/Z-isomers of **CF$_3$-INT3** and **CF$_3$-INT4** with their respective adducts and transition states, as well as the transition states and products for the formation of **CF$_3$-RedEli** with or without an extra *p*-CF$_3$-diphenylacetylene (CF$_3$-DPA) ligand.

Comparing the Gibbs energies in **Figure 6.13** with those in **Figure 6.6**, we can see that in general the patterns are similar. Interestingly, the gap between the most relevant transition states, **CF$_3$-TS-Z$_{RE\text{-}DPA}$** and **CF$_3$-TS-Z$_{3\text{-}4}$**, became slightly smaller (for the reaction with DPA, it was 1.2 kcal/mol; for CF$_3$-DPA, the difference is only 0.6 kcal/mol, the half of the gap for DPA). Our DFT calculations do not accurately reproduce the experimental "blocking" of the aromatic homologation when CF$_3$-DPA is used. Nevertheless, the pattern shown by the stabilization of **CF$_3$-TS-Z$_{RE\text{-}DPA}$** with respect to **CF$_3$-TS-Z$_{3\text{-}4}$** is in agreement with the experimental results taking into account the intrinsic errors of the DFT calculations (*i.e.* about 2 kcal/mol).

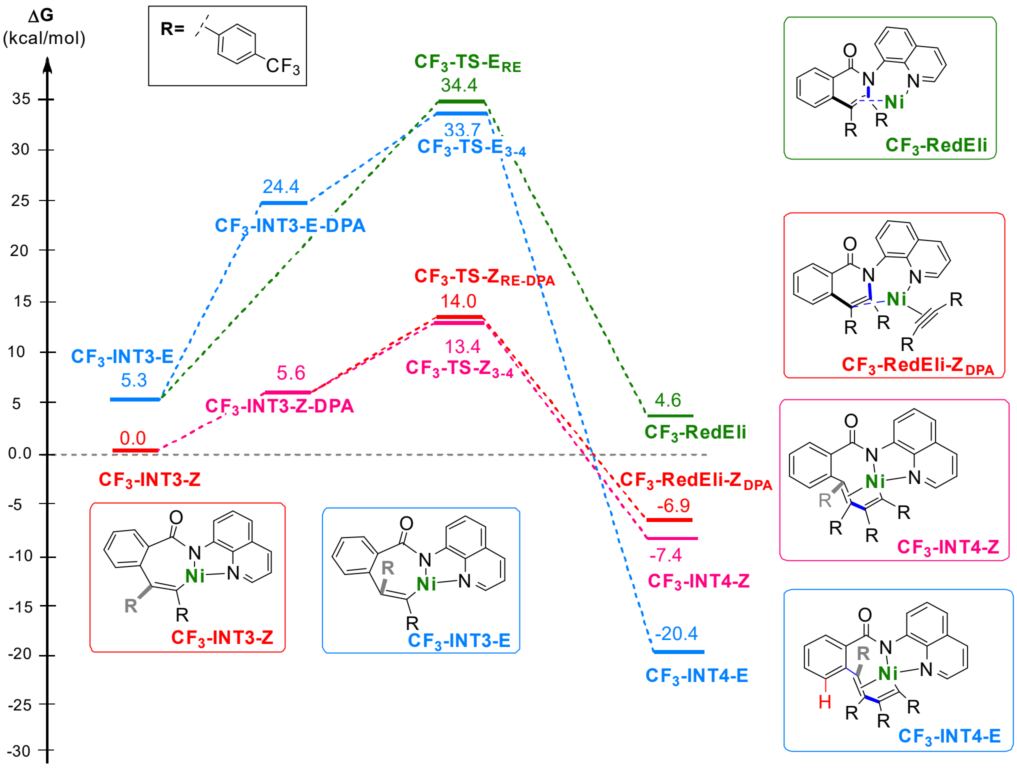

Figure 6.13 Gibbs energy profiles for the transition from the mono-alkyne intermediates (**CF_3-INT3-E** or **CF_3-INT3-Z**) to the double inserted alkyne compounds **CF_3-INT4-E** (in blue) or **CF_3-INT4-Z** (in pink), as well as the pathways for the intramolecular alkyne mono-annulation from **CF_3-INT3-E** (in green) and from **CF_3-INT3-Z** with a second CF_3-DPA coordinated to the metal (in red). The reaction was modeled at M06L/Def2-TZVP//M06L/Def2-SVP level of theory; energies given in kcal/mol.

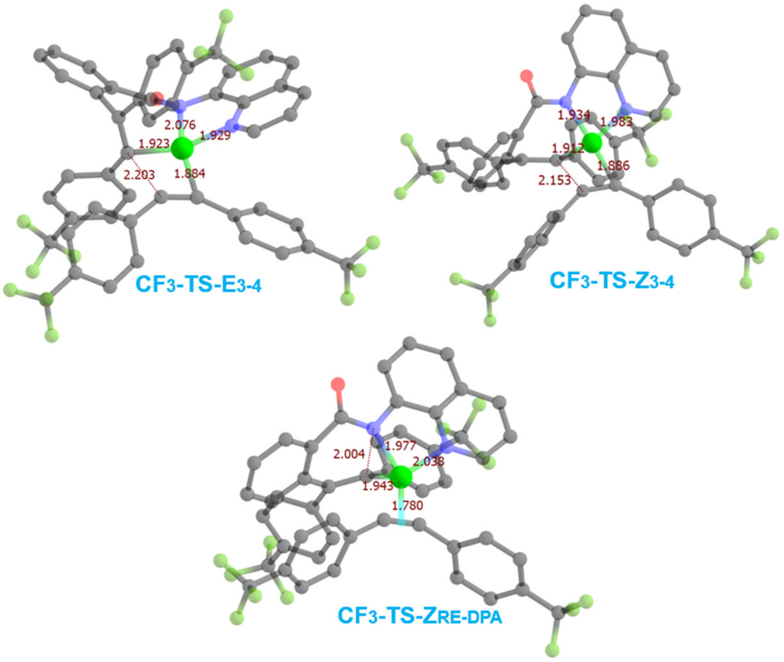

Figure 6.14 Selected optimized structures of the transition states, **CF_3-TS-$E_{3\text{-}4}$**, **CF_3-TS-$Z_{RE\text{-}DPA}$**, and **CF_3-TS-$Z_{3\text{-}4}$**.

To summarize, in this chapter, we have used computational calculations to improve the comprehension of the Ni-catalyzed chemo-divergent C-F activation with alkynes. The DFT results led to propose a mechanism for the two observed reactions: aromatic homologation and alkyne mono-annulation. We have analyzed the important role of both the E and Z isomers in the reactivity. In addition, we simulated the effect of EWG alkyne substituents in the reaction, maintaining a fair compromise between the experiment and the theory.

Chapter 7

On-ligand Amine-to-Amide Formation by CO Insertion on a Well-defined Iron(II) Complex

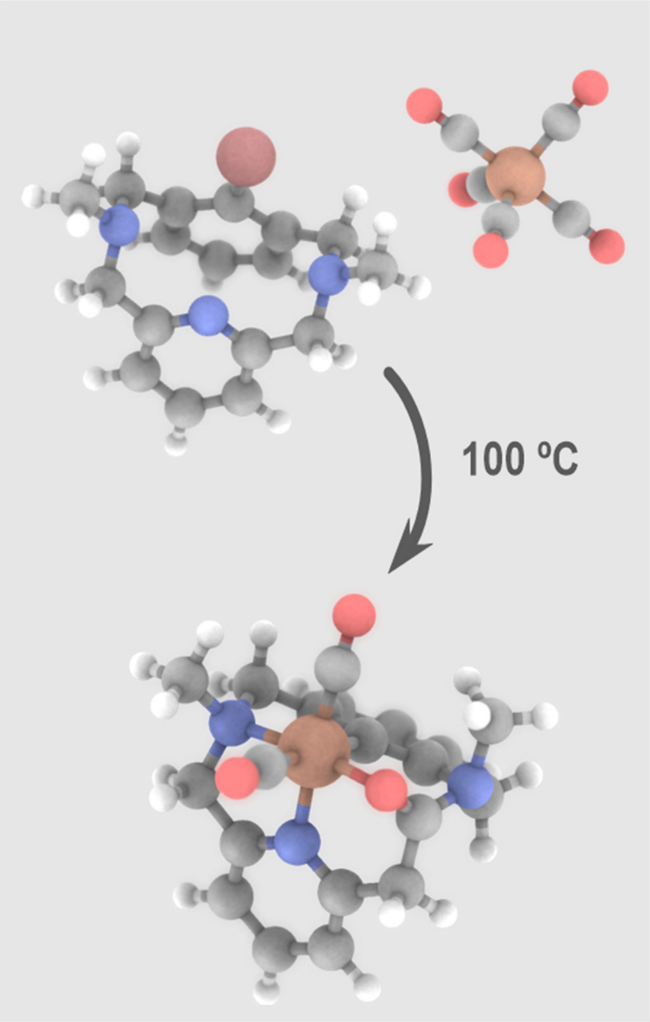

Summary

In this chapter, we will review the different computational approaches that we performed in an attempt to comprehend the reactivity of a well-defined Fe(II)-complex, specifically, its unexpected conversion of a lateral amino moiety of the ligand into an amide group by means of an apparent CO insertion. Despite having explored different options, the mechanism of this unique reaction remains unclear.

Sate of the Art.

From all the family of 3d transition metals, the most relevant of all might be Iron (the most abundant transition metal) because of: i) its presence in all kinds of systems, from living organisms to inert materials; and ii) its relevant role due to its manifold reactivity.

Iron catalysis applied to organic synthesis has been of great interest, mainly because of its low cost, high abundancy, limited toxicity, and its rich oxidation chemistry.[204] During the last decade, C-H activation by iron complexes has attracted great interest in the scientific community,[105,205] which has been translated in the development of different chemical transformations like allylations,[206] alkylations,[207,208] arylations,[209] alkyne annulations,[190,210] alkynylidation,[211] and aminations,[212] amongst others.

Nevertheless, it is not an easy task to fully understand the mechanism of these catalytic reactions where Iron intermediates are involved due to all their possible oxidation states, spin states, and geometrical flexibility that Iron complexes can adopt. In addition, the instability and high reactivity of Iron complexes under standard conditions make it harder to isolate or characterize them. Even the use of standard spectroscopic techniques does not always work (*i.e.* NMR cannot be regularly used to follow the reaction due to the paramagnetic behavior of the spin state in several Iron complexes). Therefore, it becomes paramount to rely on more advanced spectroscopy, highly controlled conditions, and theoretical calculations to propose a feasible mechanism regarding the reactivity of organo-iron complexes.

Based on this, we were interested in using some of our template triaza macrocyclic ligands that have shown capabilities to stabilize reactive species of other first-row transition metals, such as Cu, Co, Ni.[213] The stabilizing power of this type of ligands to capture or isolate organo-iron intermediates could help to shed some light onto the mechanism of the C-H and C-X activation mediated by Iron species.

Then, during the experimental study of the reaction of triazamacrocylic ligand **1a** (one of our commonly used ligands) with an iron(0) source, $Fe(CO)_5$, it was found that two very different products were obtained depending on the conditions applied. If the complex reacted at 100 °C in acetonitrile (**Figure 7.1**), we obtained an aryl-Fe(II) complex with a CO formally inserted into the ligand backbone (forming an amide on the ligand). On the other hand, if milder thermal conditions (50 °C) and UV irradiation are applied (to promote the decoordination of CO from the Fe(0) complex), the expected aryl-Fe(II) product was isolated (a crystal structure confirmed the formation of the organo-iron complex). To our knowledge, a single report of carbonylation of tertiary amines has been reported very recently, although its mechanistic proposal cannot be applied to our system.[214] Taking all of the above into account, we endeavored to gain insight into the mechanism of this unexpected CO insertion by computational means. This chapter shows the computational results obtained so far. However, up to the moment of writing this thesis, the mechanistic proposal for this reaction remains unclear.

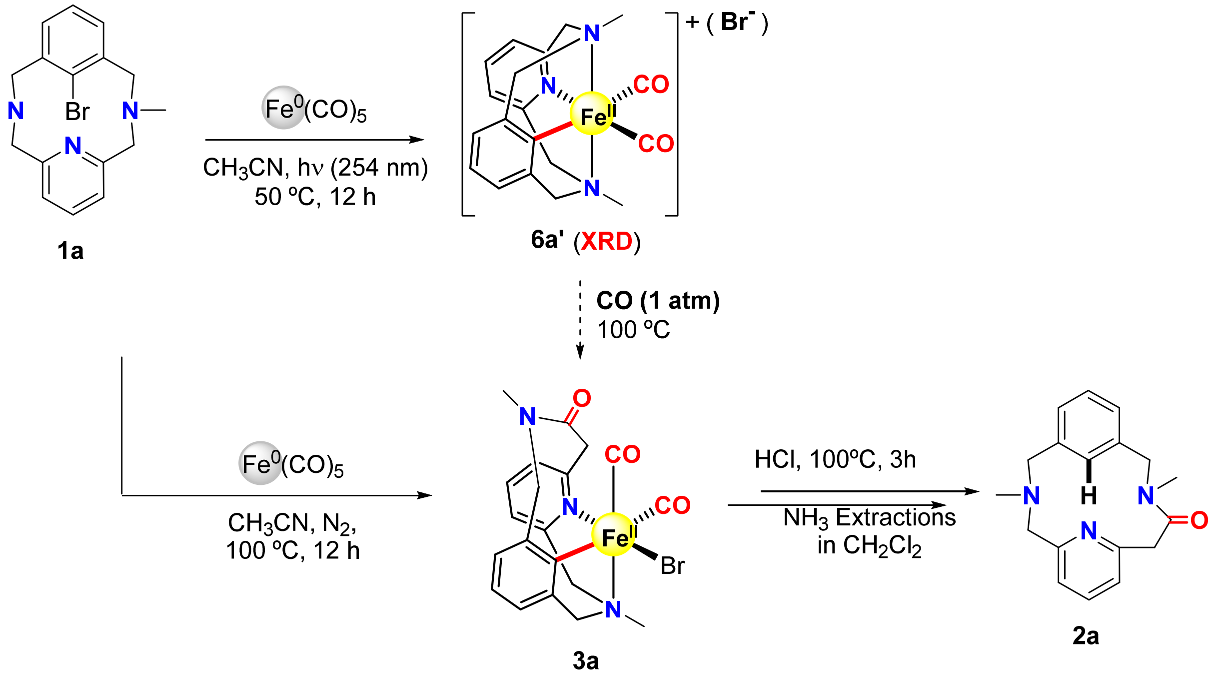

Figure 7.1 Experimental results of reacting the ligand **1a** with iron pentacarbonyl (Fe(CO)5).

7.1 Computational Details.

All DFT calculations were performed with the Gaussian 09 Revision E.01 program.[99] Geometry optimizations were carried out using the M06L functional[82] along with the def2-SVP basis set and its respective density fitting basis set (w06).[135,136] To check the reliability of the chosen functional, some calculations with B3LYP[79,81,138,139] were also performed, along with the def2-SVP basis set. Grimme's Dispersion model with Becke-Johnson damping function, GD3BJ,[137] was added to the B3LYP functional to improve accuracy. Solvation effects were included as a Polarizable Continuum using the SMD model.[94] Subsequently, we performed frequency calculations to each of the optimized structures to ensure that all local minima have only real frequencies and all transition states have only one imaginary frequency. To calculate the Gibbs energy (ΔG), *i.e.* to evaluate the entropic and enthalpic corrections, we used the python program Goodvibes (developed by Funes-Ardoiz and Paton).[97] The Gibbs energies were computed using the quasi-harmonic treatment (developed by Truhlar)[95] with a frequency scale factor of 1.0, a frequency cut-off value of 50 cm^{-1}, and a temperature value of 413.15 K (140 °C). The free energy correction associated with the change from a standard-state gas phase pressure of 1 atm to a standard-state gas phase concentration of the different reactants was also included in the final Gibbs energy differences. We also performed IRC calculations (using the LQA algorithm)[202,203] to verify that the transition states were connected with their respective reactants and products. Finally, single point energy calculations on the equilibrium geometries, including solvent and dispersion effects, were computed with the more flexible basis set Def2-TZPV[135,136] and their respective functionals (M06L or B3LYP).

Additionally, we used the program GRRM[100] (developed by Maeda and coworkers), in which we used the algorithms DS-AFIR (double sphere artificial force induced reaction) to find the shortest path that connects two structures, and SC-AFIR (single component artificial force induced reaction) to find global and semiglobal reaction path networks, in an attempt to find a suitable mechanism. Due to the high computational cost, we performed the calculations combining two levels of theory: **LV1** (M06L/Def2-SVP/W06 for C, H, N, O and M06L/SDD/W06 for Fe) for the inner part of the complex and **LV2** (M06L/Def2-SV for C and H) for the Methyl of the amino moieties and some of the aromatic carbons (see **Figure 7.2**). All AFIR calculations were performed in gas phase. Furthermore, the fragments selected to apply the SC-AFIR are marked by a blue asterisk in **Figure 7.2**. Different pair combinations of the four atoms were attempted. We used the program defaults and γ=200 and γ=500, where the γ parameter defines the upper limit of energy in which the path networks are searched (see chapter 2, AFIR section).

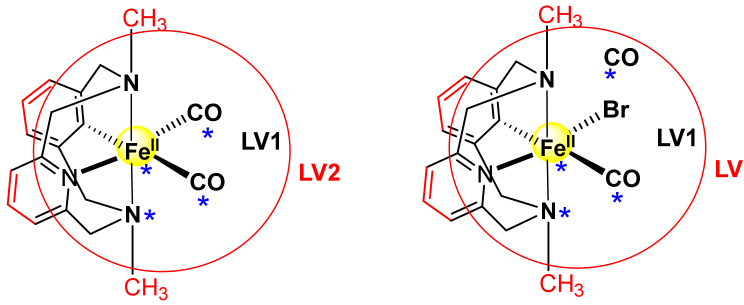

Figure 7.2 Scheme describing the sections where level of theory **LV1** (atoms in black) and **LV2** (atoms in red) are applied during the SC-AFIR calculation. The blue marks indicate the atoms that were selected to apply the single component force for different pair combinations of the blue marked atoms for each calculation.

7.2 Results and Discussions.

From the experimental results, it was evident that in the absence of light irradiation (λ=254 nm), the CO insertion was only effective over 100 °C. We were also able to identify an Iron(II) intermediate, **3a** (the intermediate complex product), by NMR spectroscopy. Since the relative position of the CO ligand and the Br^- ligand is not fully clear (or if the Bromide is acting as a counterion) with respect to the Iron, we assumed **3a-cis** as the right product complex as an initial approach (see **Figure 7.3 a**).

Unfortunately, it was not possible to isolate any other intermediate without changing the reaction conditions or the ligands. However, if we change the N-methyl moieties of the ligand for N-t-Bu, no CO-insertion product is observed; instead, the product of oxidative addition is obtained (see **Figure 7.3 b**). Moreover, if we irradiate the reaction with light (λ = 254 nm, the wavelength of CO dissociation), we also obtain an oxidative addition product **4a** with only one CO coordinated to the Iron(II) center, as ascertained by X-ray crystallography (see **Figure 7.3 c**).

(a) Reaction of **1a** with Fe(CO)$_5$ to yield **3.**

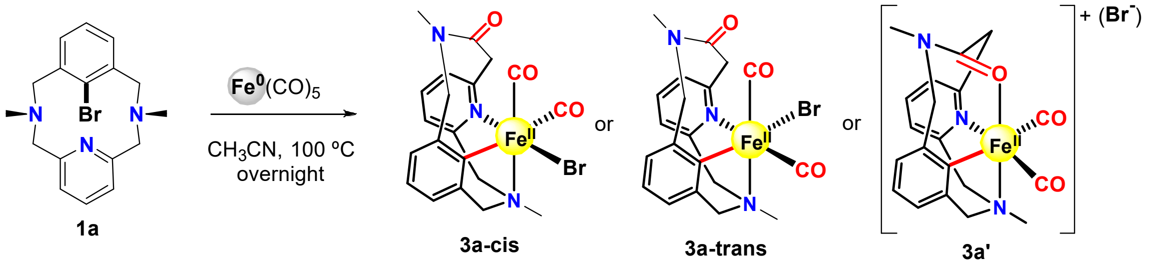

(b) Reaction of **1b** with Fe(CO)$_5$ to yield **4b**. Effect of changing the N-substituents.

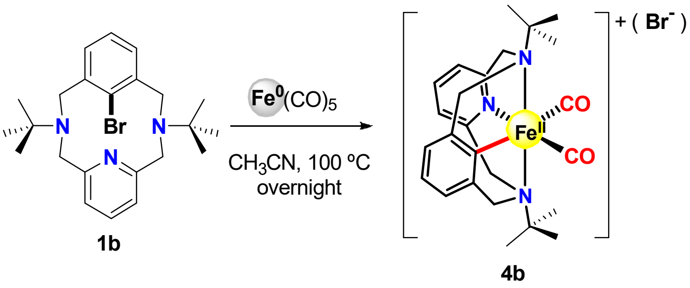

(c) Reaction of **1a** with Fe(CO)$_5$ under light exposure (254nm) to yield **4a.**

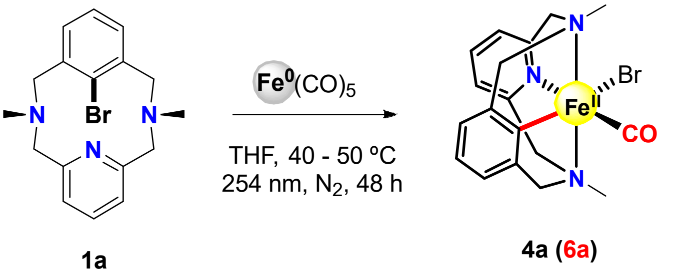

Figure 7.3 Experimental evidence regarding the reaction of study. **a)** Reactivity of **1a** under the normal conditions. **b)** Reactivity when changing the N-methyl substituents of the ligand. **c)** Reactivity when adding light exposure (254 nm).

Based on this experimental information and some assumptions, we proposed a mechanism (**Figure 7.4**) assuming that the decoordination of three CO ligands from the metal center and the simultaneous coordination of the organic ligand is favorable. Then, an oxidative addition occurs while another CO leaves the metallic center. After that, an attack from one of the amino groups to the carbonyl bonded to Iron(II) leads to some form of “rearrangement” to yield the amide moiety. Finally, the rebound of two CO ligands to the available coordination sites would furnish **3a.**

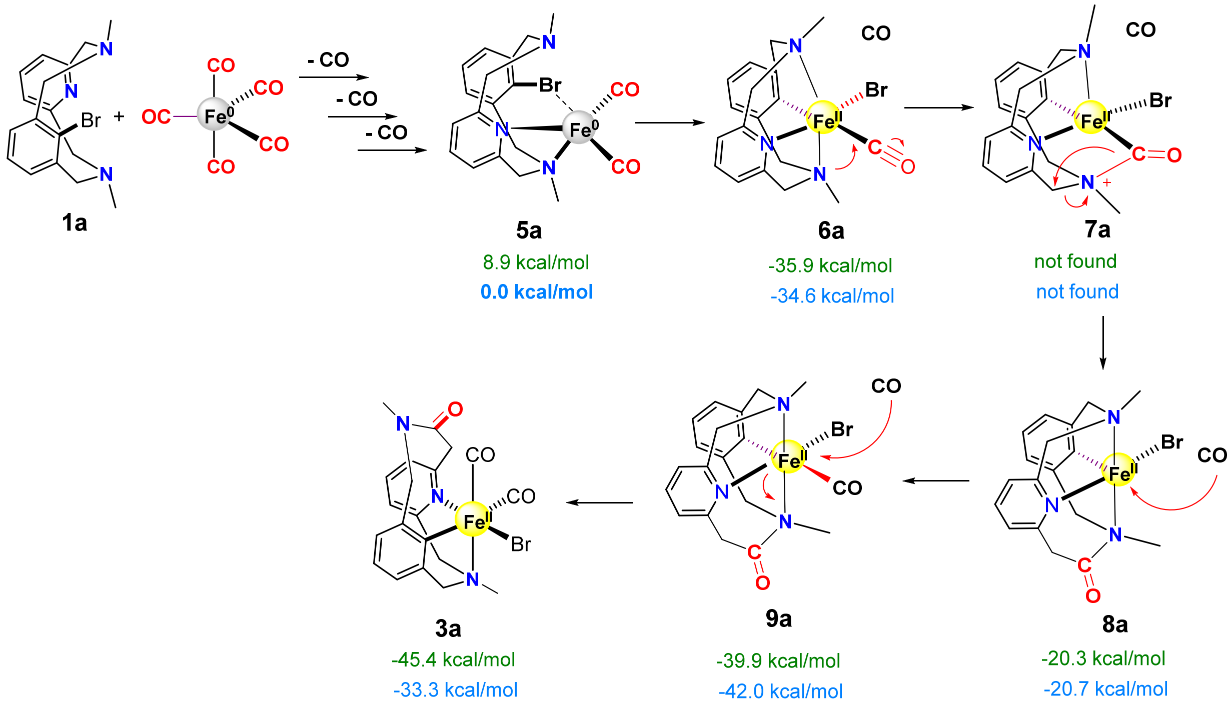

Figure 7.4 Initial proposed mechanism for the CO insertion. The relative Gibbs energy values are given for the singlet (in green) and the triplet (in blue) of each species, except for **7a** (which was not found). The point of reference is **5a** in triplet spin state. Energy values were calculated at the M06L/Def2-TZVP//M06L/Def2-SVP level of theory.

With this hypothesis in mind, we calculated the thermochemistry of this proposal using the energy of **5a** as a reference. All species could be optimized with the exception of species **7a** suggesting a concerted step from **6a** to **8a**. In addition, we explored the kinetics of the oxidative addition step from **5a** to **6a**. Although we were not able to optimize the transition state of this step, we found one transition state structure where the Br moiety is acting as a leaving group instead of a second CO (**TS**$_{5a\text{-}6a'}$ of **Figure 7.5**) yielding the product **6a′**. **TS**$_{5a\text{-}6a'}$ energy barrier is low (5.62 kcal/mol), however, **6a′** is higher in energy than its bromide relative **6a** (around 8 kcal/mol for both triplet and singlet species). We also tried to find a possible version of **7a** with another CO ligand instead of the bromide ligand (**7a′**) but it was not possible (the “bromideless” relative species **3a′** and **9a′** will be discussed later on in this chapter).

Since we did not find an intermediate or transition state connecting **6a** (**6a′**) with **8a** (**8a′**) by standard DFT calculations, we decided to use one of the automated reaction path search methods to systematically explore the possible paths of the reaction. Specifically, the method developed by Morokuma *et al.*: the AFIR (Artificial Force Induced Method) which is implemented in his software, GRRM.

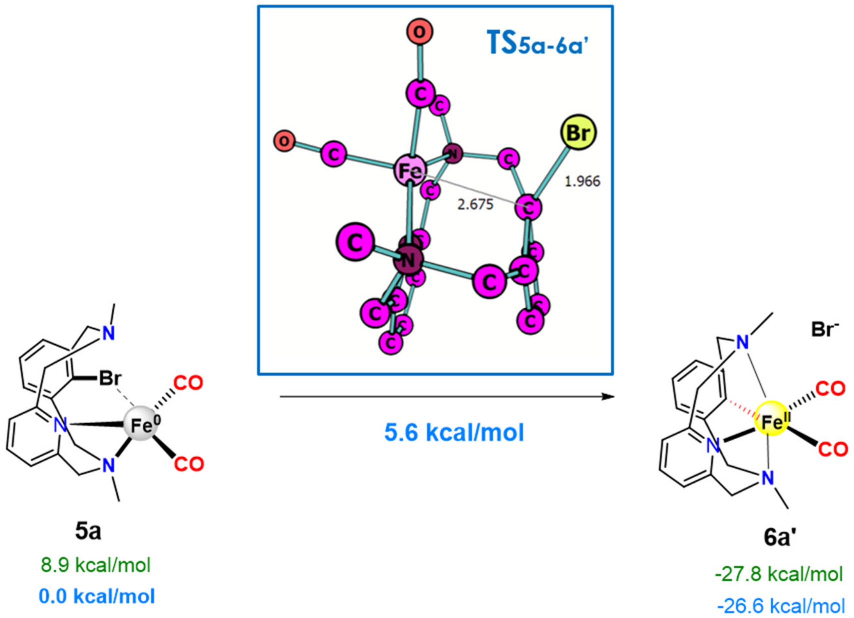

Figure 7.5 Oxidative addition of **5a** to yield **6a'** with its transition state **TS$_{5a\text{-}6a'}$**. The relative Gibbs energy values are given for the singlet (in green) and the triplet (in blue) of each species. The transition state was only found in triplet state. Energy values were calculated at the M06L/Def2-TZVP//M06L/Def2-SVP level of theory. Hydrogens are omitted for clarity.

7.2.1 The AFIR path

We decided to explore other plausible paths of the reaction with the AFIR to find the missing connection between **6a** and **8a** or a different mechanism that explains the CO insertion. First, we did several SC-AFIR calculations with the structures **5a** and **6a**/**6a'** as initial structures, selecting different fragments and γ parameters of 200 and 500; however, inconclusive results were obtained. Then, we turned to DS-AFIR calculations, using only **5a** as reactant and **9a** as product, yielding an approximated path connecting **5a** and **9a** with five intermediates, two transition states and one unavailable transition state (which was later obtained by the QST2 algorithm from Gaussian). These structures were re-optimized (with standard DFT calculations) to yield the energies and structures shown in **Figure 7.6**. The figure shows that the first transition state, **TS$_{5\text{-}10}$,** corresponds to the direct cleavage of the –H_2C-NMe bond, which explains the high Gibbs energy found. The transition states **TS$_{10\text{-}11}$** and **TS$_{12\text{-}9}$** are geometrical reorganizations of the ligands to allow the next step of the reaction. **TS$_{5\text{-}10}$** barrier is too high for the actual reaction conditions, therefore, this mechanism does not explain the reactivity of our system.

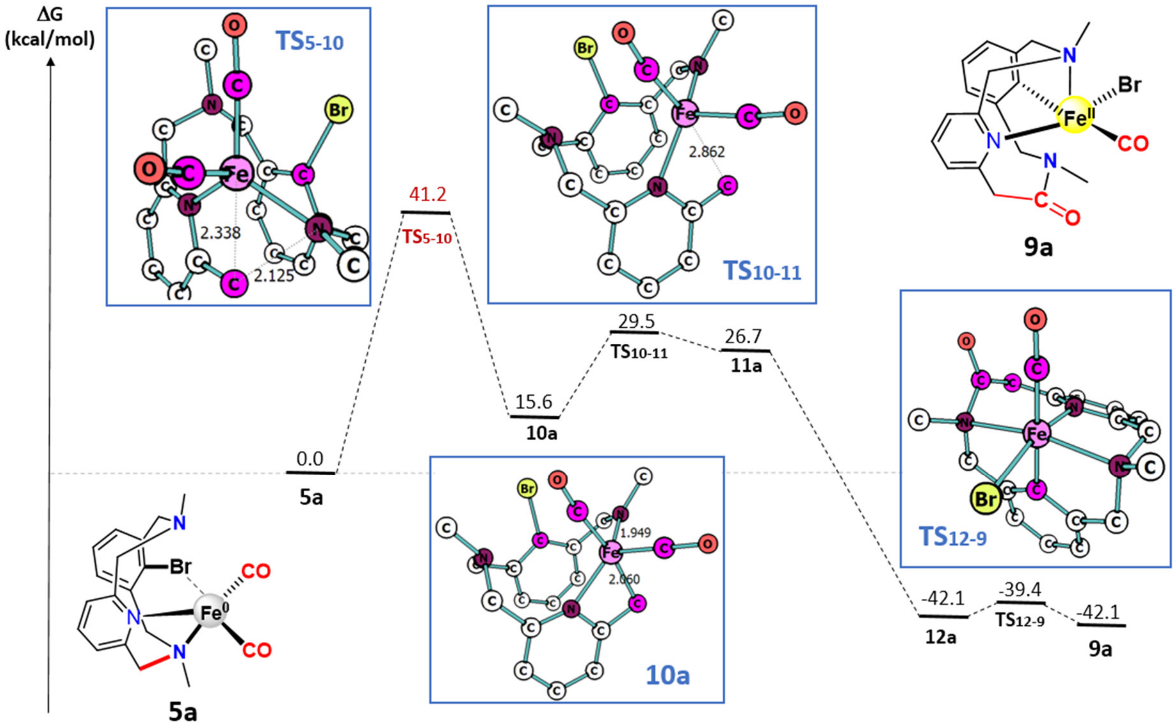

Figure 7.6 Gibbs energy profile from the resulted re-optimized path from the DS-AFIR calculation. The structures were re-optimized at M06L/Def2-TZVP//M06L/Def2-SVP level of theory. Hydrogen atoms have been omitted for clarity.

Although we wanted to explore more thoroughly different routes with the AFIR algorithms, we did not have enough computational power (or the time that these calculations require) for a more exhaustive exploration of our system bases on other hypotheses of reactants and products. Therefore, it would be more practical to analyze the rest of our hypotheses about our system just by standard DFT calculations. With this in mind, we moved to another plausible explanation for the reaction under study.

7.2.2 A different approach to the mechanism, the problem of the loss of CO ligands.

In our initial mechanistic proposal, we assumed that the loss of CO to form **5a**: i) happens before the oxidative addition; ii) is not the rate-determining step; iii) and it is energetically favored. However, after the previous results, we reconsidered these ideas and believed it reasonable to computationally evaluate the intermediates with different number of CO molecules decoordinated before the oxidative addition occurs. To achieve this goal, we assumed the reactants (Iron(0) pentacarbonyl and ligand **1a**) as a new reference point for the Gibbs energy profiles (**Table 7.1**). It is relevant to mention that we calculated both the triplet and the singlet spin states for all the species (the quintet spin state was ignored, since its energy was always too high compared to the other states in some complexes).

As **Table 7.1** shows, the formation of intermediate **5a** is not thermodynamically favored (34.1 kcal/mol). In general, the whole set of Iron(0) intermediates (4, 3, 2, 1, 0 CO ligands decoordinated) is endergonic, except for **6a**, which is slightly exergonic due to the fact that it is an Iron(II) species instead of an iron(0)-complex (it was not possible to obtain an iron(0) species with only one CO ligand). Moreover, we added the data of the product structures **3a** and **9a** in the table to compare to the others and, as we expected, they were both exergonic (**3a** being more so than **9a**).

Table 7.1 Electronic energy and Gibbs energy for the different intermediates that are formed by the loss of one CO ligand each time. The energy of products **3a** and **9a** are included for comparison.

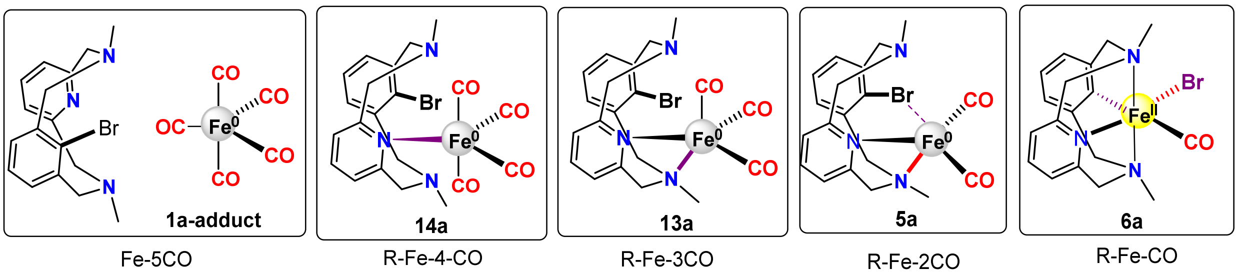

Entry	S^2	Electronic Energy (ΔE)	Gibbs Energy (ΔG)
1a + $FeCO_5$	Singlet	0.0	0.0
1a-adduct	Singlet	-5.0	16.0
1a-adduct	Triplet	22.3	37.8
14a + CO	Singlet	19.4	25.2
14a + CO	Triplet	26.8	29.4
13a + 2 CO	Singlet	36.9	29.5
13a + 2 CO	**Triplet**	**35.5**	**24.0**
5a + 3 CO	Singlet	65.2	43.0
5a+ 3 CO	Triplet	60.6	34.1
6a + 4 CO [a]	Singlet	35.9	-1.8
6a + 4 CO [a]	Triplet	39.6	-0.6
9a + 3 CO	Singlet	15.2	-5.8
9a + 3CO	Triplet	15.6	-7.9
3a + 2 CO	**Singlet**	**-6.1**	**-11.2**
3a + 2 CO	Triplet	8.3	0.8

[a] It is an Iron(II) complex not an Iron(0) complex.

From this data, we can conclude that it is likely that the intermediate **5a** cannot be part of the mechanism that describes the experiment because of its high-energy cost (34.2 kcal/mol) for the condition of the reaction (100 °C and molar concentration of ~ 0.04 M). Based on this, we wanted to explore a different mechanistic proposal similar to the one in **Figure 7.4** but reacting via the intermediate **13a** (with three CO ligands) instead of **5a** (with two CO ligands).

7.2.3 The mechanistic proposal based on **13a**.

The new proposal depicted in **Figure 7.7** is based on the assumption that under the reaction conditions the species **13a** is generated. This one is transformed into **15a-cis** (*vide infra*) by release of one of the CO ligand. Then, the attack of the side-amine to the closest CO ligand of the metal center should generate a structure analogous to **7a**. However, we found the structure **16a-cis**, which corresponds to the stepwise version of the CO insertion, *i.e.*, first the C-N bond is cleaved and then the new C-C bond is formed, leading to **9a**. Finally, by filling the ligand vacancy with another CO ligand, **3a** is formed.

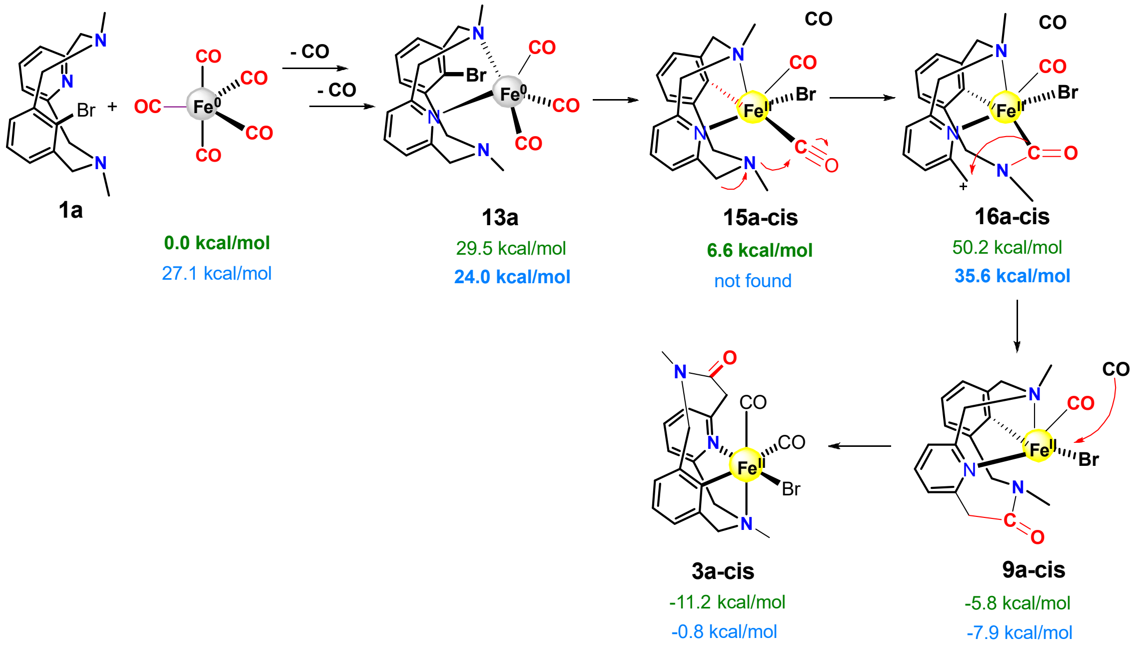

Figure 7.7 Another proposed mechanism for the CO insertion based on **13a**. The relative Gibbs energy values are given for the singlet (in green) and the triplet (in blue) of each species, except for **15a-cis** triplet (which was not found). Energy values were calculated at the M06L/Def2-TZVP//M06L/Def2-SVP level of theory. The reactants at infinite distance are defined as reference.

As we can see in **Figure 7.7**, the intermediate **16a-cis** (triplet) is high in energy (35.6 kcal/mol), making this intermediate incompatible with the experimental conditions. However, intermediates **15a-cis** and **16a-cis** have coordination isomers that might fit with the experimental evidence and the proposed mechanism (also **9a** and **3a**). In **Figure 7.8** we show the trans-coordinated isomers of the mentioned species and, as we can see, they are more stable than the cis-coordinated ones. Therefore, the trans effect of the aryl and CO ligands might have a relevant role during the oxidative addition (or, slightly after, the change from cis isomer to trans isomer should follow).

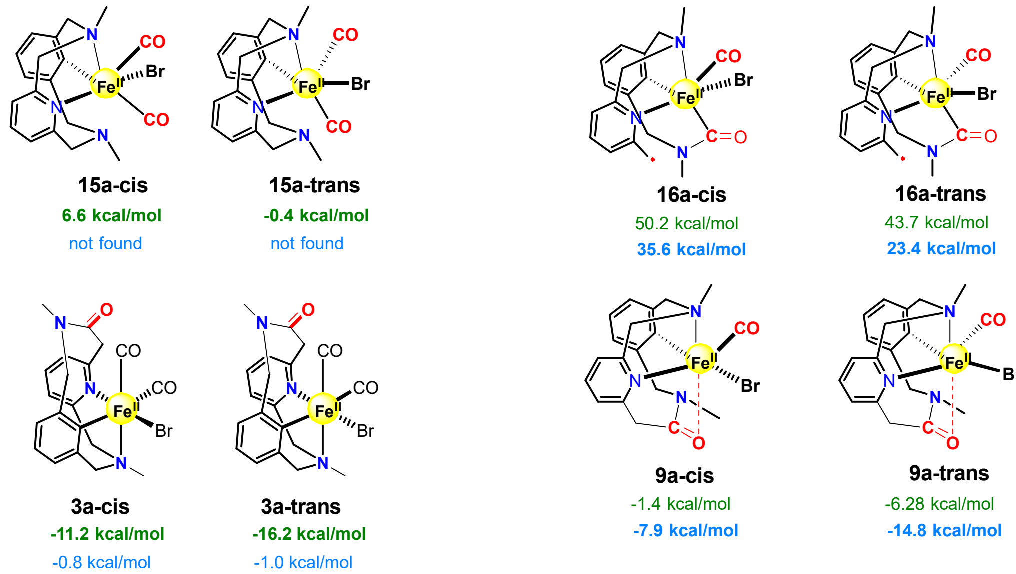

15a-cis
6.6 kcal/mol
not found

15a-trans
-0.4 kcal/mol
not found

16a-cis
50.2 kcal/mol
35.6 kcal/mol

16a-trans
43.7 kcal/mol
23.4 kcal/mol

3a-cis
-11.2 kcal/mol
-0.8 kcal/mol

3a-trans
-16.2 kcal/mol
-1.0 kcal/mol

9a-cis
-1.4 kcal/mol
-7.9 kcal/mol

9a-trans
-6.28 kcal/mol
-14.8 kcal/mol

Figure 7.8 Conformational isomers (cis and trans) of the intermediates **15a, 16a, 9a,** and **3a** (cis is defined as the Br ligand on the same side as the aryl ligand). The relative Gibbs energy values are given for the singlet (in green) and the triplet (in blue) of each species. Energy values were calculated at the M06L/Def2-TZVP//M06L/Def2-SVP level of theory. The reactants at infinite distance are defined as reference.

Inspired by this, we noticed that if we include the trans isomers instead of the cis-isomers into our mechanism, at least thermodynamically speaking, the mechanism would be more viable (**Figure 7.9**).

Once we had a reasonable thermodynamic mechanistic proposal we moved on to study the initial oxidative addition of the mechanism. Since the oxidation barrier for **13a** can occur in three different ways, we focused our attention on this subject. The possibilities studied were: 1) the oxidative addition occurs while the CO ligand leaves (concerted or stepwise); 2) the oxidative addition occurs while the Br$^-$ leaves the complex; 3) the oxidative addition occurs directly while a ligand vacancy is created by decoordinating the pyridine ligand. However, when we tried to calculate the first option, we were not able to find a suitable transition state for this transformation, neither for cis nor for trans isomers.

In the case of the second option (where the bromide acts as leaving group), we found a transition state ($\mathbf{TS}_{\mathbf{13a\text{-}15a'\text{-}add}}$, singlet) that corresponds to the oxidative addition while the Br$^-$ decoordinates from the iron(II) complex (similar to the transition state for the formation of **6a'**) to yield **15a'** (**Figure 7.10**). However, this transition state is energetically too demanding (45.9 kcal/mol) for the experimental conditions.

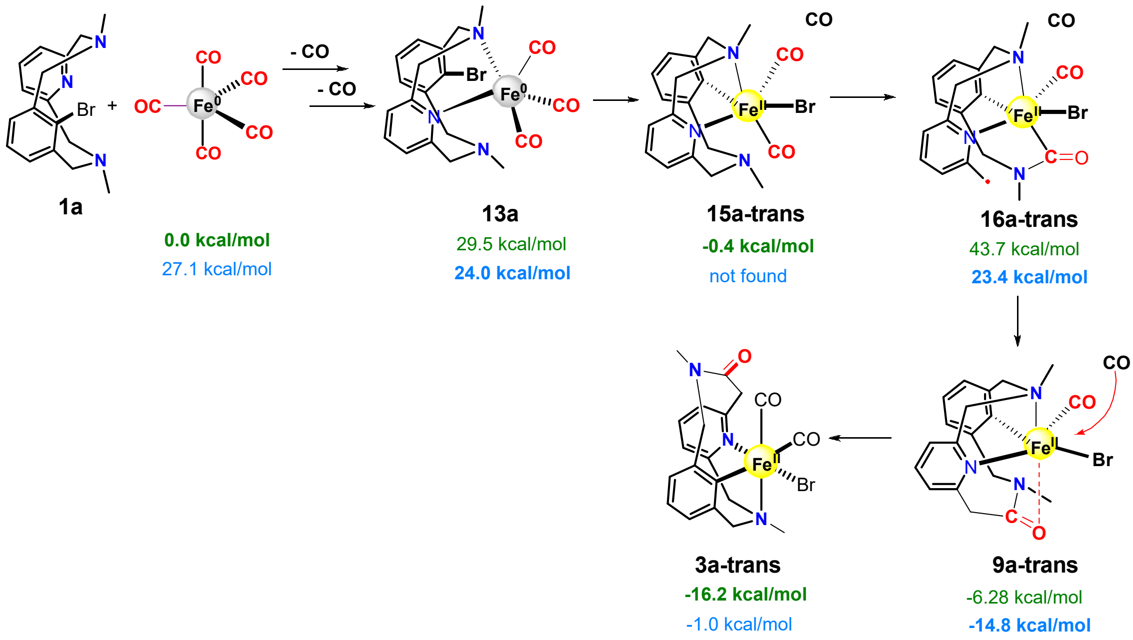

Figure 7.9 Mechanistic proposal for the CO insertion based on **13a** including the more-stable trans-coordination isomers. The relative Gibbs energy values are given for the singlet (in green) and the triplet (in blue) of each species, except for **15a-trans** triplet (which was not found). Energy values were calculated at the M06L/Def2-TZVP//M06L/Def2-SVP level of theory. The reactants at infinite distance are defined as reference.

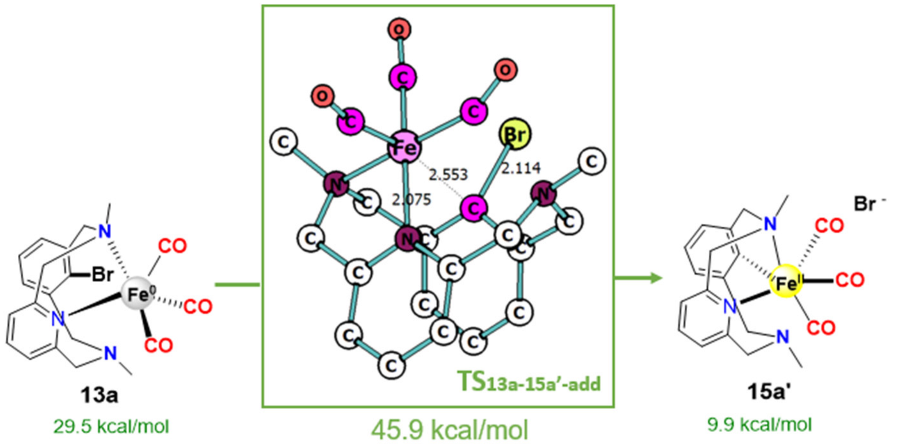

Figure 7.10 Oxidative addition of **13a** to yield **15a'** via **TS13a-15a'-add** (singlet). Energy values correspond to the Gibbs energies of the singlet species referenced to reactants at infinite distance (**1a** and iron(0) pentacarbonyl). Values are calculated at the M06L/Def2-TZVP//M06L/Def2-SVP level of theory.

Finally, in the case of the third oxidative addition (pyridine as the leaving ligand), we optimized a transition state, **TS$_{\mathbf{13aiso\text{-}17a}}$**, that corresponds to the transformation of an isomer of **13a** (**13a-iso**, where the iron is anchored to the organic ligand only by the pyridine) to yield the product **17a**, in which the pyridine ligand leaves the metal center during the oxidative addition (see **Figure 7.11**). Unfortunately, **TS$_{\mathbf{13aiso\text{-}17a}}$** was also high in energy.

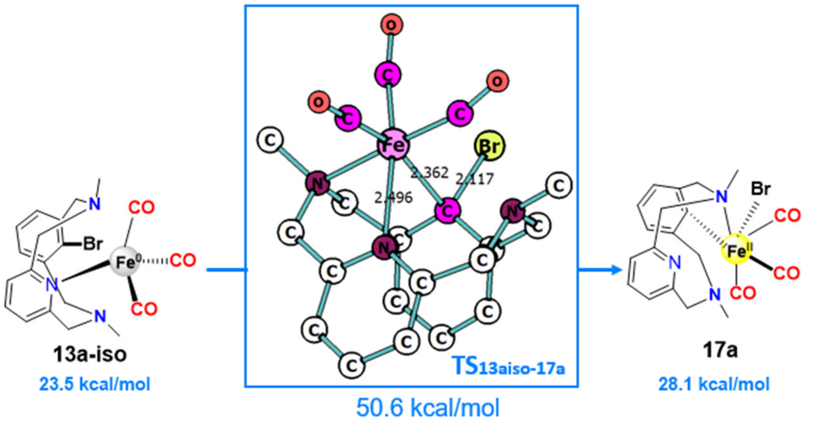

Figure 7.11 Transition state for the oxidative addition of **13a-iso** to yield the product **17a**. Energy values correspond to Gibbs energies of the triplet species referenced to reactants at infinite distance (**1a** and iron(0) pentacarbonyl). Values are calculated at the M06L/Def2-TZVP//M06L/Def2-SVP level of theory.

In summary, the mechanistic proposal based on **13a** seems viable, thermodynamically speaking (the intermediates have a reasonable Gibbs energy that can be achieved). However, the kinetic barriers for the oxidative addition step do not allow this mechanism to happen.

It is worth mentioning that we also calculated some of the relevant species at a different level of theory (B3LYP-GD3BJ/Def2TZVP// B3LYP-GD3BJ/Def2SVP). Although the results were slightly lower in energy, the patterns were the same: reasonable energy for the thermodynamic species but too high for the transition states (>37 kcal/mol).

Seeing that all of our previous proposals were not suitable for the experimental conditions, this showed us that the mechanism is far more challenging than we expected and that there is a missing piece in the puzzle (at the moment of writing this thesis). With this in mind, we consider it reasonable to dedicate the next subchapter to some other plausible mechanism that should be explored in future work.

7.2.4 Alternative mechanisms to study in future work and perspectives.

Since the previous proposals did not completely fit with the experimental conditions, the next logical alternative to study in the future could be the mechanism based on **14a** (the iron complex with 4 CO ligands instead of 3 or 2) to maintain a systematic analysis of the system (see **Figure 7.12A**). Then, as we were describing before, it would be necessary to study the thermochemistry of the different species possibly involved: the different isomers of **14a**, **18a** and **19a**, and also all the possible transition states regarding the oxidative addition (pyridine as leaving group or Br as leaving group or CO as leaving group).

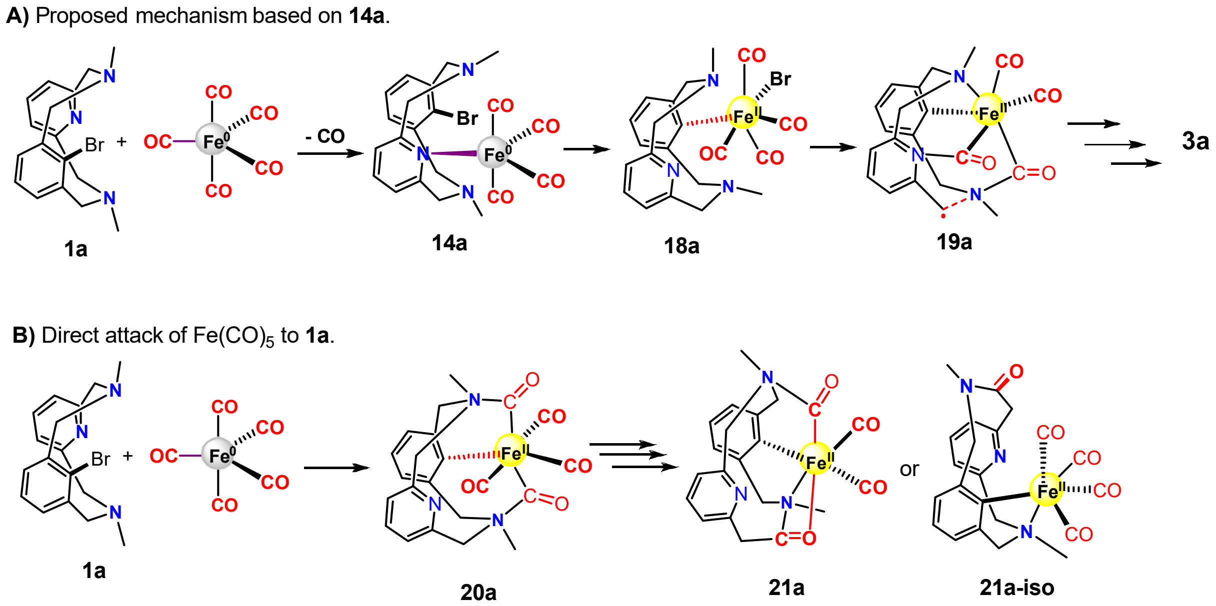

Figure 7.12 A) Proposed mechanism for the CO insertion based on **14a**. **B)** Proposed mechanism for the CO insertion starting by a direct oxidative addition.

To keep the systematic analysis, if the previous mechanism does not work, the next proposal should be a direct attack from the iron(0) pentacarbonyl to the aryl-Br bond to generate something similar to **20a** (**Figure 7.12 B**). As we suggested before for the previous mechanism, it would be prudent to explore several possible isomer of the species involved to generate **21a**.

In summary, we have explored different possible mechanisms for the CO insertion over the C-N side-bond of the ligand; however, none of our suggestions seem to show Gibbs energies low enough that correspond to the experimental conditions. We also checked some of the species in another level of theory (B3LYP-D3) but the energies were consistent with the values obtained with M06L. This makes the mechanism quite challenging, and it will require further investigation to arrive at any productive mechanism that can be related with the experimental data.

Chapter 8

Conclusions

In general, this thesis successfully highlights the relevant role of DFT calculations to reveal and comprehend key mechanistic details of the catalyses under study. The synergetic collaboration with the experimental researchers of the group allowed us to unveil the origin of unexpected intermediates and to propose new reaction mechanisms.

The conclusions are presented by chapters as follows:

"Mechanistic Aspects of the Aryl-Co(III) Masked-carbene Formation with Diazo Esters."

- The calculations for the mechanism clearly support that the reactivity of the well-defined Co(III) complex with the diazoacetates occurs via unexpected C-metalated aryl-Co(III) enolate (masked carbene) intermediate. Then, after a S_N2-like C-C bond formation and proto-demetalation steps, it yields the cyclic amide product.

- The beneficial experimental effect of the Lewis acid is explained by the calculations. The Li^+ cation is found to activate the carboxylate, triggering the C-O cleavage/C-C bond formation events. In a similar fashion, Na(OTf) (Na^+ source) and K(OTf) (K^+ source) also activate the carboxylate but with less strength (in descendant order, Li, Na, K, respectively).

- We explored computationally the reactivity of a whole family of C-metalated aryl-Co enolates with different acetate ligands, in which it is shown that the mechanism is favored by electron-poor precursors (diazo esters and carboxylate ligands). In the case of the nucleophilic aromatic moiety, electron-donating groups on the aromatic ring favor the S_N2-type step, which is the rate-determining step of the reaction. In addition, by using α-substituted diazo esters, an unprecedented intramolecular asynchronous S_N2-type pathway on a tertiary-Carbon is found.

"Insight into the Trifluoromethylation Mechanism of a Well-Defined Aryl-Ni(II) Species via Putative Ni(IV) or Ni(II) Intermediates."

- We initially explored two different pathways: i) the first proposal (A) was an oxidative-addition step followed by a reductive-elimination step (2-electron process); ii) the second proposal involved an initial single electron transfer (SET) followed by a direct radical $CF_3\cdot$ addition to the aryl group (1-electron process). Nevertheless, we finally found that the most favorable mechanism was a third mechanism that can be understood as a combination of both previous mechanisms.

- In the third mechanism the trifluoromethylation starts via a feasible single electron transfer step on the aryl-Ni(II) complex to afford a aryl-Ni(III)/$CF_3\cdot$ (first step, second mechanism), followed by a radical recombination that yields an aryl-Ni(IV)-CF_3 intermediate, which undergoes a fast reductive elimination to obtain the trifluoromethylated product (second step, first mechanism).

- The results from exploring a series of *p*-substituted aryl derivatives of Ni(II) show that the only way to considerably reduce the rate-determining step of the reaction is by using a dimethylamine substituent at the *para* position of the aryl moiety. Our calculations show that the dimethylamine group in the *p*-NMe-substituted aryl-Ni(III) complex plays a non-innocent role, significantly stabilizing the formation of the product.

"Nickel-Catalyzed Aromatic Homologation by Alkyne Insertion versus Alkyne Mono-annulation by Reductive Elimination."

- We were able to address the selectivity of arene C-F activation over the C-H activation with our calculations. According to our results, the transition state that corresponds to the C-F activation is 4.6 kcal/mol lower than the one for the C-H activation. In addition, the corresponding product of the C-F activation step is exergonic while the one that corresponds to the C-H activation is endergonic. Therefore, our computational results are aligned with the experimental evidence. Our calculations unraveled the crucial role of the Li^+ in assisting the removal of the fluoride anion.

- Our results also show that the chemodivergent behavior of the reaction, in which both the aromatic homologation product and the mono-annulation product are formed, is caused by the small energy difference (1.1 kcal/mol) between their transition states **TS-Z$_{3\text{-}4}$** (11.9kcal/mol) and **TS-Z$_{\text{RE-DPA}}$** (13.1 kcal/mol). This is in agreement with the higher yield obtained for the aromatic homologation product.

"On-ligand Amine-to-Amide Formation by CO Insertion on a Well-defined Iron(II) Complex."

- We explored computationally different mechanistic routes based on our chemical intuition that could explain the unexpected amide formation by CO insertion on the ligand scaffold. However, none shows Gibbs energy values that agree with the experimental conditions. Nevertheless, there are still some other routes that require further investigation and therefore this work is still a work in progress.

- We tried to explore in a more systematic manner possible mechanisms for the in-ligand side CO insertion with the aid of the program AFIR. We obtained a path that leads to the amide product starting from an Iron(0) species, using the algorithm DS-AFIR. However, the energy of the limiting step of this path was quite high for the experimental conditions.

References

[1] G. Rothenberg, *Catalysis: Concepts and Green Applications*, Wiley-VCH, **2017**.

[2] R. Schlögl, *ChemSusChem* **2010**, *3*, 209–222.

[3] W. Leitner, E. A. Quadrelli, R. Schlögl, *Green Chem.* **2017**, *19*, 2307–2308.

[4] P. Marion, B. Bernela, A. Piccirilli, B. Estrine, N. Patouillard, J. Guilbot, F. Jérôme, *Green Chem.* **2017**, *19*, 4973–4989.

[5] G. Centi, S. Perathoner, *Catal. Today* **2019**, DOI 10.1016/j.cattod.2019.04.003.

[6] R. A. Sheldon, I. W. C. E. Arends, U. Hanefeld, *Green Chemistry and Catalysis*, Wiley-VCH Verlag GmbH & Co. KGaA, Weinheim, Germany, **2007**.

[7] G. M. Cooper, *The Cell: A Molecular Approach*, Sinauer Associates, **2000**.

[8] IUPAC, "catalyst," DOI 10.1351/goldbook.C00876can be found under http://goldbook.iupac.org/C00876.html, **n.d.**

[9] G. Rothenberg, *Catalysis: Concepts and Green Applications*, Wiley-VCH Verlag GmbH & Co. KGaA, Weinheim, Germany, **2008**.

[10] "The Nobel Prize in Chemistry 2001," can be found under https://www.nobelprize.org/prizes/chemistry/2001/summary/, **n.d.**

[11] "The Nobel Prize in Chemistry 2005 - NobelPrize.org," can be found under https://www.nobelprize.org/prizes/chemistry/2005/summary/, **n.d.**

[12] "The Nobel Prize in Chemistry 2010 - NobelPrize.org," can be found under https://www.nobelprize.org/prizes/chemistry/2010/summary/, **n.d.**

[13] G. W. Parshall, *J. Mol. Catal.* **1978**, *4*, 243–270.

[14] J. Hagen, *Industrial Catalysis : A Practical Approach*, John Wiley & Sons, **2015**.

[15] F. Calderazzo, D. Carmona, M. Catellani, H. Brintzinger, M. G. Clerici, C. Dwyer, G. Fink, J. Fraile, A. Haynes, P. Howard, et al., *Metal-Catalysis in Industrial Organic Processes*, The Royal Society Of Chemistry, **2006**.

[16] B. Cornils, W. A. Herrmann, M. Beller, R. Paciello, *Applied Homogeneous Catalysis with Organometallic Compounds:A Comprehensive Handbook in Four Volumes*, **2017**.

[17] Q. L. Zhou, *Angew. Chemie - Int. Ed.* **2016**, *55*, 5352–5353.

[18] P. Chirik, R. Morris, *Acc. Chem. Res.* **2015**, *48*, 2495–2495.

[19] T. Sperger, I. A. Sanhueza, F. Schoenebeck, *Acc. Chem. Res.* **2016**, *49*, 1311–1319.

[20] G. J. Cheng, X. Zhang, L. W. Chung, L. Xu, Y. D. Wu, *J. Am. Chem. Soc.* **2015**, *137*, 1706–1725.

[21] K. D. Vogiatzis, M. V. Polynski, J. K. Kirkland, J. Townsend, A. Hashemi, C. Liu, E. A. Pidko, *Chem. Rev.* **2019**, *119*, 2453–2523.

[22] J. J. Spivey, K. S. Krishna, C. S. S. R. Kumar, K. M. Dooley, J. C. Flake, L. H. Haber, Y. Xu, M. J. Janik, S. B. Sinnott, Y. T. Cheng, et al., *J. Phys. Chem. C* **2014**, *118*, 20043–20069.

[23] A. J. Medford, A. Vojvodic, J. S. Hummelshøj, J. Voss, F. Abild-Pedersen, F. Studt, T. Bligaard, A. Nilsson, J. K. Nørskov, *J. Catal.* **2015**, *328*, 36–42.

[24] V. Van Speybroeck, K. Hemelsoet, L. Joos, M. Waroquier, R. G. Bell, C. R. A. Catlow, *Chem. Soc. Rev.* **2015**, *44*, 7044–7111.

[25] T. Sperger, I. A. Sanhueza, I. Kalvet, F. Schoenebeck, *Chem. Rev.* **2015**, *115*, 9532–9586.

[26] J. N. Harvey, F. Himo, F. Maseras, L. Perrin, *ACS Catal.* **2019**, *9*, 6803–6813.

[27] R. Noyori, J. P. Richmond, *Adv. Synth. Catal.* **2013**, *355*, 3–8.

[28] R. J. Meier, *Faraday Discuss.* **2003**, *124*, 405.

[29] A. J. Cohen, P. Mori-Sánchez, W. Yang, *Insights into Current Limitations of Density*

Functional Theory, **2008**.

[30] L. Goerigk, A. Hansen, C. Bauer, S. Ehrlich, A. Najibi, S. Grimme, *Phys. Chem. Chem. Phys.* **2017**, *19*, 32184–32215.

[31] H. Kruse, L. Goerigk, S. Grimme, *J. Org. Chem.* **2012**, *77*, 1–14.

[32] M. Garcia-Borràs, J. M. Luis, M. Swart, M. Solà, *Chem. - A Eur. J.* **2013**, *19*, 4468–4479.

[33] J. F. Hartwig, *Nature* **2008**, *455*, 314–322.

[34] S. L. Buchwald, *Acc. Chem. Res.* **2008**, *41*, 1439.

[35] J. Magano, J. R. Dunetz, *RSC Catal. Ser.* **2015**, *2015-Janua*, 697–778.

[36] B. Schlummer, U. Scholz, *Adv. Synth. Catal.* **2004**, *346*, 1599–1626.

[37] S. L. Buchwald, C. Mauger, G. Mignani, U. Scholz, *Adv. Synth. Catal.* **2006**, *348*, 23–39.

[38] M. Kosugi, M. Kameyama, T. Migita, *Chem. Lett.* **1983**, *12*, 927–928.

[39] Y. Kiso, K. Tamao, M. Kumada, *J. Organomet. Chem.* **1973**, *50*, C12–C14.

[40] N. Miyaura, K. Yamada, A. Suzuki, *Tetrahedron Lett.* **1979**, *20*, 3437–3440.

[41] D. Milstein, J. K. Stille, *J. Org. Chem.* **1979**, *44*, 1613–1618.

[42] A. O. King, N. Okukado, E. I. Negishi, *J. Chem. Soc. Chem. Commun.* **1977**, 683–684.

[43] Y. Hatanaka, T. Hiyama, *J. Org. Chem.* **1988**, *53*, 918–920.

[44] K. Sonogashira, *J. Organomet. Chem.* **2002**, *653*, 46–49.

[45] K. F. Heck, J. P. Nolley, *J. Org. Chem.* **1972**, *37*, 2320–2322.

[46] F. Paul, J. Patt, J. F. Hartwig, *J. Am. Chem. Soc.* **1994**, *116*, 5969–5970.

[47] A. S. Guram, S. L. Buchwald, *J. Am. Chem. Soc.* **1994**, *116*, 7901–7902.

[48] J. C. Hermann, Y. Chen, C. Wartchow, J. Menke, L. Gao, S. K. Gleason, N. E. Haynes, N. Scott, A. Petersen, S. Gabriel, et al., *ACS Med. Chem. Lett.* **2013**, *4*, 197–200.

[49] J. Kielhorn, C. Melber, D. Keller, I. Mangelsdorf, *Int. J. Hyg. Environ. Health* **2002**, *205*, 417–432.

[50] J. Wataha, in *Encycl. Met.* (Eds.: R.H. Kretsinger, V.N. Uversky, E.A. Permyakov), Springer New York, New York, NY, **2013**, pp. 1628–1635.

[51] B. M. Rosen, K. W. Quasdorf, D. A. Wilson, N. Zhang, A.-M. Resmerita, N. K. Garg, V. Percec, *Chem. Rev.* **2011**, *111*, 1346–1416.

[52] S. Z. Tasker, E. A. Standley, T. F. Jamison, *Nature* **2014**, *509*, 299–309.

[53] J. B. Diccianni, J. Katigbak, C. Hu, T. Diao, *J. Am. Chem. Soc.* **2019**, *141*, 1788–1796.

[54] H. Xu, C. T. Hu, X. Wang, T. Diao, *Organometallics* **2017**, *36*, 4099–4102.

[55] M. D. Leatherman, S. A. Svejda, L. K. Johnson, M. Brookhart, *J. Am. Chem. Soc.* **2003**, *125*, 3068–3081.

[56] H. Xu, P. B. White, C. Hu, T. Diao, *Angew. Chemie - Int. Ed.* **2017**, *56*, 1535–1538.

[57] L. Jin, H. Zhang, P. Li, J. R. Sowa, A. Lei, *J. Am. Chem. Soc.* **2009**, *131*, 9892–9893.

[58] J. B. Diccianni, T. Diao, *Trends Chem.* **2019**, *0*, DOI 10.1016/j.trechm.2019.08.004.

[59] J. Sommer, J. Bukala, *Acc. Chem. Res.* **1993**, *26*, 370–376.

[60] G. Dyker, *Angew. Chemie Int. Ed.* **1999**, *38*, 1698–1712.

[61] O. Planas, P. G. Chirila, C. J. Whiteoak, X. Ribas, *Current Mechanistic Understanding of Cobalt-Catalyzed C–H Functionalization*, Elsevier Inc., **2018**.

[62] P. B. Tchounwou, C. G. Yedjou, A. K. Patlolla, D. J. Sutton, *EXS* **2012**, *101*, 133–164.

[63] G. Song, X. Li, *Acc. Chem. Res.* **2015**, *48*, 1007–1020.

[64] G. Song, F. Wang, X. Li, *Chem. Soc. Rev.* **2012**, *41*, 3651–3678.

[65] K. Gao, N. Yoshikai, *Acc. Chem. Res.* **2014**, *47*, 1208–1219.

[66] A. Pribram-Jones, D. A. Gross, K. Burke, *Annu. Rev. Phys. Chem.* **2015**, *66*, 283–304.

[67] F. Jensen, *Introduction to Computational Chemistry*, John Wiley & Sons, Inc., USA, **2006**.

[68] Y. A. Wang, N. Govind, E. Carter, *Phys. Rev. B - Condens. Matter Mater. Phys.* **1999**, *60*, 16350–16358.

[69] S. S. Iyengar, M. Ernzerhof, S. N. Maximoff, G. E. Scuseria, *Phys. Rev. A - At. Mol. Opt. Phys.* **2001**, *63*, 8.

[70] W. Kohn, L. J. Sham, *Phys. Rev.* **1965**, *140*, A1133–A1138.

[71] R. Car, *Nat. Chem.* **2016**, *8*, 820–821.

[72] J. L. Bao, L. Gagliardi, D. G. Truhlar, *J. Phys. Chem. Lett.* **2018**, *9*, 2353–2358.

[73] O. A. Vydrov, G. E. Scuseria, *J. Chem. Phys.* **2005**, *122*, 184107.

[74] S. Grimme, *Wiley Interdiscip. Rev. Comput. Mol. Sci.* **2011**, *1*, 211–228.

[75] S. Grimme, S. Ehrlich, L. Goerigk, *J. Comput. Chem.* **2011**, *32*, 1456–1465.

[76] A. D. Becke, *Phys. Rev. A* **1988**, *38*, 3098–3100.

[77] J. P. Perdew, *Phys. Rev. B* **1986**, *33*, 8822–8824.

[78] A. D. Becke, *J. Chem. Phys.* **1993**, *98*, 5648–5652.

[79] C. Lee, W. Yang, R. G. Parr, *Phys. Rev. B* **1988**, *37*, 785–789.

[80] S. H. Vosko, L. Wilk, M. Nusair, *Can. J. Phys.* **1980**, *58*, 1200–1211.

[81] P. J. Stephens, F. J. Devlin, C. F. Chabalowski, M. J. Frisch, *J. Phys. Chem.* **1994**, *98*, 11623–11627.

[82] Y. Zhao, D. G. Truhlar, *J. Chem. Phys.* **2006**, *125*, 194101.

[83] D. C. Young, in *Comput. Chem. A Pract. Guid. Appl. Tech. to Real World Probl.*, John Wiley & Sons, Inc., New York, USA, **2001**, pp. 78–91.

[84] D. Moran, A. C. Simmonett, F. E. Leach, W. D. Allen, P. V. R. Schleyer, H. F. Schaefer, *J. Am. Chem. Soc.* **2006**, *128*, 9342–9343.

[85] A. J. C. Varandas, *J. Phys. Chem. A* **2008**, *112*, 1841–1850.

[86] A. J. C. Varandas, *J. Chem. Phys.* **2007**, *126*, DOI 10.1063/1.2741259.

[87] D. W. Schwenke, *J. Chem. Phys.* **2005**, *122*, DOI 10.1063/1.1824880.

[88] D. C. Young, *Computational Chemistry: A Practical Guide for Applying Techniques to Real World Problems*, John Wiley & Sons, Inc., New York, USA, **2001**.

[89] P. Morgante, R. Peverati, **2019**, DOI 10.26434/CHEMRXIV.10187756.V1.

[90] F. Jensen, *J. Chem. Phys.* **2001**, *115*, 9113–9125.

[91] D. G. Truhlar, *J. Chem. Educ.* **2019**, *96*, 1671–1675.

[92] B. Mennucci, R. Cammi, *Continuum Solvation Models in Chemical Physics: From Theory to Applications*, Chichester, UK, **2007**.

[93] J. Tomasi, B. Mennucci, R. Cammi, *Chem. Rev.* **2005**, *105*, 2999–3093.

[94] A. V. Marenich, C. J. Cramer, D. G. Truhlar, *J. Phys. Chem. B* **2009**, *113*, 6378–6396.

[95] R. F. Ribeiro, A. V. Marenich, C. J. Cramer, D. G. Truhlar, *J. Phys. Chem. B* **2011**, *115*, 14556–14562.

[96] S. Grimme, *Chem. - A Eur. J.* **2012**, *18*, 9955–9964.

[97] R. S. Funes-Ardoiz, I., Paton, **2016**, DOI http://doi.org/10.5281/zenodo.595246.

[98] R. a. Marcus, *J. Chem. Phys.* **1956**, *24*, 966.

[99] and D. J. F. M. J. Frisch, G. W. Trucks, H. B. Schlegel, G. E. Scuseria, M. A. Robb, J. R. Cheeseman, G. Scalmani, V. Barone, G. A. Petersson, H. Nakatsuji, X. Li, M. Caricato, A. Marenich, J. Bloino, B. G. Janesko, R. Gomperts, B. Mennucci, H. P. Hratchian, J. V. Ort, **2016**.

[100] S. Maeda, Y. Harabuchi, M. Takagi, K. Saita, K. Suzuki, T. Ichino, Y. Sumiya, K.

Sugiyama, Y. Ono, *J. Comput. Chem.* **2017**, *39*, 233–250.
[101] S. Maeda, “AFIR Mannual ONLINE,” can be found under https://afir.sci.hokudai.ac.jp/documents/manual/toc, **2017**.
[102] T. Newhouse, P. S. Baran, *Angew. Chemie - Int. Ed.* **2011**, *50*, 3362–3374.
[103] L. McMurray, F. O'Hara, M. J. Gaunt, *Chem. Soc. Rev.* **2011**, *40*, 1885–1898.
[104] P. Thansandote, M. Lautens, *Chem. - A Eur. J.* **2009**, *15*, 5874–5883.
[105] P. Gandeepan, T. Müller, D. Zell, G. Cera, S. Warratz, L. Ackermann, *Chem. Rev.* **2018**, acs.chemrev.8b00507.
[106] W. I. Dzik, X. Xu, X. P. Zhang, J. N. H. Reek, B. De Bruin, *J. Am. Chem. Soc.* **2010**, *132*, 10891–10902.
[107] J. E. Zweig, D. E. Kim, T. R. Newhouse, *Chem. Rev.* **2017**, *117*, 11680–11752.
[108] M. Moselage, J. Li, L. Ackermann, *ACS Catal.* **2016**, *6*, 498–525.
[109] S. Wang, S. Y. Chen, X. Q. Yu, *Chem. Commun.* **2017**, *53*, 3165–3180.
[110] P. G. Chirila, C. J. Whiteoak, *Dalt. Trans.* **2017**, *46*, 9721–9739.
[111] T. Yoshino, S. Matsunaga, *Adv. Synth. Catal.* **2017**, *359*, 1245–1262.
[112] D. Wei, X. Zhu, J. L. Niu, M. P. Song, *ChemCatChem* **2016**, *8*, 1242–1263.
[113] Y. Kommagalla, N. Chatani, *Coord. Chem. Rev.* **2017**, *350*, 117–135.
[114] T. Avilés, A. Dinis, M. J. Calhorda, P. Pinto, V. Félix, M. G. B. Drew, *J. Organomet. Chem.* **2001**, *625*, 186–194.
[115] K. Kanamori, W. E. Broderick, R. F. Jordan, R. D. Willett, J. I. Legg, *J. Am. Chem. Soc.* **1986**, *108*, 7122–7124.
[116] X. Yu, K. Chen, S. Guo, P. Shi, C. Song, J. Zhu, *Org. Lett.* **2017**, *19*, 5348–5351.
[117] S. Maity, R. Kancherla, U. Dhawa, E. Hoque, S. Pimparkar, D. Maiti, *ACS Catal.* **2016**, *6*, 5493–5499.
[118] Y. Baek, S. Kim, B. Jeon, P. H. Lee, *Org. Lett.* **2016**, *18*, 104–107.
[119] K. Ramakrishna, C. Sivasankar, *European J. Org. Chem.* **2017**, *2017*, 4035–4043.
[120] B. G. Das, A. Chirila, M. Tromp, J. N. H. Reek, B. de Bruin, *J. Am. Chem. Soc.* **2016**, jacs.6b05434.
[121] Y. Wang, X. Wen, X. Cui, L. Wojtas, X. P. Zhang, *J. Am. Chem. Soc.* **2017**, *139*, 1049–1052.
[122] T. Ikeno, I. Iwakura, T. Yamada, *J. Am. Chem. Soc.* **2002**, *124*, 15152–15153.
[123] H. Lu, W. I. Dzik, X. Xu, L. Wojtas, B. De Bruin, X. P. Zhang, *J. Am. Chem. Soc.* **2011**, *133*, 8518–8521.
[124] S. Roy, S. K. Das, B. Chattopadhyay, *Angew. Chemie - Int. Ed.* **2018**, *57*, 2238–2243.
[125] C. Te Grotenhuis, B. G. Das, P. F. Kuijpers, W. Hageman, M. Trouwborst, B. De Bruin, *Chem. Sci.* **2017**, *8*, 8221–8230.
[126] C. te Grotenhuis, N. van den Heuvel, J. I. van der Vlugt, B. de Bruin, *Angew. Chemie - Int. Ed.* **2018**, *57*, 140–145.
[127] S. Y. Yan, P. X. Ling, B. F. Shi, *Adv. Synth. Catal.* **2017**, *359*, 2912–2917.
[128] X. G. Liu, S. S. Zhang, J. Q. Wu, Q. Li, H. Wang, *Tetrahedron Lett.* **2015**, *56*, 4093–4095.
[129] J. Li, M. Tang, L. Zang, X. Zhang, Z. Zhang, L. Ackermann, *Org. Lett.* **2016**, *18*, 2742–2745.
[130] D. Zhao, J. H. Kim, L. Stegemann, C. A. Strassert, F. Glorius, *Angew. Chem. Int. Ed.* **2015**, *54*, 1–5.
[131] J. H. Kim, S. Greßies, F. Glorius, *Angew. Chemie - Int. Ed.* **2016**, *55*, 5577–5581.

[132] S. Qu, C. J. Cramer, *J. Org. Chem.* **2017**, acs.joc.6b02962.

[133] F. Hu, Y. Xia, C. Ma, Y. Zhang, J. Wang, *Chem. Commun.* **2015**, *51*, 7986–7995.

[134] O. Planas, C. J. Whiteoak, V. Martin-Diaconescu, I. Gamba, J. M. Luis, T. Parella, A. Company, X. Ribas, *J. Am. Chem. Soc.* **2016**, *138*, 14388–14397.

[135] F. Weigend, R. Ahlrichs, *Phys. Chem. Chem. Phys.* **2005**, *7*, 3297.

[136] F. Weigend, *Phys. Chem. Chem. Phys.* **2006**, *8*, 1057.

[137] S. Grimme, J. Antony, S. Ehrlich, H. Krieg, *J. Chem. Phys.* **2010**, *132*, 154104.

[138] A. D. Becke, *J. Chem. Phys.* **1993**, *98*, 1372.

[139] S. H. Vosko, L. Wilk, M. Nusair, *Can. J. Phys.* **1980**, *58*, 1200–1211.

[140] T. Furuya, A. S. Kamlet, T. Ritter, *Nature* **2011**, *473*, 470–477.

[141] S. S. Barata-Vallejo, B. Lantano, A. Postigo, *Chem. - A Eur. J.* **2014**, *20*, 16806–16829.

[142] E. J. Cho, T. D. Senecal, T. Kinzel, Y. Zhang, D. A. Watson, S. L. Buchwald, *Science (80-.).* **2010**, *328*, 1679–1681.

[143] N. D. Ball, J. B. Gary, Y. Ye, M. S. Sanford, *J. Am. Chem. Soc.* **2011**, *133*, 7577–7584.

[144] A. Maleckis, M. S. Sanford, *Organometallics* **2014**, *33*, 2653–2660.

[145] R. Jana, T. P. Pathak, M. S. Sigman, *Chem. Rev.* **2011**, *111*, 1417–1492.

[146] V. P. Ananikov, *ACS Catal.* **2015**, *5*, 1964–1971.

[147] C. M. Lavoie, P. M. Macqueen, N. L. Rotta-Loria, R. S. Sawatzky, A. Borzenko, A. J. Chisholm, B. K. V. Hargreaves, R. McDonald, M. J. Ferguson, M. Stradiotto, *Nat. Commun.* **2016**, *7*, 11073.

[148] D. A. Everson, D. J. Weix, *J. Org. Chem.* **2014**, *79*, 4793–4798.

[149] T. T. Tsou, J. K. Kochi, *J. Am. Chem. Soc.* **1979**, *101*, 6319–6332.

[150] H. Q. Do, E. R. R. Chandrashekar, G. C. Fu, *J. Am. Chem. Soc.* **2013**, *135*, 16288–16291.

[151] J. Cornella, J. T. Edwards, T. Qin, S. Kawamura, J. Wang, C. M. Pan, R. Gianatassio, M. Schmidt, M. D. Eastgate, P. S. Baran, *J. Am. Chem. Soc.* **2016**, *138*, 2174–2177.

[152] T. Qin, J. Cornella, C. Li, L. R. Malins, J. T. Edwards, S. Kawamura, B. D. Maxwell, M. D. Eastgate, P. S. Baran, *Science (80-.).* **2016**, *352*, 801–805.

[153] N. M. Camasso, M. S. Sanford, *Science (80-.).* **2015**, *347*, 1218–1220.

[154] J. W. Schultz, K. Fuchigami, B. Zheng, N. P. Rath, L. M. Mirica, *J. Am. Chem. Soc.* **2016**, *138*, 12928–12934.

[155] Y. Aihara, N. Chatani, *J. Am. Chem. Soc.* **2014**, *136*, 898–901.

[156] Y. Aihara, N. Chatani, *J. Am. Chem. Soc.* **2013**, *135*, 5308–5311.

[157] X. Wu, Y. Zhao, H. Ge, *J. Am. Chem. Soc.* **2014**, *136*, 1789–1792.

[158] G. E. Martinez, C. Ocampo, Y. J. Park, A. R. Fout, *J. Am. Chem. Soc.* **2016**, *138*, 4290–4293.

[159] E. A. Meucci, A. Ariafard, A. J. Canty, J. W. Kampf, M. S. Sanford, *J. Am. Chem. Soc.* **2019**, *141*, 13261–13267.

[160] J. R. Bour, N. M. Camasso, M. S. Sanford, *J. Am. Chem. Soc.* **2015**, *137*, 8034–8037.

[161] A. Schäfer, H. Horn, R. Ahlrichs, *J. Chem. Phys.* **1992**, *97*, 2571–2577.

[162] A. Schäfer, C. Huber, R. Ahlrichs, *J. Chem. Phys.* **1994**, *100*, 5829.

[163] R. A. Kendall, T. H. Dunning, R. J. Harrison, *J. Chem. Phys.* **1992**, *96*, 6796–6806.

[164] E. R. Davidson, *Chem. Phys. Lett.* **1996**, *260*, 514–518.

[165] M. Rovira, S. Roldán-Gómez, V. Martin-Diaconescu, C. J. Whiteoak, A. Company, J. M. Luis, X. Ribas, *Chem. - A Eur. J.* **2017**, *23*, 11662–11668.

[166] S. Swallow, in *Prog. Med. Chem.*, John Wiley & Sons, Ltd, **2015**, pp. 65–133.

[167] K. Müller, C. Faeh, F. Diederich, *Science (80-.).* **2007**, *317*, 1881–1886.

[168] J. Wang, M. Sánchez-Roselló, J. L. Aceña, C. Del Pozo, A. E. Sorochinsky, S. Fustero, V. A. Soloshonok, H. Liu, *Chem. Rev.* **2014**, *114*, 2432–2506.

[169] S. Purser, P. R. Moore, S. Swallow, V. Gouverneur, *Chem. Soc. Rev.* **2008**, *37*, 1–200.

[170] A. D. Sun, J. A. Love, *Dalt. Trans.* **2010**, *39*, 10362–10374.

[171] H. Amii, K. Uneyama, *ChemInform* **2009**, *40*, 2119–2183.

[172] T. Ahrens, J. Kohlmann, M. Ahrens, T. Braun, *Chem. Rev.* **2015**, *115*, 931–972.

[173] B. Zheng, F. Tang, J. Luo, J. W. Schultz, N. P. Rath, L. M. Mirica, *J. Am. Chem. Soc.* **2014**, *136*, 6499–6504.

[174] L. Ackermann, R. Born, J. H. Spatz, D. Meyer, *Angew. Chemie - Int. Ed.* **2005**, *44*, 7216–7219.

[175] N. Yoshikai, H. Mashima, E. Nakamura, *J. Am. Chem. Soc.* **2005**, *127*, 17978–17979.

[176] J. R. Wang, K. Manabe, *Org. Lett.* **2009**, *11*, 741–744.

[177] N. Yoshikai, H. Matsuda, E. Nakamura, *J. Am. Chem. Soc.* **2009**, *131*, 9590–9599.

[178] L. Ackermann, C. Wechsler, A. R. Kapdi, A. Althammer, *Synlett* **2010**, *2010*, 294–298.

[179] Y. Nakamura, N. Yoshikai, L. Ilies, E. Nakamura, *Org. Lett.* **2012**, *14*, 3316–3319.

[180] W. J. Guo, Z. X. Wang, *J. Org. Chem.* **2013**, *78*, 1054–1061.

[181] T. Schaub, M. Backes, U. Radius, *J. Am. Chem. Soc.* **2006**, *128*, 15964–15965.

[182] A. D. Sun, J. A. Love, *Org. Lett.* **2011**, *13*, 2750–2753.

[183] M. Tobisu, T. Xu, T. Shimasaki, N. Chatani, *J. Am. Chem. Soc.* **2011**, *133*, 19505–19511.

[184] J. Zhou, J. H. J. Berthel, M. W. Kuntze-Fechner, A. Friedrich, T. B. Marder, U. Radius, *J. Org. Chem.* **2016**, *81*, 5789–5794.

[185] Y. A. Ho, M. Leiendecker, X. Liu, C. Wang, N. Alandini, M. Rueping, *Org. Lett.* **2018**, *20*, 5644–5647.

[186] D. Yu, C. S. Wang, C. Yao, Q. Shen, L. Lu, *Org. Lett.* **2014**, *16*, 5544–5547.

[187] N. Guimond, C. Gouliaras, K. Fagnou, *J. Am. Chem. Soc.* **2010**, *132*, 6908–6909.

[188] L. Ackermann, A. V. Lygin, N. Hofmann, *Angew. Chemie - Int. Ed.* **2011**, *50*, 6379–6382.

[189] H. Shiota, Y. Ano, Y. Aihara, Y. Fukumoto, N. Chatani, *J. Am. Chem. Soc.* **2011**, *133*, 14952–14955.

[190] G. Cera, T. Haven, L. Ackermann, *Chem. Commun.* **2017**, *53*, 6460–6463.

[191] C. Tian, L. Massignan, T. H. Meyer, L. Ackermann, *Angew. Chemie - Int. Ed.* **2018**, *57*, 2383–2387.

[192] W. Song, L. Ackermann, *Chem. Commun.* **2013**, *49*, 6638–6640.

[193] D. R. Stuart, M. Bertrand-Laperle, K. M. N. Burgess, K. Fagnou, *J. Am. Chem. Soc.* **2008**, *130*, 16474–16475.

[194] L. Ackermann, *Acc. Chem. Res.* **2014**, *47*, 281–295.

[195] N. Jiao, Z. Shi, C. Zhang, S. Li, D. Pan, S. Ding, Y. Cui, *Angew. Chemie - Int. Ed.* **2009**, *48*, 4572–4576.

[196] J. Le Bras, J. Muzart, *Synth.* **2014**, *46*, 1555–1572.

[197] T. Fukutani, K. Hirano, T. Satoh, M. Miura, *J. Org. Chem.* **2011**, *76*, 2867–2874.

[198] M. V. Pham, N. Cramer, *Angew. Chemie - Int. Ed.* **2014**, *53*, 3484–3487.

[199] Á. M. Martínez, J. Echavarren, I. Alonso, N. Rodríguez, R. Gómez Arrayás, J. C. Carretero, *Chem. Sci.* **2015**, *6*, 5802–5814.

[200] L. C. Misal Castro, A. Obata, Y. Aihara, N. Chatani, *Chem. - A Eur. J.* **2016**, *22*, 1362–1367.

[201] Z. He, Y. Huang, *ACS Catal.* **2016**, *6*, 7814–7823.

[202] M. Page, J. W. McIver, *J. Chem. Phys.* **1988**, *88*, 922–935.

[203] M. Page, C. Doubleday, J. W. McIver, *J. Chem. Phys.* **1990**, *93*, 5634–5642.

[204] I. Bauer, H.-J. Knölker, *Chem. Rev.* **2015**, *115*, 3170–3387.

[205] R. Shang, L. Ilies, E. Nakamura, *Chem. Rev.* **2017**, *117*, 9086–9139.

[206] G. Cera, T. Haven, L. Ackermann, *Angew. Chemie - Int. Ed.* **2016**, *55*, 1484–1488.

[207] E. R. Fruchey, B. M. Monks, S. P. Cook, *J. Am. Chem. Soc.* **2014**, *136*, 13130–13133.

[208] L. Ilies, T. Matsubara, S. Ichikawa, S. Asako, E. Nakamura, *J. Am. Chem. Soc.* **2014**, *136*, 13126–13129.

[209] Q. Gu, H. H. Al Mamari, K. Graczyk, E. Diers, L. Ackermann, *Angew. Chemie - Int. Ed.* **2014**, *53*, 3868–3871.

[210] J. Mo, T. Müller, J. C. A. Oliveira, L. Ackermann, *Angew. Chemie - Int. Ed.* **2018**, *57*, 7719–7723.

[211] G. Cera, T. Haven, L. Ackermann, *Chem. - A Eur. J.* **2017**, *23*, 3577–3582.

[212] T. Matsubara, S. Asako, L. Ilies, E. Nakamura, *J. Am. Chem. Soc.* **2014**, *136*, 646–649.

[213] X. Ribas, M. Devillard, *Chem. - A Eur. J.* **2018**, *24*, 1222–1230.

[214] T. Nasr Allah, S. Savourey, J. C. Berthet, E. Nicolas, T. Cantat, *Angew. Chemie - Int. Ed.* **2019**, *58*, 10884–10887.

Annex

In this section we include the links to a repository or a source where anyone can access the Cartesian coordinates of the optimized structures that belong to this thesis. The information is given by chapter.

Chapter 4: *"Mechanistic Aspects of the Aryl-Co(III) Masked-carbene Formation with Diazo Esters."*

For this chapter, the coordinates are contained in the **supporting information** (SI) of the two published papers corresponding to this work:

- "Carboxylate-Assisted Formation of Aryl-Co(III) Masked-Carbenes in Cobalt-Catalyzed C–H Functionalization with Diazo Esters" DOI:10.1039/c8sc00851e.
- "Mechanistic insights into the S_N2-type reactivity of aryl-Co(III) masked-carbenes for C–C bond forming transformations" DOI: 10.1021/jacs.7b07880.

Chapter 5: *"Insight into the Trifluoromethylation Mechanism of a Well-Defined Aryl-Ni(II) Species via Putative Ni(IV) or Ni(II) Intermediates."*

In this case, most of the structures that correspond to this chapter are contained in the **supporting information** of the following paper:

- "Trifluoromethylation of a Well-Defined Square-Planar Aryl-Ni^{II} Complex involving $Ni^{III}/CF_3\cdot$ and $Ni^{IV}-CF_3$ Intermediate Species DOI:10.1002/chem.201702168.

except for the structures that correspond to the sections **5.3.4** and **5.3.5**, in which case we uploaded the structures into a "cloud service":

- https://tinyurl.com/y6zvbn48 (sections **5.3.4**)
- https://tinyurl.com/y33quw9u (sections **5.3.5**)

Chapter 6: *"Nickel-Catalyzed Aromatic Homologation by Alkyne Insertion versus Alkyne Mono-annulation by Reductive Elimination."*

For this chapter, the coordinates are contained in the **supporting information** (SI) of the recently published paper (manuscript accepted):

- "Chemo-Divergent Nickel(0)-Catalyzed Arene C–F Activation with Alkynes: Unprecedented C-F/C-H Double-Insertion" DOI:10.1021/acscatal.9b03620.

Chapter 7: *"On-ligand Amine-to-Amide Formation by CO Insertion on a Well-defined Iron(II) Complex."*

In this case, the coordinates of the optimized structures are stored in a cloud service, which can be accessed with the following link:

- https://tinyurl.com/yyszj66n